

Very high redshift quasars and the rapid emergence of super-massive black holes

Pavel Kroupa^{1,2,3*}, Ladislav Subr^{2†}, Tereza Jerabkova^{1,2,3,4,5,6‡}§, Long Wang^{7¶}¶

¹Helmholtz-Institut für Strahlen- und Kernphysik, University of Bonn, Nussallee 14-16, D-53115 Bonn, Germany

²Charles University in Prague, Faculty of Mathematics and Physics, Astronomical Institute, V Holešovičkách 2, CZ-180 00 Praha 8, Czech Republic

³Astronomical Institute, Czech Academy of Sciences, Fričova 298, 25165, Ondřejov, Czech Republic

⁴Instituto de Astrofísica de Canarias, E-38205 La Laguna, Tenerife, Spain

⁵GRANTECAN, Cuesta de San Jose s/n, 38712 Brena Baja, La Palma, Spain

⁶European Space Research and Technology Centre (ESA ESTEC), Keplerlaan 1, 2201 AZ Noordwijk, Netherlands

⁷Department of Astronomy, School of Science, The University of Tokyo 7-3-1 Hongo, Bunkyo-ku, Tokyo 113-0033, JAPAN

18 September 2020

ABSTRACT

The observation of quasars at very high redshift such as Pōniuā’ena is a challenge for models of super-massive black hole (SMBH) formation. This work presents a study of SMBH formation via known physical processes in star-burst clusters formed at the onset of the formation of their hosting galaxy. While at the early stages hyper-massive star-burst clusters reach the luminosities of quasars, once their massive stars die, the ensuing gas accretion from the still forming host galaxy compresses its stellar black hole (BH) component to a compact state overcoming heating from the BH–BH binaries such that the cluster collapses, forming a massive SMBH-seed within about a hundred Myr. Within this scenario the SMBH–spheroid correlation emerges near-to-exactly. The highest-redshift quasars may thus be hyper-massive star-burst clusters or young ultra-compact dwarf galaxies (UCDs), being the precursors of the SMBHs that form therein within about 200 Myr of the first stars. For spheroid masses $\lesssim 10^{9.6} M_{\odot}$ a SMBH cannot form and instead only the accumulated nuclear cluster remains. The number evolution of the quasar phases with redshift is calculated and the possible problem of missing quasars at very high redshift is raised. SMBH-bearing UCDs and the formation of spheroids are discussed critically in view of the high redshift observations. A possible tension is found between the high star-formation rates (SFRs) implied by downsizing and the observed SFRs, which may be alleviated within the IGIMF theory and if the downsizing times are somewhat longer.

Key words: star clusters: general, galaxies: star formation, galaxies: nuclei, galaxies: formation, quasars: general, cosmology: miscellaneous

1 INTRODUCTION

The existence of super massive black holes (SMBHs, masses $M_{\text{SMBH}} \gtrsim 10^6 M_{\odot}$) at the centers of galaxies has been surmised since a long time (Salpeter 1964; Wolfe & Burbidge 1970; Lynden-Bell & Rees 1971) and appears now well secured through the observation of the orbit of the S2 star near the centre of the Milky Way with the GRAVITY instrument (Gravity Collaboration et al. 2018), astrometric

measurements of the motion of Sgr A* (Reid & Brunthaler 2020) and the observation of the shadow of the SMBH in M87 with the Event Horizon Telescope (Event Horizon Telescope Collaboration et al. 2019). The observed rapid appearance of SMBHs in the early Universe, their correlation with their host galaxy properties and the presence of recently discovered SMBHs in ultra-compact dwarf galaxies (UCDs) remain, however, unexplained (Ferrarese & Merritt 2002; Kormendy & Ho 2013; Seth et al. 2014; Heckman & Best 2014; Janz et al. 2015; Di Matteo et al. 2017; Mezcua 2017; Bañados et al. 2018; Ahn et al. 2017, 2018; Afanasiev et al. 2018), with UCDs with mass $< 10^7 M_{\odot}$ apparently not hosting SMBHs (Voggel et al. 2018). SMBHs with masses $M_{\text{SMBH}} \approx 10^{10} M_{\odot}$ have been argued to exist a few hun-

* pkroupa@uni-bonn.de; pavel.kroupa@mff.cuni.cz

† subr@sirrah.troja.mff.cuni.cz

‡ tereza.jerabkova@esa.int

§ ESA Fellow

¶ long.wang@astron.s.u-tokyo.ac.jp

dred Myr after the Big Bang (Bañados et al. 2016; Di Matteo et al. 2017; Bañados et al. 2018; Mezcuca 2017). This poses a challenge for theories of the formation of SMBHs because they are observed at high redshift to be accreting at (Willott et al. 2010; Bañados et al. 2018) or below (Mazuchelli et al. 2017; Kim et al. 2018) the Eddington limit (Eq. 45 in Sec. 8.1). Assuming super-Eddington accretion with only 10 per cent of the infalling matter being radiated away ($\epsilon_r = 0.1$ in Eq. 45 in Sec. 8.1), a stellar-mass black hole (BH) seed, $M_{\text{seed}} = 10 M_{\odot}$, would still need to continuously accrete for $t_{\text{accr}} \approx 1 \text{ Gyr}$ to reach $10^{10} M_{\odot}$. This poses a problem if the hosting spheroid galaxy¹ forms on a much shorter downsizing time-scale (Eq. 1 below) after which gas infall shuts off. Quasars have life-times of about 10–100 Myr (Martini & Weinberg 2001; Yu & Tremaine 2002) and the first stars would have formed after 200 Myr after the Big Bang due to the time required for metal-free gas to cool (Yoshida et al. 2004). Indeed, a star-forming, about $10^9 M_{\odot}$ galaxy has been discovered at a redshift $z = 9.1$ which is about 250 Myr after the birth of the Universe (Hashimoto et al. 2018). These authors find the bulk of its formation to have occurred at $z \approx 15$, with a suppression of its star-formation rate SFR² and a rejuvenated gas inflow leading to the detected star formation at $z \approx 9.1$. It remains a challenge to understand the observed rapid appearance of the SMBH–host galaxy correlations in view of the theoretically predicted hierarchical formation of galaxies in standard cosmology (e.g. Kotilainen et al. 2009; Portinari et al. 2012; Latif & Ferrara 2016), noting that the SMBH–host galaxy correlation extends from elliptical galaxies to the bulge component of disk galaxies (Sanghvi et al. 2014). In the recent review of high redshift ($z \gtrsim 5$) quasars and their host galaxies, Trakhtenbrot (2020) writes that the multi-wavelength data show these SMBHs to be consistent with Eddington-limited, radiatively efficient accretion which had to proceed near-to continuously since very early epochs. Trakhtenbrot (2020) also writes that ALMA observations of the host’s inter-stellar medium uncover gas-rich, well developed galaxies, with SFRs that may exceed $\approx 1000 M_{\odot}/\text{yr}$.

Possible theoretical explanations (see Latif & Ferrara 2016 for a review) for much larger M_{seed} or more rapid mass growth are primordial black holes (Carr & Hawking 1974; Deng & Vilenkin 2017), hyper-Eddington or supra-exponential accretion (Alexander & Natarajan 2014; Begelman & Volonteri 2017), the very massive first metal-free population III stars leaving massive BH seeds or runaway stellar mergers in massive star clusters which would have had very large masses leaving direct-collapse SMBH seeds (Portegies Zwart & McMillan 2002; Rasio et al. 2004; Portegies Zwart et al. 2004; Goswami et al. 2012; Mapelli 2016). These suggestions rely on the uncertain stellar evolution of hyper-massive stars (see e.g. Díaz et al. 2019 for a discussion of the physical barriers concerning direct cloud collapse to form SMBH-seeds, Alister Seguel et al. 2019 for a discussion

of mass loss during mergers of population III stars, Woods et al. 2020 for an exploration of the theoretical limiting one-dimensional evolution of zero-metallicity, non-rotating stars). Also studied is the possible direct collapse of the first baryonic structures (Latif & Schleicher 2015; Mayer & Bonoli 2019; Ardaneh et al. 2018; Latif et al. 2019), which rely on early structure formation in standard dark matter models (see Haemmerlé et al. 2020 for a review).

With this contribution an explanation for the rapid emergence of SMBHs of all masses is sought which may operate by itself or in conjunction with the above suggestions, but does not need to invoke additional non-standard physics. Growing a black hole by accretion of gas is inefficient because a significant fraction of the rest-mass energy of the infalling matter is radiated as photons and ejected via jets. The key idea followed here is based on the high efficiency of mass-growth of black holes when they merge. According to the LIGO/VIRGO observations of gravitational wave signals from merging binary black holes, the merged black hole mass is only less than 5 per cent lighter than the sum of the pre-merger black holes (Abbott et al. 2016, 2019). A rapidly functioning physical mechanism ensuring the merger of many black holes may thus be a necessary key ingredient for understanding the observed rapid appearance of SMBHs in the Universe within a conservative framework.

To this end, we consider here the stellar population formed from extremely low metallicity gas in the first highest-density peaks of star formation, relying on previously independently obtained knowledge on the properties of such a population. The evolution is formulated of the stellar black hole (BH) sub-cluster with initial mass $M_{\text{BH},0}$ which is left after the massive stars have evolved. The cluster most likely forms mass-segregated (e.g. Pavlík et al. 2019) and if not it will dynamically mass-segregate to a half mass radius which depends on the mass-fraction of BHs (Breen & Heggie 2013a). Giersz et al. (2015) show that such a cluster can form an intermediate mass black hole (IMBH, mass $10^3 \lesssim M_{\text{IMBH}}/M_{\odot} < 10^6$) through runaway merging of its BHs, but the time-scale for this, being of the order of 10–15 median two-body relaxation times, t_{rlx} , is too long ($> \text{few Gyr}$) to account for the rapid ($\lesssim 300 \text{ Myr}$) appearance of SMBHs after the birth of the Universe. For the BH sub-cluster to form a SMBH-seed mass comprising a significant fraction of $M_{\text{BH},0}$, it needs to reach a velocity dispersion of about 1 per cent of the speed of light (Lee 1993, 1995; Kupa et al. 2006), because then the energy dissipation through the radiation of gravitational waves due to BH–BH encounters makes the relativistic collapse inevitable on the core-collapse time-scale of the BH sub-cluster, being as above $10 < t_{\text{collapse}}/t_{\text{rlx}} < 15$. This relativistic state can only be reached if the BH sub-cluster has a half-mass radius less than 0.02 pc (for $M_{\text{BH},0} = 10^6 M_{\odot}$). In this case t_{collapse} is of the order of a Myr (assuming the BHs have masses $m_{\text{BH}} = 50 M_{\odot}$). The problem is that BH-binaries which form in the core of the BH sub-cluster heat it, leading to long-term balanced evolution of the cluster (Breen & Heggie 2013b) such that such small radii cannot be reached. But if gas from the assembling spheroid accretes onto the central BH sub-cluster it may squeeze it into the relativistic state. This idea is placed into the context of the formation of spheroids and their stellar population. An essential part of the here presented theory is to calculate the radius shrinkage of the

¹ Many disk galaxies have central old spheroidal (classical) bulges which have largely indistinguishable properties from those of elliptical galaxies (Gadotti & Kauffmann 2009) and we refer to elliptical galaxies and classical bulges as spheroids or spheroid galaxies.

² SFR is the acronym for “star-formation rate”, while *SFR* is the corresponding physical quantity.

BH sub-cluster within the massive star-burst cluster, which, according to the IGIMF theory (Sec. 3.3), is expected to have formed during the formation of a spheroid.

The observed correlations between the galaxy-wide SFR and the population of forming star clusters and the stellar initial mass function (IMF, the number of stars per mass interval) are discussed in Sec. 2 and in Sec. 3, respectively. Following Jerabkova et al. (2018) we distinguish between the composite or galaxy-wide IMF, gwIMF, and the IMF which constitutes the population of stars formed in one embedded star cluster, see also Kroupa et al. (2013); Hopkins (2018). These set the stage for the calculation of the formation of the SMBH (Sec. 4, Sec. 5). The resulting galaxy–SMBH-mass correlation and the expected number of quasars at high redshift are addressed, respectively, in Sec. 6 and 7. The latter section includes a discussion of the newly discovered Pōniūā’ena. Sec. 8 deals with caveats and compares the model with observations of star-forming objects at high redshift. Sec. 9 contains the conclusions.

2 THE GALAXY–STAR-CLUSTER CORRELATION

The correlation between galaxy mass and its star-cluster population is discussed in this section, before continuing with a discussion of the initial stellar population in massive star-burst clusters in Sec. 3. In the following we first discuss the downsizing problem (Sec. 2.1), then populating a forming spheroid with star clusters (Sec. 2.2).

2.1 The formation time scale for spheroids

Observations of the chemical abundances suggest that the most massive spheroids, which typically harbour the most-massive SMBHs (Ferrarese & Merritt 2002), may have formed very early and on a time scale, $\Delta\tau$, of less than a Gyr. This downsizing result was deduced originally by Matteucci (1994); Thomas et al. (1999, 2005); Recchi et al. (2009); Yan et al. (2019b); Salvador-Rusiñol et al. (2020) through the following general argument: Core-collapse supernovae (e.g. SN type II) enrich the inter-stellar medium (ISM) with α elements and iron, Fe, while the type Ia supernovae contribute most of the Fe. Stars formed from the ISM which was being enriched by SN II will thus have similar $[\alpha/\text{Fe}]$ abundance ratios. When SN Ia begin to explode with a delay after the SN II cease the $[\alpha/\text{Fe}]$ abundance ratio of the ISM begins to decrease. The observed super-solar $[\alpha/\text{Fe}]$ abundance of the stellar population in spheroids requires $\Delta\tau$ to be shorter than the time needed for SN Ia to contribute significant Fe to the gas from which the population formed (for a discussion on the uncertainty of the delay-time distribution see Yan et al. 2020). By implication, the so-constrained $\Delta\tau$ leads to a high average SFR ($= M_{\text{igal}}/\Delta\tau$) and Matteucci (1994) additionally finds the gwIMF to need to be top-heavy in order to explain the high observed (near-to solar or super-solar) metallicity, Z , of the massive spheroids.

From fig. 18 in Recchi et al. (2009) the downsizing relation follows (see also Fig. 9 below),

$$\Delta\tau/\text{Gyr} = 8.16 e^{(-0.556 \log_{10}(M_{\text{igal}}/M_{\odot}) + 3.401)} + 0.027, \quad (1)$$

where $10^6 \lesssim M_{\text{igal}}/M_{\odot} \lesssim 10^{12}$ is the initial stellar mass of the

galaxy (“initial” referring in this context to the total stellar mass assembled without stellar-evolutionary mass loss, but compare with Fig. 10 below). For example, a giant spheroid with an initial stellar mass $M_{\text{igal}} = 10^{12} M_{\odot}$ would have formed over a time-scale of $\Delta\tau = 0.34$ Gyr implying a star-formation rate $SFR = 2941 M_{\odot}/\text{yr}$ (the formation of spheroids and these model vs observed SFRs are discussed in more detail in Sec. 8.2). Such SFRs are indeed observed at high redshift ($z > 4$: Glazebrook et al. 2017; Pavesi et al. 2018; Miller et al. 2018; Fan et al. 2019; Nguyen et al. 2020). The REQUIEM Survey I finds high redshift ($z \approx 6$) quasars to be surrounded by massive circum-galactic media on scales of dozens of kpc typical of massive galaxies (Farina et al. 2019), suggesting a significant cool gas component to exist from which the spheroid hosting the quasar accretes. Stellar-population synthesis of spheroids confirms the downsizing relation but suggests a systematically longer $\Delta\tau$ by a factor of about two (McDermid et al. 2015, see also de La Rosa et al. 2011).

The implied short formation times thus suggest a monolithic formation of spheroids: Following Comerón et al. (2016), monolithic formation or collapse of a stellar system is understood to be its rapid formation where several generations of stars form in rapid succession, essentially on a free-fall time-scale. Assume a spherical post-Big-Bang gas cloud of mass M_{cloud} in units of M_{\odot} with initial radius R_{cloud} in units of pc collapses on a free-fall time scale and forms a spheroid. Thus, if the formation time $\Delta\tau_{\text{Myr}}$ in units of Myr is assumed to be the free-fall time (Eq. 10) it follows that $R_{\text{cloud}} \approx (\Delta\tau_{\text{Myr}}/16.6)^{2/3} M_{\text{cloud}}^{1/3}$. This means that for a spheroid which forms $10^{12} M_{\odot}$ in stars in $\Delta\tau = 0.34$ Gyr (Eq. 1), $R_{\text{cloud}} \approx 100$ kpc assuming a star-formation efficiency of 1/3. This rough estimate is smaller in reality due to cosmic expansion (needing a higher density and thus smaller radius for gravitational decoupling from the initial Hubble flow), but suggests (in this model) that the gas which forms the bulk of the final spheroid accretes from a region with a radius of $\lesssim 100$ kpc. Since no fully-fledged independent galaxy would have been able to develop within the flow within 0.34 Gyr, the so-formed spheroid can be referred to as having formed monolithically, i.e., in one collapse. However, it is likely that the in-falling gas would not be homogeneous such that sub-regions collapse faster forming stars in sub-galactic objects such that the “monolithic” formation may well be associated with the rapid merging of developing sub-galactic building blocks. This monolithic formation model would be replaced by a merging model if $\Delta\tau$ would be longer, but the essence of the model is the natural physical correlation between the central gas density, where the most massive (and first) star cluster forms, and the overall proto-spheroid gas mass which ultimately leads to the observed SMBH-mass–spheroid-mass correlation. This natural physical correlation is at the heart of the IGIMF theory discussed next.

2.2 The most massive embedded cluster in the forming spheroid

Extragalactic observations (Larsen & Richtler 2000; Larsen 2002b,a; Randriamanakoto et al. 2013; Whitmore et al. 2014) have shown that the stellar mass, $M_{\text{ecl,max}}$, of the most-

massive star cluster forming in a galaxy follows the empirical WKL correlation with the galaxy-wide SFR (Weidner et al. 2004),

$$M_{\text{ecl,max}}/M_{\odot} = 8.24 \times 10^4 \times (SFR/(M_{\odot}/\text{yr}))^{0.75}. \quad (2)$$

Randriamanakoto et al. (2013) find the dispersion of the masses of the most-massive clusters at a given SFR to be smaller than expected from random sampling, and Larsen (2002b) emphasises that the mass of the most massive young cluster depends on the SFR of the galaxy, and thus the pressure (Elmegreen & Efremov 1997), such that globular (GC) and open star clusters are part of the same family, rather than requiring distinct formation conditions. In the example above ($SFR = 2491 M_{\odot}/\text{yr}$), $M_{\text{ecl,max}} \approx 2.9 \times 10^7 M_{\odot}$.

The gaseous inter-stellar medium transforms to a new population of stars on a time-scale of about $\delta t' = 10 \text{ Myr}$. This time scale is observed to be the life-time of molecular clouds (Fukui et al. 1999; Yamaguchi et al. 2001; Tamburro et al. 2008; Fukui & Kawamura 2010; Meidt et al. 2015) and is also deduced from the offset of dusty spiral patterns from the freshly hatched stellar population in spiral galaxies (Egusa et al. 2004, 2009). The mass of the stars formed in the galaxy over the time interval δt is

$$M_{\delta t}(t) = SFR(t) \times \delta t. \quad (3)$$

According to observations, most stars form clustered in the density peaks in molecular clouds (Lada & Lada 2003; Lada 2010; Megeath et al. 2016; Joncour et al. 2018), a conclusion also reached from binary-star dynamical population synthesis (Kroupa 1995; Marks & Kroupa 2011). The distribution function of stellar masses, M_{ecl} , of these embedded clusters has been observed to be a power-law (Zhang & Fall 1999; Larsen 2002a; Lada & Lada 2003; Hunter et al. 2003; Weidner et al. 2004; McCrady & Graham 2007),

$$\xi_{\text{ecl}}(M_{\text{ecl}}) = k_{\text{ecl}} M_{\text{ecl}}^{-\beta}, \quad M_{\text{ecl}} \geq M_{\text{ecl,min}}, \quad (4)$$

where $M_{\text{ecl,min}} \approx 5 M_{\odot}$ is the minimum embedded stellar group or cluster mass (as observed in e.g. the Taurus-Auriga star-forming region, Joncour et al. 2018), $dN_{\text{ecl}} = \xi_{\text{ecl}} dM_{\text{ecl}}$ being the number of embedded clusters with birth masses (in stars) in the mass range M_{ecl} to $M_{\text{ecl}} + dM_{\text{ecl}}$.

The power-law index of the embedded cluster mass function is suggested by Weidner et al. (2004) to be $\beta = 2.4$ based on $M_{\text{ecl,max}} - SFR$ data for late-type galaxies. Murray (2009) summarises that $1.5 < \beta < 2$. According to Weidner et al. (2013b) $\beta \leq 2.0$ is possible with $\xi_{\text{ecl}}(M_{\text{ecl}})$ becoming more top-heavy with increasing galaxy-wide SFR and decreasing metallicity. We will discuss both possibilities ($\beta = 2$ and 2.4 , for a discussion and references see Schulz et al. 2015) in Sec. 6 but take $\beta = 2$ as the default canonical value.

Solving for $M_{\text{ecl,max}}$ the following two equations,

$$M_{\delta t}(t) = \int_{M_{\text{ecl,min}}}^{M_{\text{ecl,max}}(SFR)} M_{\text{ecl}} \xi_{\text{ecl}}(M_{\text{ecl}}) dM_{\text{ecl}}, \quad (5)$$

$$1 = \int_{M_{\text{ecl,max}}(SFR)}^{M_{\text{ecl,max}*}} \xi_{\text{ecl}}(M_{\text{ecl}}) dM_{\text{ecl}},$$

where $M_{\text{ecl,max}*}$ is the physical allowed maximum cluster mass (we adopt $M_{\text{ecl,max}*} = 10^{9.7} M_{\odot}$, but the results are not sensitive to this value as long as $M_{\text{ecl,max}*} \geq 10^9 M_{\odot}$, see Weidner et al. 2004) the calculated $M_{\text{ecl,max}}(SFR)$ re-

lation follows the above WKL correlation (Eq. 2) very closely if $\delta t \approx 10 \text{ Myr}$ in general, and with $\beta = 2.4$. The values of $M_{\text{ecl,max}}$ are significantly larger for $\beta = 2$ than for $\beta = 2.4$. For example, if $SFR = 3 \times 10^3 M_{\odot}/\text{yr}$ then $M_{\text{ecl,max}} \approx 3.3 \times 10^7 M_{\odot} (\beta = 2.4)$ and $M_{\text{ecl,max}} \approx 3 \times 10^9 M_{\odot} (\beta = 2.0)$; see fig.2 in Yan et al. (2017). This has an important bearing on the mass of the SMBH-seed which can form in the central most-massive star-burst cluster within a few hundred Myr as discussed in Sec. 6 below). Note the consistency of this model with the data, because $\delta t \approx \delta t'$.

Assuming $SFR \approx M_{\text{igal}}/\Delta\tau$ remains about constant over the time of formation of the galaxy (i.e. we assume a box-shaped star-formation history, SFH),

$$N_{\text{gen}} = \Delta\tau/\delta t \quad (6)$$

generations of embedded cluster populations form, each following the above relations. This is supported by observational evidence in that subsequently-populated $\xi_{\text{ecl}}(M_{\text{ecl}})$ can be extracted from observed luminosity functions of GCs and UCDs in galaxy clusters (Schulz et al. 2016). Therefore, a $M_{\text{igal}} = 10^{12} M_{\odot}$ elliptical galaxy will have formed $N_{\text{gen}} \approx 34$ most-massive clusters of mass $M_{\text{ecl,max}} \approx 3.3 \times 10^7 M_{\odot}$ (if $\beta = 2.4$) up to $M_{\text{ecl,max}} \approx 3 \times 10^9 M_{\odot}$ (for $\beta = 2.0$) during its assembly. Only the first-formed clusters will be extremely metal poor though (Yan et al. 2019b), this being important for the shape of the IMF and thus the content of BHs (Jerabkova et al. 2017). The true star-formation history is likely to have been more complex with peak star formation rates that may surpass the average SFR .

Spheroids would thus have formed many massive star-burst clusters in the densest gas clouds usually observationally (Joseph & Wright 1985; Wright et al. 1988; McCrady & Graham 2007; Stolte et al. 2014; Ando et al. 2017; Leroy et al. 2018; Randriamanakoto et al. 2019) and theoretically (Norman 1987; Li et al. 2017) found near their centres where the highest gas pressures reign (Elmegreen & Efremov 1997). Cases in point for the ongoing formation of the most-massive clusters in the central region are the galaxies Arp 220 (Lonsdale et al. 2006), M33 (Pflamm-Altenburg et al. 2013) and Henize 2-10 (Nguyen et al. 2014). Evidence for higher and earlier past innermost star-forming intensities find support from metallicity and age tracers (Martín-Navarro et al. 2018; Martín-Navarro et al. 2019) and morphological studies at high redshift (Pavesi et al. 2018) as well as measured radial metallicity and age gradients in spheroids (Zibetti et al. 2019). The observed compactness ($\approx 40 \text{ pc}$) of $6 \lesssim z \lesssim 8$ galaxies with stellar masses $10^6 - 10^7 M_{\odot}$ may thus be naturally explained in this way (Ploeckinger et al. 2019).

2.3 Summary

The masses of the most-massive young clusters in star-forming galaxies correlate positively with the SFR and with decreasing galactocentric distance.

3 THE STELLAR POPULATION IN MASSIVE STAR-BURST CLUSTERS AND IN ULTRA COMPACT DWARF GALAXIES

In this section the initial stellar population in massive star-burst clusters is discussed. First (Sec. 3.1) the canonical stel-

lar IMF is introduced. In Sec. 3.2 the observational evidence on the molecular cloud-core scale for a systematically varying IMF is elucidated. Consistency with the galaxy-wide initial stellar populations is tested for thereafter (Sec. 3.3). The content of stellar black holes (BHs) in individual clusters is then formulated (Sec. 3.4), in preparation for Sec. 4.

3.1 The canonical stellar IMF

One conservative assumption is the stellar population to be always described by an invariant IMF. Thus, for the invariant canonical IMF (Kroupa 2001, 2002; Chabrier 2003; Bastian et al. 2010; Kroupa et al. 2013; Offner et al. 2014), the number of freshly formed stars with masses in the range m to $m + dm$ in an embedded cluster is $dN = \xi(m) dm$, where the IMF, $\xi(m) = k m^{-\alpha_i}$, with $\alpha_1 = 1.3$ for $0.08 < m/M_\odot \leq 0.5$ and $\alpha_2 = 2.3$ for $0.5 < m/M_\odot < 1$. The canonical IMF, which is typical for star formation in the present-day Galaxy, has the Salpeter-Massey index $\alpha_3 = \alpha_2 = 2.3$ (Salpeter 1955; Massey et al. 1995; Massey 2003) for $1 M_\odot \leq m \leq m_{\max}(M_{\text{ecl}}) \leq m_{\max*}$, with $m_{\max*} \approx 150 M_\odot$ being the empirically found maximum stellar mass (Weidner & Kroupa 2004; Figer 2005; Oey & Clarke 2005; Koen 2006; Maíz Apellániz 2008; Banerjee et al. 2012), and $m_{\max}(M_{\text{ecl}})$ being the most-massive-star- M_{ecl} relation (Oh & Kroupa 2018).

3.2 The variable stellar IMF in dependence of the physical environment

Observation and stellar-dynamical analysis has suggested that low-metallicity star-burst clusters with $M_{\text{ecl}} \approx 10^4 - 10^5 M_\odot$, ages ≤ 10 Myr, which can be resolved into individual stars, have an over-surplus of massive stars relative to their low-mass star content when compared to the canonical IMF (Banerjee & Kroupa 2012; Schneider et al. 2018; Kalari et al. 2018). That is, the IMF appears to be top-heavy in massive and/or low-metallicity star-burst clusters compared to the canonical IMF. Evidence for an IMF which becomes increasingly top-heavy with decreasing metallicity and increasing star-formation rate per volume on a pc-scale consistent with these results has emerged from an analysis of the present-day properties of very old Milky Way GCs, which had birth masses $\approx 10^5 - 10^7 M_\odot$ and that have different but low metal abundances (Marks et al. 2012). The star clusters in the Andromeda galaxy likewise suggest a similar metallicity dependence of their IMFs (Hasani Zonoozi et al. 2016; Haghi et al. 2017). Present-day ultra compact dwarf galaxies (UCDs) have properties which resemble ultra-massive GCs with masses in the range $10^6 - 10^9 M_\odot$ (Hilker et al. 2007; Mieske et al. 2008; Brodie et al. 2011) and many have been shown to comply to this dependency of the IMF (Dabringhausen et al. 2009; Murray 2009; Dabringhausen et al. 2012; Marks et al. 2012). The high rate of core-collapse supernovae per year observed in the central region of the star-bursting galaxy Arp 220 suggests the stars to be forming with a top-heavy IMF. These observed massive central star-bursts appear to occur in individual UCD-type objects (Lonsdale et al. 2006; Dabringhausen et al. 2012). The extreme star-formation conditions within 0.04 to 0.4 pc of the Galactic centre lead, apparently, to a very top-heavy ($\alpha_3 \approx 0.45$, see Eq. 7) IMF significantly depleted in low mass stars (Bartko

et al. 2010, see also discussion in Kroupa et al. 2013), despite the high metallicity.

Theoretical work on star formation has also been suggesting that a top-heavy IMF ought to emerge in low metallicity and high density gas peaks in gas clouds. A shift to higher average stellar masses is needed for gravitational instability due to the lower efficiency of cooling in low-metallicity environments and environments with higher gas temperatures (Larson 1998; Murray 2009), as induced for example from cosmic ray heating produced by supernovae (Papadopoulos 2010), due to the increased rate of accretion resulting from a lower photon pressure in low-metallicity regions (Adams & Fatuzzo 1996; Adams & Laughlin 1996), higher ambient temperature (Riaz et al. 2020) and due to the coagulation in very dense proto-clusters of cloud cores to more massive ones before their individual collapse to proto stars can occur (Dib et al. 2007).

Given the above empirical evidence and the need for compliance with the on-going star-forming activity in the MW, the variation of the IMF with metallicity and density of the star-forming gas on the scale of an embedded cluster (≈ 1 pc) has been formulated as a dependency of the power-law indices describing the distribution of stellar masses (Dabringhausen et al. 2009, 2012; Marks et al. 2012; Recchi & Kroupa 2015; Yan et al. 2017; Jerabkova et al. 2018). Thus,

$$\alpha_3 = -0.41 x + 1.94; x \geq -0.87, \quad (7)$$

and $\alpha_3 = 2.3; x < -0.87$, where

$$x = -0.14 [\text{M}/\text{H}] + 0.99 \log_{10} \left(\rho_{\text{cl}} / (10^6 M_\odot \text{pc}^{-3}) \right), \quad (8)$$

with $[\text{M}/\text{H}]$ being the metal (all nuclei heavier than He providing cooling through electronic transitions) abundance and ρ_{cl} the density of the cluster-forming gas cloud core (Marks et al. 2012, as obtained from the embedded-cluster radius- M_{ecl} relation of Marks & Kroupa 2012; see also Recchi & Kroupa 2015; Jerabkova et al. 2018). Since the star-formation history building up an individual embedded cluster from the monolithic collapse of a molecular cloud core takes about 1 Myr (e.g. Beccari et al. 2017; Kroupa et al. 2018), the star-formation rate density during the formation of an embedded cluster is $\approx \epsilon \rho_{\text{cl}} / 1$ Myr, where ϵ is the star-formation efficiency (stellar mass formed per total initial mass). Caveats concerning the variation of the IMF as defined by Eq. 7 are discussed in Sec. 8.3.

3.3 Consistency Check: the galaxy-wide IMF

A consistency check as to whether the variation of the IMF on the scales of star-forming events detailed in Sec. 3.2 captures the broadly correct physical behaviour is provided by comparing with the galaxy-wide IMF (gwIMF) calculated by summing all star-formation events in a galaxy as detailed via the IGIMF theory (Kroupa & Weidner 2003; Pflamm-Altenburg et al. 2011; Kroupa et al. 2013; Recchi & Kroupa 2015; Yan et al. 2017; Jerabkova et al. 2018; Dabringhausen 2019). Calculating the gwIMF by summing all IMFs in the newly formed embedded clusters to obtain the composite or integrated IMF (i.e. the IGIMF) leads to galaxies with low/high SFRs having a top-light/top-heavy gwIMF, respectively.

This has indeed been found to be the case observationally (Lonsdale et al. 2006; Hoversten & Glazebrook 2008; Lee et al. 2009; Meurer et al. 2009; Gunawardhana et al. 2011; Rowlands et al. 2014; Romano et al. 2017; Zhang et al. 2018). Elliptical galaxies, having formed with $SFR > 10^3 M_\odot/\text{yr}$, have been found to have had early top-heavy gwIMFs in order to account for their high metallicity, despite their brief formation time-scales and a possibly bottom-heavy gwIMF during the final metal-rich formation phase (Matteucci 1994; Gibson & Matteucci 1997; Vazdekis et al. 1997; Weidner et al. 2013b,a; Martín-Navarro 2016; Fontanot et al. 2017; De Masi et al. 2018; Jerabkova et al. 2018). The top-heavy gwIMFs in galaxies which have or had high SFRs comes, within the model used here, from such galaxies forming very massive clusters (Sec. 2, Eq. 5), which have top-heavy IMFs. The observed dynamical mass-to-light ratios of early type galaxies are well consistent with the IGIMF being top-light at small galaxy masses ($\lesssim 10^9 M_\odot$) becoming increasingly top-heavy for massive spheroids leaving up to about half their present-day dynamical masses in the form of stellar remnants (Dabringhausen 2019). This observational and theoretical agreement of how the gwIMF changes with a changing SFR and metallicity is an important positive consistency-test for the IMF variation on the scale of individual star clusters (Sec. 3.2).

3.4 The BH content of high redshift star burst clusters, their appearance as quasars and later as UCDs

Assuming the canonical IMF above (Sec. 3.1), a few-Myr old massive star-burst cluster/UCD with mass M_{ecl} formed through a monolithic gas-cloud collapse contains

$$N_{\text{can}} = 6.3 \times 10^{-3} M_{\text{ecl}}/M_\odot \quad (9)$$

stars more massive than $20 M_\odot$ (see also Kroupa et al. 2013, their table 4-1, average stellar mass $\bar{m} = 0.55 M_\odot$). Thus, a $M_{\text{ecl}} = 10^7 M_\odot$ cluster would contain 1.8×10^7 stars and 6.3×10^4 stars more massive than $20 M_\odot$, each of these becoming, after about 50 Myr and ignoring stellar mergers and ejections, a BH.

According to the systematically varying IMF (Sec. 3.2), such a monolithically-formed cluster (MC) would, if formed with very low metallicity, be dominated in mass by massive stars and would have a bolometric luminosity of $L_{\text{bol}} \approx 4 \times 10^{10} L_{\text{bol}\odot}$ for dozens of Myr (Jerabkova et al. 2017). That is, such an object would appear quasar-like (see also an example below in this section) for a time comparable to quasar-life-times (Sec. 1). The above work shows the stellar populations would reach the luminosities of bright quasars and have comparable photometrical colors. The computed SEDs represent only stellar populations. In reality the massive star-burst clusters are complex systems of stars (and stellar BHs early on), gas and dust. In order to be able to compare detailed differences between the spectral properties of actual quasars (accreting SMBHs) and the hyper-massive clusters, detailed realistic hydro-dynamical simulations with radiative transfer in hot dense gas with dust would be necessary. While this certainly represents a fruitful pathway for future investigations, in this work "quasar-like" describes objects with photometric properties of a quasar in terms of brightness and color. The first such formed hyper-massive

cluster may inhibit the formation of further clusters due to its strong feedback (Ploeckinger et al. 2019). Once its massive stars have died, the supernovae, which lead to a variability of L_{bol} on a monthly time-scale by dozens of per cent, will have enriched the surrounding gas with metals such that obscuration by dust may be significant and the IMF in the cluster forming from the enriched gas may rapidly evolve to a more canonical form (Jerabkova et al. 2018). It is thus the first such massive cluster which may play a decisive role in the rapid emergence of SMBH-seeds.

On the other hand, some UCDs can form from the coagulation of massive star-cluster complexes (SCCs) (Kroupa 1998; Fellhauer & Kroupa 2002; Brüns et al. 2011) observed to have formed in strongly interacting star-bursting galaxies and also in the expelled gas-rich tidal arms (e.g. in the Tadpole galaxy, fig. 10 in Kroupa 2015). The composite IMF of such composite SCC UCDs is calculated assuming the UCD is made of a full ensemble of embedded clusters as above (Sec. 2). The composite IMF (cIMF) of a UCD is the sum over all its embedded clusters and their individual IMFs as given by the IGIMF theory (Sec. 3.3, see also Schulz et al. 2015), and is top-light relative to that of the MC UCD type, therewith containing a smaller number of remnants. Given that the assembly of spheroids will have involved mergers, it is likely that some of the very massive young clusters may be ejected from the inner regions or some may form in gas-rich tidal tails. Thus, at a given present-day UCD mass, a range of objects with different dynamical mass to light ratios is expected to exist in the vicinity of present-day spheroids in this theory.

A test of whether the model developed here is consistent with observational data on the pc-scale is provided by comparing the calculated photometric V-band mass-to-light (M/L_V) ratios with observational data of UCDs. The calculated values are dynamical M/L_V ratios because they include the mass from remnants and are thus directly comparable to the observed ratios, which are derived from the stellar velocity dispersions in the UCDs (see Dabringhausen et al. 2008 for an in-depth discussion of these issues). The comparison is done in Fig. 1 which demonstrates that the model well accounts for the data, given that most real UCDs are likely a mixture of the MC and SCC types (e.g., a certain fraction of the proto-UCD may form monolithically and may merge with many other massive clusters which formed in the same star cluster complex). Interesting is that the upper and lower boundaries of the models for plausible metallicities and ages encompass the observed data nearly completely. An invariant canonical IMF would lead to a horizontal line at a level depending on the age and metallicity. The brighter UCDs do not appear to be consistent with an invariant IMF (Dabringhausen et al. 2009, 2012).

The likely mass of all BHs (stemming from stars more massive than $20 M_\odot$) as a function of M_{ecl} and of the luminous mass for the typical UCD ages for the MC and SCC types is shown in Fig. 2. The luminous mass, M_{lum} , is approximated here to be the mass in all stars less massive than $1 M_\odot$. Fig. 3 depicts M_{lum} vs the initial or birth stellar mass of the MC and SCC types of UCDs.

Thus, according to the model developed here, a present-day UCD with a mass in shining stars of $M_{\text{lum}} \approx 10^8 M_\odot$ would have had the following properties:

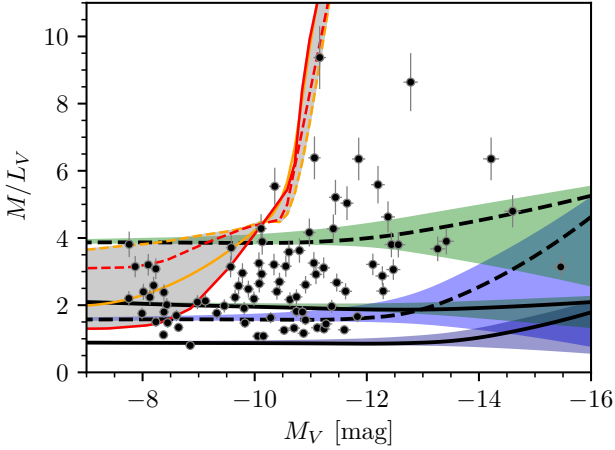


Figure 1. The dynamical mass to V-band light (M/L_V) ratio of the MC (red and orange) and SCC (green and blue) models for different metallicities. The MC models which assume the varying IMF (Eq. 7, Marks et al. 2012) are shown for an age of 10 Gyr. The dashed red line is for $[\text{Fe}/\text{H}] = -2$ assuming all BHs are retained. The dashed orange line is for $[\text{Fe}/\text{H}] = 0$ assuming all BHs are retained. The full red line is for $[\text{Fe}/\text{H}] = -2$ assuming the BHs are retained dynamically, i.e. in dependence of the distribution of kick velocities of neutron stars and BHs (assuming a kick velocity dispersion of 190 km/s) and the depth of the potential well (assuming the initial radius-mass relation of Marks & Kroupa 2012, see Jerabkova et al. 2017; Pavlík et al. 2018 for details). The full orange line is for $[\text{Fe}/\text{H}] = 0$ assuming the BHs are retained dynamically. The SCC models assume the composite IMF to be given by the sum of all varying IMFs (Eq. 7) in all star clusters which form the final UCD following the IGIMF theory (Sec. 3.3, see Jerabkova et al. 2018 for the details, the IGIMF3 formulation being applied here). The lower boundaries of the coloured regions show models which retain no BHs, while the upper boundaries assume all BHs are retained. The black lines show the results if BHs are retained dynamically. Note the down trend of the lower boundaries for the brighter (more massive) UCDs. It is due to removing BHs in increasingly top-heavy composite IMFs for which the BHs contribute an increasing fraction of the mass. The black line is dashed for an age of 13 Gyr and full for an age of 5 Gyr, both for $[\text{Fe}/\text{H}] = -2$. The upper blue region is for an age of 13 Gyr and the lower dark blue region assumes models at an age of 5 Gyr, both having $[\text{Fe}/\text{H}] = -2$. The upper green models assume an age of 13 Gyr, and the lower dark green models assume an age of 5 Gyr, both being for $[\text{Fe}/\text{H}] = 0$. The luminosities of the models are calculated with the second release of the spectral evolution code PEGASE2 (Fioc & Rocca-Volmerange 1997). The data points are observed UCDs with their uncertainties (Voggel et al. 2019, not their normalised data). The stellar-population and dynamical properties of UCDs in terms of their formation process is studied in much more detail by Mahani et al. (in prep.).

- If born monolithically (MC type), a total birth mass in stars comprising $M_{\text{ecl}} \gtrsim 10^{10} M_{\odot}$ and a mass in BHs of $M_{\text{BH},0} \gtrsim 10^9 M_{\odot}$. This type of object would have $L_{\text{bol}} \approx 10^{13} L_{\text{bol}\odot}$ which varies by 10 per cent on a monthly time-scale due to the large number of core-collapse supernovae. It would drive a metal-rich, massive-star- and supernova-driven outflow of $\approx 200 M_{\odot}/\text{yr}$ with an outflow speed of probably > 1000 km/s (outflow velocities ≈ 1000 km/s are computed for $10^5 < M_{\text{ecl}}/M_{\odot} \leq 10^6$ by Chevalier & Clegg 1985; Tenorio-Tagle et al. 2007, 2010; Silich et al. 2011). Trakht-

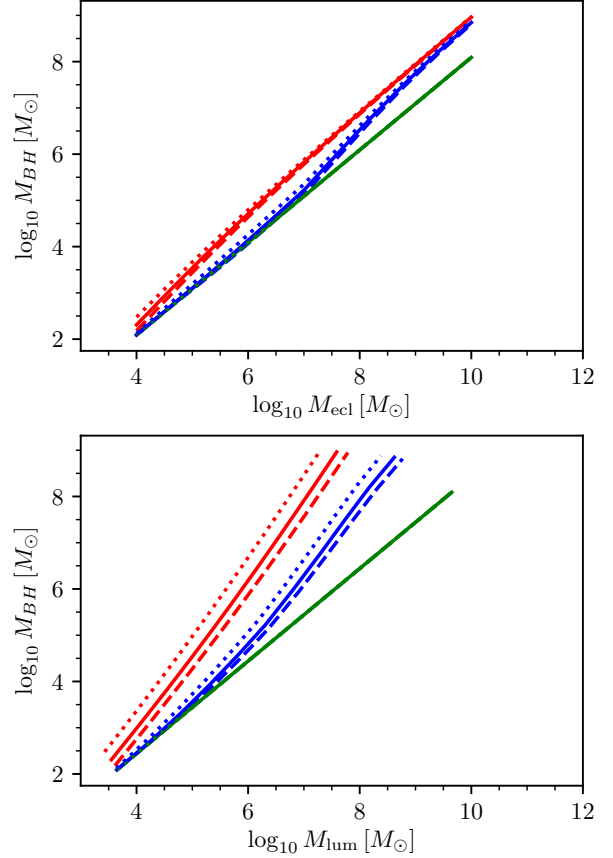


Figure 2. The model mass in BHs ($M_{\text{BH}} = M_{\text{BH},0}$) in UCDs in dependence of the (upper panel) UCD birth mass in stars, M_{ecl} , and of the (lower panel) UCD luminous mass (M_{lum} , defined as the mass in all stars less massive than $1 M_{\odot}$; see also Fig. 3). The models assume all BHs are retained and that a BH comprises 10 per cent of the birth mass of the star and that only stars more massive than $20 M_{\odot}$ leave BHs. The red lines are for MC models and assume the varying IMF (Eq. 7), while the blue lines are for SCC models and assume the UCDs are made from a fully sampled population of star clusters (following the IGIMF3 formulation in Jerabkova et al. 2017). The green line is for the invariant canonical IMF. The dotted lines are for $[\text{Fe}/\text{H}] = -5$, the full lines are for $[\text{Fe}/\text{H}] = -2$ and the dashed lines are for $[\text{Fe}/\text{H}] = 0$.

enbrot (2020) discusses similar observed outflows from high redshift quasar-hosting systems. An observer may interpret the luminosity to be the accretion luminosity onto a SMBH of Eddington mass $\approx 3 \times 10^7 M_{\odot}$ (Eq. 48). This similarity in spatially unresolved observational data between very young super-star-clusters and accreting SMBHs, which extends also to the spectral energy distribution, has been discussed in the past (Terlevich & Melnick 1985, for a historical review see Shields 1999). Such an MC type cluster may thus appear, to a certain degree, as a very high redshift quasar (see Jerabkova et al. 2017, who however only calculate the stellar SED of such objects). The masses of SMBHs at high redshift are estimated from the width of their spectral lines as well as their accretion luminosity, as successfully obtained for the first time for a $z = 5.9$ quasar by Eilers et al. (2018).

- If born from a full distribution of star clusters (SCC type), a total birth mass in stars comprising $M_{\text{ecl}} \approx 10^{9.5} M_{\odot}$ with $M_{\text{BH},0} \approx 10^{8.5} M_{\odot}$.

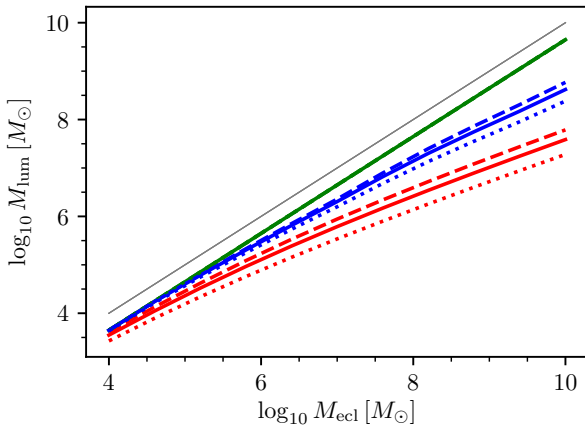


Figure 3. The luminous mass M_{lum} in dependence of the initial MC (red) and SCC (blue) stellar mass, M_{ecl} , of the UCD models as in Fig. 2. The thin gray line is the 1:1 relation.

- If born with a canonical IMF, a total birth mass in stars comprising $M_{\text{ecl}} \approx 10^{8.1} M_{\odot}$ with $M_{\text{BH},0} \approx 10^{6.5} M_{\odot}$.

Note that the apparent quasar-likeness extends also to this (canonical) and the previous SCC case, with the MC case being the most extreme in the present models (subject to the possibility that the IMF may have been even more top-heavy at very low metallicity). Whether such objects do in fact resemble the observed properties of high redshift quasars needs to be ascertained and tested by calculating the spectrum of the metal-rich > 1000 km/s fast outflow in combination with that of the stellar SED and dust self-obscurtion. Trakhtenbrot (2020) writes that the (rest-frame) UV spectra of the highest- and lower-redshift quasars are remarkably similar to each other (when matched in luminosity), referring in particular to the broad emission lines of $\text{C}_{\text{IV}}\lambda 1549$, $\text{C}_{\text{III}}\lambda 1909$, and $\text{Mg}_{\text{II}}\lambda 2798$, and that such comparisons need to account for the tendency of highly accreting quasars to show blue-shifted (UV) broad lines. It is beyond the scope of this work to perform the necessary radiation transfer calculations within the dynamical winds. The similarities and differences of these to the outflows powered by accreting SMBHs at low to moderate redshift (e.g. Arav et al. 2020) will need to be studied. This may thus be seen as an interesting topic for future research.

3.5 Summary

The top-heaviness of the IMF in star-burst clusters correlates positively with decreasing metallicity and increasing star-formation rate density and thus birth mass of the cluster. The observationally constrained galaxy-wide IMFs are consistent with this variation. The observed properties of present-day UCDs are also consistent with this variation. The massive star-burst clusters thus contain populations of stellar BHs that can be estimated using this variation of the IMF. The case can be raised that the first (very metal-poor) hyper-massive star-burst clusters which most likely formed at the centres of the spheroids resemble, for some dozens of Myr, quasars in terms of spatial compactness, luminosity and outflow speeds.

4 THE CLUSTER OF STELLAR MASS BLACK HOLES AND ITS COLLAPSE

In this section the theoretical framework is developed, and Sec. 5 presents the results of the calculations.

To introduce the model, assume for now that the central region of the collapsing gas cloud, which will become the spheroid with (for example) a peak global $SFR \gtrsim 3 \times 10^3 M_{\odot}/\text{yr}$, forms within about a Myr at least one massive ($M_{\text{ecl,max}} \gtrsim 3 \times 10^7 M_{\odot}$) star-burst cluster with a birth half-mass radius $r_{\text{h}} \approx 1$ pc (Marks & Kroupa 2012) and of very low metallicity ($[\text{M}/\text{H}] \approx -6$) and thus with a top-heavy IMF ($\alpha_3 \approx 1.05$, Eq. 7). Note that the *first* stars will be formed as a population at the centre of the forming spheroid before the spheroid exists and before it has self-enriched with metals. The IMF of this population of stars in this first hyper-massive cluster will be very top-heavy, assuming Marks et al. (2012) holds. After this population has formed its massive stars will begin to enrich the gas in their surrounding such that further star formation will be associated with a less top-heavy IMF. At the same time the star-burst will enshroud itself by dust produced by the evolving stars. Such a cluster forms during the first few Myr with an average SFR of only $\approx 100 M_{\odot}/\text{yr}$ with the SFR picking up over time as the rest of the spheroid forms.

During the first about 50 Myr the star-burst cluster would be quasar-like (Jerabkova et al. 2017, Sec. 3.4) and may suppress further star formation within its vicinity (Ploekinger et al. 2019). One extreme assumption would be that it blows off a large fraction of its mass ($\gtrsim 75$ per cent, table 3 in Dabringhausen et al. 2010) in the form of stellar winds and combined supernova ejecta thus probably driving a massive metal-rich outflow ($\dot{M}_{\text{off}} \gtrsim 1 M_{\odot}/\text{yr}$) and would, in this case, expand by a factor of more than ten (Dabringhausen et al. 2010). This object does not dissolve despite losing more than 75 per cent of its initial mass (in the form of winds and supernova ejecta) because it is confined at the centre of the potential well of the forming spheroid. It is also likely that such a central cluster will not be able to blow out its stellar ejecta and residual gas due to the large escape speed from its centre (in the above example, $v_{\text{esc}} \gtrsim 400$ km/s). The binding energy of the central cluster $\propto M_{\text{cluster}}^2$ while the feedback energy scales almost linearly with M_{cluster} such that for $M_{\text{cluster}} \gtrsim 10^7 M_{\odot}$ the feedback energy will not suffice to remove the residual gas (fig. 3 in Baumgardt et al. 2008 and sec. 4.6 in Wang et al. 2020). An example of a low-redshift star-burst where the high rate of central core-collapse supernovae per year, detected at radio wavelengths, is unable to blow out the gas is evident in Arp 220 (Lonsdale et al. 2006; Dabringhausen et al. 2012).

The star-burst cluster is most likely to form mass-segregated (Pavlík et al. 2019 and references therein). If not, it will mass-segregate; idealised N-body simulations having shown that the BH sub-system shrinks to about 10 per cent of the original radius of the cluster but on a Gyr time-scale (Breen & Hoggie 2013a). During the explosion a BH may receive a substantial kick if the explosion is not symmetric but the envelope fall back fraction limits the velocities (e.g. Fryer et al. 2012; Belczynski et al. 2016). Given the deep potential well of the case in study here, it is safe to assume all BHs are retained (Pavlík et al. 2018; Jerabkova et al. 2017; Wang 2020). Independently of primordial mass-segregation,

the whole BH-containing cluster will shrink due to gas inflow, as discussed below (but neglecting the stars; the stars would aid in the shrinkage due to the deeper potential and would lead to a faster mass growth of the merging BHs so neglecting them here leads to a conservative estimate of the shrinking time).

When the supernova explosions cease in the central hyper-massive cluster, it is unavoidable that the gas from which the rest of the spheroid is still forming falls into it (Pflamm-Altenburg & Kroupa 2009). The evolving starburst which forms the spheroid will not blow out all the gas as it is confined by the potential of the baryonic component and its particle or phantom dark matter halo (Famaey & McGaugh 2012; Lüghausen et al. 2013). The survey of 1957 massive galaxies at $1 < z < 3$ by Ramasawmy et al. (2019) shows the feedback from their accreting SMBHs to not measurably affect their star formation and thus their gas content.

The time scale of gas in-fall is given by the free-fall or dynamical time,

$$t_{\text{dyn}} \approx \left(\frac{3\pi}{32G\rho} \right)^{1/2}, \quad (10)$$

with the density being (assuming a constant-density sphere) $\rho = 3M/(4\pi R^3)$ and $G \approx 0.0045 \text{ pc } M_{\odot}^{-1}/(\text{pc}/\text{Myr})^2$ is the gravitational constant. Assuming for the spheroid a mass $M = 10^{11} M_{\odot}$ and a characteristic radius of $R = 2000 \text{ pc}$ (Fujimoto et al. 2020) and for the cluster $M = 10^8 M_{\odot}$, $R = 10 \text{ pc}$ (Dabringhausen et al. 2008), $t_{\text{dyn}} = 4.7 \text{ Myr}$ and 0.05 Myr , respectively. The in-falling gas is likely to form stars. Assuming a star-formation efficiency of 10-30 per cent as is observed in the embedded clusters in molecular clouds of the Milky Way (e.g. Megeath et al. 2016) (in actuality it may be smaller since the star-formation efficiency probably increases with the cooling capability of the gas and thus with its metallicity), most of the in-falling mass will remain gaseous, especially so since gas will continue falling towards the centre as stars form from it.

As t_{dyn} is less than about 10 Myr, gas inflow can be assumed to be essentially instantaneous. The potential of a non-ionising cluster can draw-in a cooling flow (Pflamm-Altenburg & Kroupa 2009; Bekki & Mackey 2009). Observational evidence for gas accretion onto clusters triggering new star formation has been found (For & Bekki 2017). For a global $SFR = 3 \times 10^3 M_{\odot}/\text{yr}$ about $3 \times 10^{12} M_{\odot}$ of gas collapses to the spheroid in 340 Myr assuming the star-formation efficiency $\epsilon \approx 30$ per cent. The innermost 1 per cent mass radius is thus likely to have an inflow rate of $\dot{M}_{\text{iff}} \approx 10^8 M_{\odot}/\text{Myr}$. An example of an observed significant mass inflow into the central region hosting an active galactic nucleus is the galaxy M81 at a distance of about 3.6 Mpc (Devereux 2019). The interested reader is referred to Boco et al. (2020) who discuss further observational evidence for gas-rich central galactic regions. The main conclusion here is that the central cluster of stellar-mass BHs will be in a significant star-forming gaseous environment during the downsizing time-scale, Eq. 1, which is the formation time-scale of the spheroid.

This leads to three connected effects: (i) the cluster shrinks due to friction of the BHs on the gas, (ii) the cluster shrinks due to the inflowing gas (this is the inverse of the expansion of a star cluster when it expels its residual gas),

and (iii) the stellar-mass black holes (BHs) in the nuclear cluster undergo mass growth through accretion.

We assume the stars and other remnants in the cluster can be ignored as their individual masses are much smaller than those of the stellar BHs and thus they are either absorbed by the BHs (enhancing their mass growth) or they are pushed outside of R via energy equipartition (Banerjee & Kroupa 2011; Breen & Heggie 2013a). The $\gtrsim 50 \text{ Myr}$ old cluster is assumed to consist of N BHs, each of mass m_{BH} . The example given below Eq. 3 has, for $m_{\text{BH}} \approx 100 M_{\odot}$ (ultra-low metallicity, Banerjee et al. 2019), $N \approx 10^{4.3}$ ($\beta = 2.4$) to $N \approx 10^{6.1}$ ($\beta = 2.0$). A gravitational N-body system in a tidal field loses its members through energy-equipartition driven evaporation as ejections through binary encounters are rare (Heggie & Hut 2003; Baumgardt & Makino 2003). In the present context, in 200 Myr this cluster will have lost a negligible fraction of its BHs to galactocentric distances larger than R . Some of these may return due to dynamical friction on the dense stellar component in the inner region of the forming spheroid (see Breen & Heggie 2013a for a further discussion). Assuming no BHs are lost is thus a reasonable assumption in the present context.

This section discusses the processes acting as such a cluster of BHs evolves. The aim here is to understand if, at least in principle, the evolution of a cluster of BHs subject to the presence and accretion of gas onto it from the forming host galaxy may lead to the formation of an SMBH-seed on an astrophysically relevant (within a few hundred Myr) time-scale. The role of binary BHs which form near the core of the BH cluster is discussed in Sec. 4.1. In Sec. 4.2 it is shown that the BH sub-cluster will core-collapse once a critical density is reached because the heating from binary BHs ceases to be an energy source. The evolution of the BH sub-cluster taking into account gas drag is calculated in Sec. 4.3. We emphasise that we only touch upon the relevant physical processes. Detailed treatment awaits significant future research involving radiation transport and relativistic stellar dynamics.

4.1 Heating from dynamically formed BH–BH binaries

The physical situation we are studying is as follows: the central region of the forming spheroid contains, after the first $\approx 50 \text{ Myr}$, a cluster of N BHs. This cluster will tend to core collapse due to the energy-equipartition process. As the density of the BH sub-cluster increases the BHs form binaries through triple encounters. These triple and subsequent encounters involving the BH binaries stabilise the cluster against core collapse as the binaries are a heating source (e.g. Hills 1975; Heggie 1975; Miller & Hamilton 2002; Banerjee et al. 2010; Miller & Davies 2012; Strader et al. 2012; Fujii & Portegies Zwart 2014; Giersz et al. 2015). That the energy-equipartition-driven core collapse of a star cluster is halted through energy production by binary encounters leading to gravothermal oscillations rather than runaway collapse of the core has been shown for the first time by means of numerical models by Giersz & Spurzem (2003).

Thus a BH sub-cluster evolves such that the BH population self-depletes through the dynamical formation of BH binaries in triple encounters which, after their formation, exchange energy with a third BH, leading to expulsion of

the binary and single BH to distances $> R$ (Banerjee 2017). Due to the deep potential well, the massive nuclear cluster will retain most of its BHs (for a more detailed discussion on BH retainment see Jerabkova et al. 2017; Pavlík et al. 2018), but the binary activity will halt core collapse of the BH sub-cluster. At the same time the cluster may shrink as gas keeps falling into it (Sec. 4.3), enhancing heating through binary activity.

According to Hénon's ζ principle (Hénon 1961, 1975), the energy generating rate of the core from encounters between singles/binaries with hard binaries is regulated by the bulk of the system. Such encounters transform internal binding energy of the binary into kinetic energy of the centre of mass motions (eq. 1 in Antonini et al. 2019, where the numerical coefficient (see also below) $\zeta \approx 0.0926$ for isolated systems, Hénon 1965, and $\zeta \approx 0.0743$ for tidally limited clusters, Hénon 1961) which supports the cluster against core collapse and thus leads to energy balance of the cluster. Based on this Hénon's ζ principle, Gieles et al. (2011) study the life cycle of GCs in the Milky Way and suggest that almost all GCs are in energy balance. This balanced evolution theory is also the basis for Monte-Carlo simulation codes for GCs (e.g. Hypki & Giersz 2013; Joshi et al. 2000) having been confirmed to work well via comparison with direct N -body simulations (e.g. Rodriguez et al. 2016). Using direct N -body simulations, Breen & Heggie (2013b) apply the balanced evolution theory to a system composed of a star cluster and a BH sub-cluster which generates the energy through binary BH encounters and Wang (2020) studies the implied dissolution rates of star clusters assuming top-heavy IMFs and thus enhanced BH contents.

The hard/soft binary boundary is (Heggie 1975; Hills 1975)

$$a_{\text{h/s}} = \frac{Gm_1m_2}{\langle m \rangle \sigma^2}. \quad (11)$$

A binary with component masses m_1, m_2 and with a semi-major axis $a > a_{\text{h/s}}$ is a soft binary and will be disrupted due to further encounters (e.g. Kroupa 1995). Thus only hard binaries with $a < a_{\text{h/s}}$ can survive. When the velocity dispersion of the BH sub-cluster, σ , increases, $a_{\text{h/s}}$ decreases. The heating process of the cluster through the binaries is via the energy exchange between the hard binaries encountering with other BHs and the cluster achieves energy balance. The binary-single encounter timescale is (Heggie & Hut 2003)

$$t_{\text{ce}} = \frac{\sigma}{8\pi G \rho_{\text{BH}} a}, \quad (12)$$

where ρ_{BH} is the total BH mass density in the cluster and a is the typical semi-major axis of a BH binary. t_{ce} becomes longer when σ increases or ρ_{BH} decreases.

The energy production rate through binary-BHs, $\dot{E}_{\text{bin,heat}}$, can be written for equal-mass BHs by adopting eq. 1 and 2 in Antonini et al. (2019) together with their equation for the total energy of the cluster, E (we do not use their eq. 3). For the cluster mass we assume $M_{\text{cl}} = M_{\text{g}} + M_{\text{BH},0}$, which is the gas mass plus mass in N equal-mass BHs, $M_{\text{g}} = \eta_{\text{g}} M_{\text{BH},0}$, $M_{\text{BH},0} = N m_{\text{BH}}$ for some number η_{g} . Their r_{h} we assume to be the characteristic radius of the BH sub-cluster, R , and following the assumption by Gieles et al. (2011) we adopt for the numerical coefficient $\zeta = 0.1$ which relates the energy production to the total energy and the

two-body relaxation time. The constant ψ depends on the mass spectrum (for a discussion see Antonini et al. 2019) and here $\psi = 1$ for equal-mass BHs. The Coulomb logarithm, $\ln \Lambda = \ln(N/2)$. Thus

$$\dot{E}_{\text{bin,heat}} = 0.145 \frac{G^{1.5} (1 + \eta_{\text{g}})^{1.5} m_{\text{BH}}^{2.5} N^{1.5}}{R^{2.5}} \ln \left(\frac{N}{2} \right). \quad (13)$$

Note that we ignore the rest of the stellar cluster in order to simplify the problem. That is, we assume the forming spheroid contains at its centre a cluster of N equal-mass BHs which is self-gravitating and in which binaries are formed dynamically which heat the cluster. Further assumptions are discussed as caveats in Sec. 8 and in particular in Sec. 8.3.

In a BH sub-cluster with a velocity dispersion larger than a critical value (Sec. 4.2), the dynamically formed BH binaries merge due to the radiation of gravitational waves before a further dynamical encounter with another BH because these binaries have a small encounter cross section. Three-body encounters which expel the BHs from the cluster thus cease to be an important physical process. Radiation of gravitational waves during the occurring BH mergers may also impart sufficient recoils to allow the merged BHs to escape to distances $> R$. Calculations which include gravitational redshift and space-time curvature scattering of gravitational waves suggest that recoil velocities are much less than 500 km/s (Favata et al. 2004). In a BH sub-cluster with $\sigma_{\text{h,BH}} > 100$ km/s a sufficient number of BHs are thus most probably retained despite the gravitational-wave recoils (see also Jerabkova et al. 2017; Pavlík et al. 2018). Runaway merging may proceed in this regime because further mergers between the retained growing merged BH and a stellar BH receive insignificant recoils. If the cluster has a velocity dispersion larger than a critical value (≥ 500 km/s, Sec. 4.2) the BH binaries typically merge through the radiation of gravitational waves before the next encounter and the binary BHs cease to be a heating source. When this occurs, the BH cluster starts to shrink without the core being able to generate sufficient energy to sustain balanced evolution.

4.2 Loss of support from BH binaries

Once the cluster of BHs reaches a critical density and velocity dispersion when the dynamically formed binaries are sufficiently tight to merge through radiation of gravitational waves on a timescale comparable to or faster than subsequent further encounters, the BH binaries cease to be the energy source opposing core collapse (in analogy to the final endothermic nuclear reactions in stars leading to catastrophic stellar collapse and therefore core-collapse supernovae). Balanced evolution breaks down and the cluster then collapses on a core-collapse time-scale, forming a singularity, i.e. the SMBH-seed containing a significant fraction of the BH sub-cluster mass (5 per cent in pure post-Newtonian N -body computations, Lee 1993; Kupi et al. 2006).

A hard BH binary can merge via gravitational wave (GW) radiation. The decay timescale of a BH binary (Peters 1964) is

$$t_{\text{gw}} = \frac{a^4}{4\beta}, \quad \text{where } \beta = \frac{64}{5} \frac{G^3 m_1 m_2 (m_1 + m_2)}{c^5}. \quad (14)$$

Eq. 14 estimates the decay timescale for a circular orbit

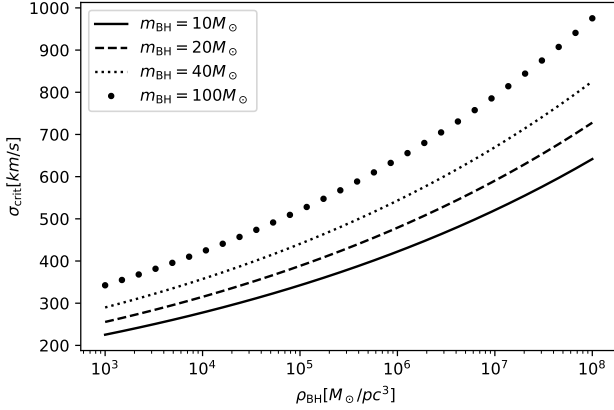


Figure 4. The velocity dispersion–density criterion (Eq. 17) for the condition when the BH binaries cease to be heating sources (above the curves) such that the BH cluster can continue to shrink due to gas drag w/o opposition by BH binary encounters. Different line styles indicate different BH masses, m_{BH} .

for a given a . For eccentric orbits, the merging timescale is shorter. Thus Eq. 14 provides a conservative, upper limit.

When a is sufficiently small, $t_{\text{ce}} > t_{\text{gw}}$ obtains. Such a binary merges before any additional encounter happens. This suggests that when σ is large enough in the core of the BH sub-cluster, $a_{\text{h/s}}$ can be sufficiently small such that $t_{\text{ce}} > t_{\text{gw}}$. In this case, once hard binaries form dynamically, they merge via GW radiation before they experience a sufficient number of encounters to transfer their binding energy to the kinetic energy of the field, i.e., the BH binaries stop being stellar-dynamical heating sources for the BH sub-cluster (Lee 1995; Kupi et al. 2006). When this occurs, it is expected that the energy balance cannot be established and collapse happens to a merged SMBH-seed.

The criterion $t_{\text{ce}} > t_{\text{gw}}$ results in

$$a < \left(\frac{\beta\sigma}{2\pi G\rho_{\text{BH}}} \right)^{1/5}. \quad (15)$$

By setting $a = a_{\text{h/s}}$, we can obtain a relation between σ and ρ_{BH} ,

$$\sigma^{11} > \frac{5}{32}\pi\rho_{\text{BH}} \frac{G^3(m_1m_2)^4c^5}{(m_1+m_2)\langle m \rangle^5}. \quad (16)$$

In a system with equal-mass BHs ($m_1 = m_2 = m_{\text{BH}}$), the relation can be simplified,

$$\sigma_{\text{crit}}^{11} = \frac{5}{64}\pi\rho_{\text{BH}}G^3m_{\text{BH}}^2c^5, \quad (17)$$

such that for σ (Eq. 24) larger than σ_{crit} the heating through binaries (Eq. 13) ceases to be relevant. With Eq. 17 we can obtain the criterion on σ_{crit} in dependence of ρ_{BH} when this occurs, as shown in Fig. 4.

According to Gürkan et al. (2004) and Fujii & Portegies Zwart (2014), a cluster with N BHs and an average BH mass of m_{BH} undergoes core collapse after a time $t_{\text{cc}} \approx 0.15 t_{\text{rc}}$,

where the core two-body-relaxation time-scale is

$$t_{\text{rc}} \approx \frac{0.065}{G^2 m_{\text{BH}} \ln \Lambda} \frac{\sigma_{\text{c}}^3}{\rho_{\text{c}}}. \quad (18)$$

As a rough approximation, the core-values for the velocity dispersion and density, $\sigma_{\text{c}}, \rho_{\text{c}}$, can be replaced by $\sigma_{\text{crit}}, \rho_{\text{BH}}$, respectively. A cluster of 10^5 BHs with an average mass of $50 M_{\odot}$ will, once it reaches a density of $\rho_{\text{BH}} \approx 10^8 M_{\odot}/\text{pc}^3$ and $\sigma \approx 700$ km/s, collapse within $t_{\text{cc}} \approx 3$ Myr.

Inserting Eq. 17 into Eq. 18,

$$\frac{t_{\text{cc}}}{\text{Myr}} \approx 1.2 \times 10^8 \frac{1}{\ln \Lambda} \left(\frac{m_{\text{BH}}}{M_{\odot}} \right)^{-\frac{5}{11}} \left(\frac{\rho_{\text{BH}}}{(M_{\odot}/\text{pc}^3)} \right)^{-\frac{8}{11}}. \quad (19)$$

The BH sub-cluster collapses faster though, because gas drag (Sec. 4.3) shrinks it in the absence of binary heating. Once σ reaches 1 per cent of the speed of light,

$$\sigma_{\text{rel}} \equiv 3000 \text{ km/s}, \quad (20)$$

the BH sub-cluster is referred to throughout this text as being in the relativistic state. This critical value is adopted here in view of the N-body work studying the relativistic collapse of BH clusters starting with comparable velocity dispersions (Lee 1993, 1995; Kupi et al. 2006).

4.3 Shrinkage of BH sub-cluster through gas drag

We consider a self-gravitating system consisting of BHs of total mass $M_{\text{BH}}(t) = Nm_{\text{BH}}(t)$ and a gas mass of

$$M_{\text{g}}(t) = (4/3)\pi R^3(t)\rho_{\text{g}}(t), \quad (21)$$

where the time dependence is explicitly written since the BHs may accrete from the gas and the cluster may accrete additional gas, $R(t)$ is the characteristic radius of the BH sub-cluster, and $\rho_{\text{g}}(t)$ is the gas mass volume density. The gas density becomes

$$\rho_{\text{g}}(t) = f_{\text{g}} \frac{3M_{\text{g}}(t)}{4\pi R^3(t)}, \quad (22)$$

where $f_{\text{g}} \approx 1$ covers the density actually not being constant throughout the cluster and that the characteristic radius R does not cover the whole cluster.

Assuming the BH sub-cluster to be close to virial equilibrium, i.e., the velocity dispersion σ being related to, R , the absolute value of the potential energy, E , is

$$E(t) = f_{\text{v}} \frac{G(M_{\text{g}}(t) + Nm_{\text{BH}}(t))^2}{R(t)} = Nm_{\text{BH}}(t)\sigma^2(t). \quad (23)$$

The dimensionless factor $f_{\text{v}} \approx 1$ and covers, e.g., a departure from virial equilibrium or a particular shape of the potential well. From this follows the velocity dispersion of the BHs (dropping from hereon the explicit time dependence),

$$\sigma = \left(f_{\text{v}} \frac{G(M_{\text{g}} + Nm_{\text{BH}})^2}{RNm_{\text{BH}}} \right)^{1/2}. \quad (24)$$

We further assume that the BHs dissipate their kinetic energy as they move through the gas medium. Dynamical friction will lead to a drag force on each BH of

$$F = \dot{p} = -4\pi f_{\Lambda} \ln \Lambda \rho_{\text{g}} \frac{G^2 m_{\text{BH}}^2}{v^2}, \quad (25)$$

which points in the direction opposite to the BH's motion. This first order approximation is sufficient for the current context; a similar formula can be derived within the framework of Bondi-Hoyle accretion onto a moving object (Sec. 8.1). In Eq. 25, v is the speed of the BH with respect to the gas, $f_\Lambda \approx 1$, the exact value of which depends on the particular derivation (e.g., in the case of Chandrasekhar dynamical friction, $f_\Lambda \approx \pi/3$) and $\ln \Lambda = \ln(R/b_{\min})$ is the Coulomb logarithm with b_{\min} being the physically relevant minimum gravitational encounter distance. The Coulomb logarithm can be estimated by equating the kinetic energy of a particle with its binding energy at minimum distance,

$$\ln \Lambda = \ln \frac{Rv^2}{2Gm_{\text{BH}}} . \quad (26)$$

For $v^2 \approx \sigma^2$ and for a self-gravitating system near virial equilibrium, $\ln \Lambda = \ln(N/2)$ is a good approximation. The drag force (Eq. 25) will lead to a decrease (dissipation) of the BH's (kinetic) energy,

$$\dot{E}_{\text{BH}} = v\dot{p} = -4\pi f_\Lambda \ln(N/2) \rho_g \frac{G^2 m_{\text{BH}}^2}{v} . \quad (27)$$

Considering a cluster of N bodies of mass m_{BH} and since $v \approx \sigma$, the net energy dissipation per unit time is estimated as

$$\dot{E}_{\text{diss}} = -4\pi f_\Lambda \ln(N/2) \rho_g \frac{NG^2 m_{\text{BH}}^2}{\sigma} . \quad (28)$$

The energy generation rate due to binary heating is given by Eq. 13 such that the overall rate of change of binding energy of the BH sub-cluster becomes

$$\dot{E} = \dot{E}_{\text{diss}} + \dot{E}_{\text{bin,heat}} . \quad (29)$$

From Eq. 23 follows (assuming $N = \text{constant}$)

$$\dot{R} = \left(\frac{\dot{E}}{f_v G} - \frac{2}{R} (M_g + N m_{\text{BH}}) (\dot{M}_g + N \dot{m}_{\text{BH}}) \right) \frac{R^2}{(M_g + N m_{\text{BH}})^2} . \quad (30)$$

Note that if the cluster of BHs accretes gas then $\dot{M}_g > 0$ and the cluster shrinks (the inverse of gas expulsion). It also shrinks due to gas drag, since $\dot{E}_{\text{diss}} < 0$, but will expand if binary heating dominates. This is the case in the absence of gas ($E_{\text{diss}} = 0$, neglecting other energy dissipation mechanisms for now).

Note also that if the binary heating just balances the energy dissipation through gas drag, $\dot{E}_{\text{diss}} + \dot{E}_{\text{bin,heat}} = 0$, it follows, with Eq. 22 and 24 and assuming the gas mass within R is a constant fraction or multiple, η_g , of the BH cluster mass, $M_g = \eta_g N m_{\text{BH}}$, that

$$\frac{\eta_g}{(1 + \eta_g)^{2.5}} = 0.0483 . \quad (31)$$

Thus, for $\eta_g < 0.055$ and for $\eta_g > 5.78$ the BH cluster expands because binary heating dominates over gas drag, while for values in between the cluster contracts. At large η_g the velocity dispersion, σ , becomes too large for gas drag to be significant (Eq. 28). For large values of η_g the BH sub-cluster may also be in the relativistic regime (Eq. 20) initially, experiencing core-collapse and thus runaway BH–BH merging within 10–15 median two body relaxation times as a conse-

quence of energy loss through the emission of gravitational waves (Kupi et al. 2006). The collapse may be much faster though if gas falls in from the forming and evolving spheroid.

Eq. 30 will be used to investigate the shrinkage of the BH sub-cluster.

4.4 Summary

The equation governing the radius of the BH sub-cluster (Eq. 30) has been derived taking into account the heating through dynamically formed BH–BH binaries (Eq. 13) and thus the strive towards expansion of R , loss of their support when the velocity dispersion of the BH sub-cluster surpasses a critical value (Eq. 17) and the effect of gas on shrinking the cluster (Eq. 28). If a fraction η_g of the BH sub-cluster mass is in gas, then for $\eta_g < 0.06$ and $\eta_g > 6$ binary BH–BH heating drives the cluster towards expansion. Nevertheless, for $\eta_g > 6$ the BH sub-cluster may be in the relativistic state (Eq. 20) initially. When the BH sub-cluster reaches, or is, in this state, it will collapse within 10–15 median two-body relaxation times, forming a runaway merger through gravitational-wave emitting BH–BH encounters comprising about 5 per cent of the BH sub-cluster mass (Lee 1993; Kupi et al. 2006). This collapse time is likely shorter and the SMBH-seed mass will be likely larger if gas from the forming spheroid continues to fall onto the BH sub-cluster. This phase of the evolution remains to be understood though.

5 THE SHRINKING BH SUB-CLUSTER

The evolution of the BH sub-cluster through binary heating and gas drag is calculated in Sec. 5.1. The results are discussed in the context of other, independent, work in Sec. 5.2, and Sec. 5.3 contains a brief summary of this section.

5.1 Solutions

The aim is to compute the radius of the BH sub-cluster in order to find the time, t_{rel} , in initial BH cluster radius and mass ($R_0, M_{\text{BH},0}$) space when the BH cluster reaches the relativistic state (Eq. 20). During the evolution we also note the time, t_{crit} , when the condition given by Eq. 17 on its velocity dispersion (Eq. 24) is reached, i.e. when the BH binaries cease to be a heating source. The mass of the BH sub-cluster is assumed to be constant, $M_{\text{BH}}(t) = M_{\text{BH},0} = N m_{\text{BH}}$ (see Sec. 8.1).

We assume the BH sub-cluster is embedded in gas of constant total mass $M_g = \eta_g N m_{\text{BH}}$ within $R(t)$ for different values of η_g and that $\dot{m}_{\text{BH}} = 0$. The gas mass is assumed to be constant within $R(t)$ in a rough approximation of the gas accretion from the forming spheroid being balanced by feedback from the BH sub-cluster (see Sec. 8 for a further discussion).

The differential equation for the evolution of $R(t)$ (Eq. 30) is integrated with the python scipy library function called ODEINT (Virtanen et al. 2019) for solving systems of the form $dy/dt = f(y)$. The library is based on the ODEPACK fortran77 ordinary differential equation solver and uses the LSODA package (Hindmarsh 1983; Radhakrishnan & Hindmarsh 1993; Brown & Hindmarsh 1989). It uses the

dense or banded Jacobian for stiff problems and automatically evaluates if the system is stiff or non-stiff.

In order to map-out the parameter space we solve the equation $\dot{R}(t)$ (Eq. 30) for $R(t)$ for an equidistant grid of the parameters $N = M_{\text{BH},0}/m_{\text{BH}}$ (from 10^3 to 10^7 with 100 points in \log_{10} space), R_0 (between 0.5 and 10 pc in linear space with 100 points) and for several values of m_{BH} and η_g (Fig. 8). To solve the equation efficiently the following procedure is applied for each set of parameters ($M_{\text{BH},0}, R_0, m_{\text{BH}}, \eta_g$):

(i) If the system is initially relativistic it is noted and we move to the next set of parameters. This means its initial condition (Eq. 24) fulfils Eq. 20, i.e. $\sigma \geq \sigma_{\text{rel}}$.

(ii) In the case that the system is not initially relativistic, at first $R(t)$ is found for the array ranging in time from $t = 10^3$ Myr to $t = 10^4$ Myr in 10^6 log-steps to evaluate the nature of the given solution. We can thus estimate the time-scale on which the radius evolves. In case the system is collapsing too slowly, that is, if this characteristic time scale is longer than 1 Gyr, then this is noted and we continue with the next set of parameters.

(iii) In the case that the characteristic time scale is shorter than 1 Gyr we compute a finer grid for $R(t)$ and identify the time, t_{crit} , when the BH binaries cease to heat the cluster (Eq. 17) and the time, t_{rel} , when the BH cluster reaches the relativistic state (Eq. 20). The former time is noted for interest, but it is the latter time that we are mostly interested in.

The computation of a whole grid (as seen in one of the panels in Fig. 8) takes about 2-6 hours of CPU time on a modern PC with a 2.8 GHz QC i7 processor.

An example of the evolution of the radius of the BH sub-cluster, $R(t)$, is visualised in Fig. 5 which demonstrates a contracting case. For the latter, the ratio of the energy dissipation through gas drag to the heating of the cluster through binary BH activity is plotted in Fig. 6. It demonstrates that, while the dissipation dominates initially, binary heating becomes more significant as the radius shrinks. The corresponding evolution of the velocity dispersion of the BH sub-cluster in comparison to the critical condition when binary heating ceases are shown in Fig. 7.

Fig. 8 delineates the different behaviour in $R_0, M_{\text{BH},0} = M_{\text{BH}}$ space. For the parameters of the upper four panels ($\eta_g = 0.1$ and 1), the whole shown space leads to contracting solutions, i.e., heating through dynamically formed BH-BH binaries is smaller than the gas drag which the BHs experience in the BH sub-cluster. In the light blue region the shrinking time is longer than a Gyr. But even with a moderate gas fraction ($0.1 < \eta_g < 1$), BH sub-clusters with $R_0 \lesssim 1.5 - 4$ pc and $M_{\text{BH},0} \gtrsim 10^4 M_{\odot}$ reach the relativistic state within much less than a Gyr. As η_g or m_{BH} increases, the collapsing solution space increases significantly. For the cosmologically relevant cases ($m_{\text{BH}} = 100 M_{\odot}$ and $\eta_g \approx \text{few}$), BH clusters with $R_0 \lesssim 6$ pc and $M_{\text{BH},0} \approx 10^5 M_{\odot}$ have $t_{\text{rel}} < 300$ Myr.

Once in the relativistic state and if gas plays no role, the BH sub-cluster experiences core-collapse within 10–15 median two-body relaxation times (Lee 1993, 1995; Kupi et al. 2006), i.e., $t_{\text{collapse}}/t_{\text{HX}} \approx 10 - 15$ with $t_{\text{HX}} \approx t_{\text{cross}} N/\ln(N/2)$ and the crossing time $t_{\text{cross}} = 2R/\sigma$. Taking a conservative

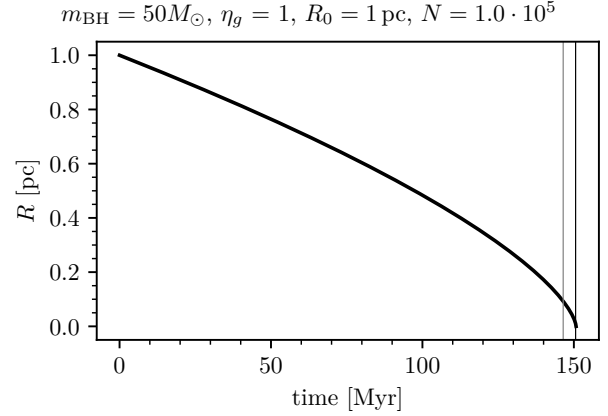


Figure 5. The evolution of the cluster radius, $R(t)$, for $\eta_g = 1.0$, $m_{\text{BH}} = 50 M_{\odot}$, $M_{\text{BH},0} = 5 \times 10^6 M_{\odot}$ and $R_0 = 1$ pc. The cluster of BHs contracts because gas drag outweighs binary heating. See Fig. 6 for the ratio of the rates of energy change due to gas drag and binary heating. The vertical thin grey line represents the time, t_{crit} , when binary heating ceases to be relevant (Eq. 17) and the vertical thick line shows the time, t_{rel} , when the BH cluster reaches the relativistic state (Eq. 20).

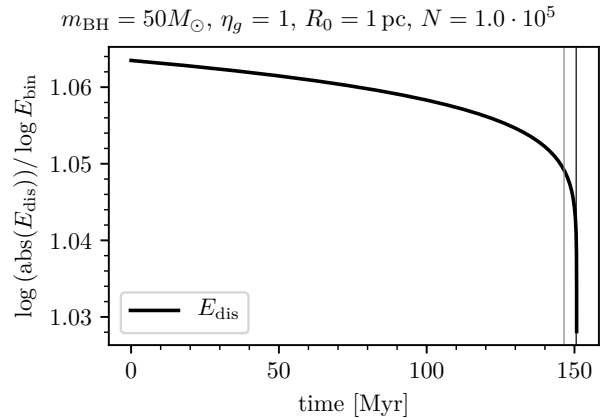


Figure 6. The ratio of the rates of energy change due to gas drag and binary heating for the parameters as in Fig. 5. The ratio of the \log_{10} values of $|\dot{E}_{\text{dis}}|$ and $\dot{E}_{\text{bin,heat}}$ is larger than one because gas drag outweighs binary heating. The ratio decreases because binary heating becomes increasingly significant as the cluster shrinks forming more energetic binaries. The vertical lines have the same meaning as in Fig. 5.

estimate,

$$t_{\text{collapse}}/\text{Myr} \approx \frac{15}{\ln(0.5 M_{\text{BH}}/m_{\text{BH}})} \frac{M_{\text{BH}}}{m_{\text{BH}}} \frac{2 R_{\text{rel}}/\text{pc}}{\sigma_{\text{rel}}/(\text{km/s})}. \quad (32)$$

The radius of the BH cluster in this state is, by Eq. 24,

$$R_{\text{rel}}/\text{pc} \approx \frac{M_{\text{BH}}}{2 \times 10^9 M_{\odot}} (1 + \eta_g)^2. \quad (33)$$

Thus, for example, for $M_{\text{BH},0} = 10^7 M_{\odot}$, $m_{\text{BH}} = 10 M_{\odot}$, $\eta_g = 1$, $R_{\text{rel}} \approx 2 \times 10^{-2}$ pc and $t_{\text{collapse}} \approx 15$ Myr. In reality, the collapse time is likely to be shorter still since the BHs will have different masses and gas drag, accretion and heating is likely to contribute to cluster shrinkage.

Thus, in this state the BH cluster core collapses through

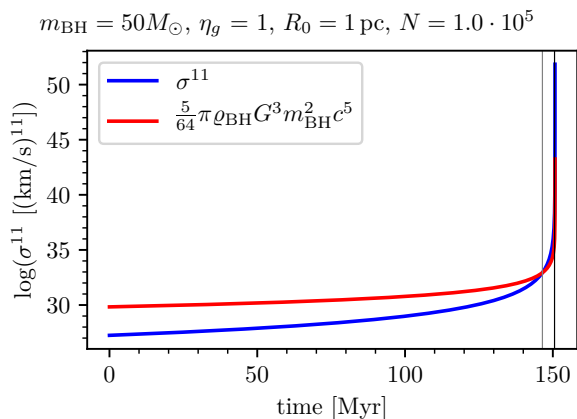


Figure 7. The evolution of the velocity dispersion (Eq. 24, blue line) and of the condition when binaries cease to be a heating source (Eq. 17, red line) for the parameters as in Fig. 5. The velocity dispersion increases as the cluster plus gas cloud shrinks. When the two lines intersect (the left vertical line) binary heating ceases to be active. The vertical lines have the same meaning as in Fig. 5. Note that $\log = \log_{10}$.

the radiation of gravitational waves in $\lesssim 15$ Myr. An independent estimate for the speed of the final relativistic collapse can be obtained as follows: eq. 15 in Lee (1993) implies a collapse time of about 10^5 yr for 10^6 BHs, $m_{\text{BH}} = 10 M_{\odot}$ and $\sigma = 3000$ km/s. A comparable relativistic collapse time scale of about 600 crossing times from that state is obtained with N-body simulations involving higher-order post-Newtonian terms (Kupi et al. 2006; e.g. within 0.3×10^5 yr for $R = 1$ pc). Thus, once the relativistic state is reached, the BH sub-cluster can be assumed to essentially collapse near to instantly to a SMBH-seed (i.e. $t_{\text{collapse}} \ll t_{\text{rel}}$). About 5 per cent of the BH sub-cluster mass merges to the SMBH-seed in this state (Lee 1993; Kupi et al. 2006), but the inflow of gas and consequently the additional orbital shrinkage of the BHs is likely to increase this to a significant fraction of $M_{\text{BH},0}$.

The upper two panels of Fig. 8 also demonstrate that as $M_{\text{BH},0}$ increases, the R_0 values decrease for which $t_{\text{rel}} < 300$ Myr. This results from gas drag becoming less efficient for larger σ (Eq. 28).

The lowest two panels (with $\eta_g = 8$) demonstrate that none of the solutions lead to a shrinking $R(t)$ (most of the $R_0, M_{\text{BH},0}$ space being dark blue, i.e. expanding, by Eq. 31). For $M_{\text{BH},0} \gtrsim 10^7 M_{\odot}$ and certain small to large values of R_0 (shown as the brown region) the BH sub-clusters are initially in the relativistic regime. For these, collapse to a SMBH-seed is also inevitable and will occur faster than the core-collapse time scale of 10–15 median two-body relaxation times since the gas accretion onto the BHs speeds up the core collapse (Leigh et al. 2013). For sufficiently small R_0 this BH–BH runaway merging time may be shorter than a few Myr. The extreme (brown) regions in Fig. 8 are not accessible to the present modelling though.

5.2 Related work

Sec. 5.1 has shown that the BH sub-cluster which forms within the first massive star-burst cluster at the centre of

the later spheroid can shrink within about 200 Myr to the relativistic state due to the gas which falls into it from the forming spheroid.

The results obtained here are in line with the work of Leigh et al. (2013) who discussed that gas-accretion onto a BH sub-cluster speeds-up its core collapse due to the mass-growth of the BHs. But the mass-growth is Eddington-limited (see Sec. 8.1), limiting the mass-growth within the time $\Delta\tau$. Our results are also in line with the suggestion by Davies et al. (2011) and Boco et al. (2020)³ who point out that the shrinkage of a cluster with BHs through the accretion of gas onto it may enhance the formation of a SMBH-seed. The difference to their work is that here much more massive star burst clusters are considered (consistent with observations, given the SFRs of galaxies) and that this work suggests a direct link between the formation of the spheroid to the SMBH-seed via the stellar population, as derived from published scalings of the stellar populations and the SFR of the forming spheroid via the IGIMF theory (Sec. 3.3). Also, the here presented work relaxes the need for $\eta_g > 1$ to reach sufficient compression for SMBH-seed formation (Davies et al. 2011) to values where the gas mass needed is smaller than that of the BH sub-cluster ($\eta_g < 1$). Also, here, for the first time, explicit time-scales are associated with the process in view of the formation times of the massive spheroids and the populations of stars they ought to contain if star formation in the early Universe follows similar rules as inferred from local populations, including low-metallicity ones.

The results obtained here are thus well consistent with the work of Davies et al. (2011); Boco et al. (2020) and of Leigh et al. (2013), and this work allows for the first time a quantification of the expected scaling of the SMBH-seed mass with the mass of the forming spheroid, as shown in Fig. 11 below.

5.3 Summary

Solutions for the evolution of the radius of the BH sub-cluster are obtained by taking into account heating through dynamically formed BH–BH binaries and dissipation of BH orbital energy through gas which presumably is in the BH sub-cluster from the forming spheroid. The gas mass is assumed to be proportional to the BH sub-cluster mass within R , mimicking very roughly the self-regulation through feedback and accretion from the forming spheroid. The BH sub-cluster can shrink to the relativistic state when its equation of state changes from an incompressible one to a pressureless one. At this point it collapses within 10–15 two body relaxation times by emitting gravitational waves. The calculations indicate that for viable initial values, $R_0, M_{\text{BH},0}$, the total time of R shrinking to a SMBH-seed mass occurs on an astrophysically interesting (< 200 Myr) time scale.

³ The work presented here was conducted with neither prior knowledge of the work of Davies et al. (2011); Leigh et al. (2013) nor of that by Boco et al. (2020). These were discovered during the writing-up stage of this manuscript.

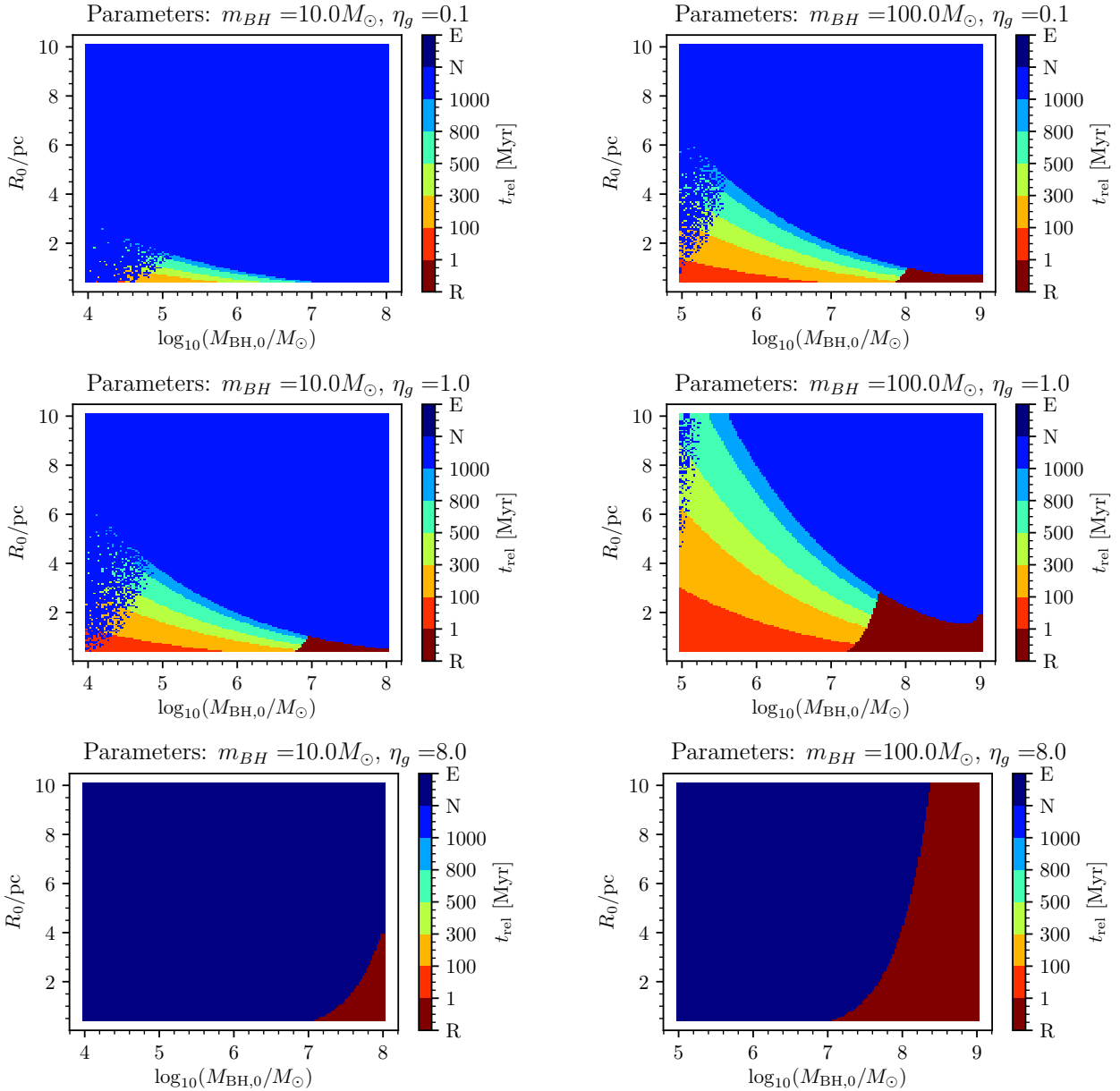


Figure 8. The time, t_{rel} , in $R_0, M_{\text{BH},0} = N m_{\text{BH}}$ space. t_{rel} is in Myr and is coloured according to the key: the middle- and dark-blue regions indicate, respectively, a shrinkage time longer than 1 Gyr and expansion, the brown region indicates the cluster to reach the relativistic state within 1 Myr. Note that for $\eta_g < 0.055$ the BH sub-cluster expands. For $\eta_g > 5.78$ (see Eq. 31) it may also formally expand, but for $M_{\text{BH},0} > 10^7 M_\odot$ and for a large fraction of the parameter space (shown here in brown in the bottom two panels) the BH sub-cluster is already initially in the relativistic state and will collapse and form a runaway BH merger within 10–15 median two-body relaxation times. For this to occur gas is therefore not needed, but the gas drag shortens this time. Note also that the $R_0 - M_{\text{BH},0}$ range for collapse to a SMBH seed becomes smaller for larger $M_{\text{BH},0}$ because the larger velocity dispersion leads to less efficient gas drag of the BHs.

6 THE GALAXY–SMBH CORRELATION

Given the correlations between the most massive forming star cluster ($M_{\text{ecc,max}}$), its stellar population (IMF) and the mass of the forming spheroid (M_{gal}) discussed in Secs 2 and 3, it is now possible to quantify the expected relation between the present-day luminous mass, M_{gal} , of the spheroid and the mass of the SMBH-seed which forms in the most massive cluster near the centre of an emerging

spheroid through the relativistic collapse of its BH sub-cluster (Sec. 4).

We proceed as follows: For a value of the total (i.e. initial) stellar mass of the spheroid, M_{gal} , the time-scale, $\Delta\tau$, of its formation is calculated (Eq. 1). Assuming the SFR remains constant over this time-scale, $SFR = M_{\text{gal}}/\Delta\tau$ (Fig. 9). The total stellar mass of the spheroid which forms over the downsizing time, M_{gal} , is plotted in Fig. 10 as a function of the final luminous mass after about 12 Gyr of evolution,

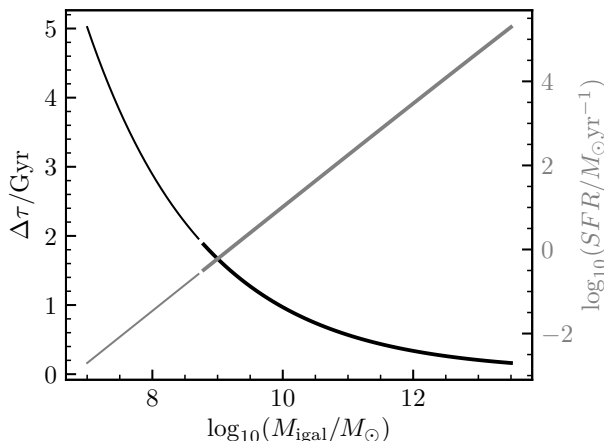


Figure 9. The downsizing time, $\Delta\tau$ (Eq. 1, left axis) and the SFR (right axis) of a spheroid with a total mass in stars of M_{igal} . The thick and thin lines with gap in between are explained in Fig. 11.

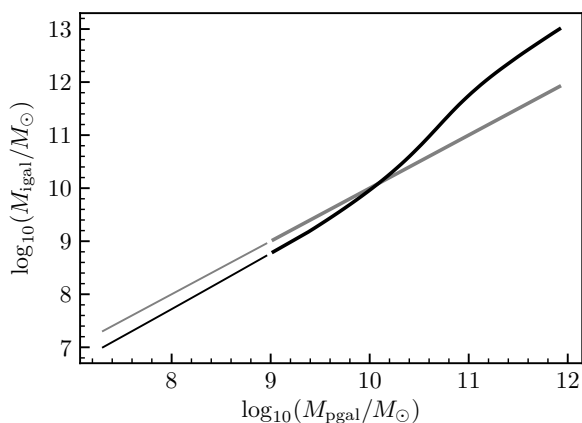


Figure 10. The total stellar mass formed in the spheroid, M_{igal} , as a function of its present-day luminous mass, M_{pgal} , assuming the systematically varying IMF in each embedded cluster as given by Eq. 7 (Marks et al. 2012; see also Yan et al. 2017; Jerabkova et al. 2018 and Dabringhausen 2019 for more detailed models). An invariant canonical IMF (Sec. 3.1) leads to a constant ratio of $M_{\text{pgal}}/M_{\text{igal}} \approx 0.7$ (Baumgardt & Makino 2003). The thick and thin lines with gap in between are explained in Fig. 11. Note the upwards turn of the thick line towards larger masses. This is due to the increasingly top-heavy gwIMF with increasing SFR and thus a decreasing $M_{\text{pgal}}/M_{\text{igal}}$ ratio. The gray thin and thick line is the 1:1 relation, the gap having merely an orientative meaning).

M_{pgal} , approximated here as the total mass in stars less massive than $1 M_{\odot}$.

Given a SFR, $M_{\text{ecl,max}}$ follows from the WKL relation (Eq. 2) or more generally from Eq. 5. Under the assumptions made in Sec. 2, as the spheroid assembles, a number of N_{gen} such clusters form (Eq. 6). But only the first-formed starburst cluster is likely to be the most relevant (Ploekinger et al. 2019), as only it will have a very top-heavy IMF as subsequently formed starburst clusters will already be metal-enriched and will therefore probably have an IMF which is closer to the canonical one. From the expected number of stars more massive than $20 M_{\odot}$, the mass of the BH sub-

cluster within $M_{\text{ecl,max}}$ follows (Fig. 2). This BH sub-cluster is expected to be present within about 50 Myr of the formation of the $M_{\text{ecl,max}}$ cluster (see also Sec. 7). We also assume, as a point of reference, an invariant canonical IMF (Sec. 3.1).

As gas from the forming spheroid falls into the central cluster, its BH sub-cluster (and most realistically the whole cluster) shrinks. For those cases where the BH sub-cluster undergoes a relativistic collapse within 0.1–0.3 Gyr (Fig. 8), Fig. 11 shows the expected SMBH-seed–spheroid mass relation. Impressively, the slope of the analytical relation is very comparable to the observational data. Assuming that only 5 per cent of the BH sub-cluster in the first cluster with a mass $M_{\text{ecl,max}}$ becomes the SMBH-seed, all such seeds need to grow by three orders of magnitude in mass ($f_{\text{growth}} = 10^3$) to reach the observed SMBH masses shown as the data points in Fig. 11. This can be achieved by Eddington-limited constant super-Eddington accretion ($\epsilon_r = 0.1$, Sec. 8.1) by the SMBH-seeds within 347 Myr, since, from Eq. 45, the accretion time is

$$t_{\text{accr}} = (452/9) \ln(f_{\text{growth}}). \quad (34)$$

We emphasise that $t_{\text{accr}} < \Delta\tau$, i.e., *the model leads to the self-consistent result that the required accretion time to reach the observed SMBH masses at a given M_{pgal} is shorter than or comparable to the downsizing, i.e. spheroid formation, time scale (Eq. 1). This is a rather remarkable result of this model needing to be emphasised.* In their review, Mayer & Bonoli (2019) point out the lack of direct radiation hydrodynamical calculations on nuclear or sub-nuclear scales that show that this growth mode can be sustained up to the extremely large BH masses needed to explain the bright high- z quasars. In this case the only advantage of the present BH merging model over that of population III remnant black holes would be that the present model leads to larger SMBH seed masses and thus shorter required accretion sustainment times and that the physical pathway of explaining SMBH seeds via gas-promoted merging BHs might, arguably, be better understood than the more uncertain physics of population III stars. However, other than that, both solution-ansatze suffer from the same remaining problem of SMBH-seed growth to the SMBH masses observed, the present model to a significantly lesser extent though. For larger SMBH-seed masses (the other coloured curves in Fig. 11) the required accretion time becomes shorter or the accretion rate can be sub-Eddington. The above holds true also if the IMF does not vary, as shown by Fig. 11. But in this case the slope of the SMBH-seed–spheroid mass is somewhat flatter, and the required growth factors, f_{growth} , are larger, but still requiring growth times of less than a Gyr to match the observed relation.

Noteworthy is that if all centrally formed $M_{\text{ecl,max}}$ clusters merge to one cluster, then their combined mass continues the same relation as that of the SMBH masses to $M_{\text{pgal}} \lesssim 10^9 M_{\odot}$ for $\beta = 2.0$ (Fig. 11) and to $M_{\text{pgal}} \lesssim 10^{9.6} M_{\odot}$ for $\beta = 2.4$ (Fig. 18). This is reminiscent of the central-massive-object(CMO)–spheroid-mass correlation found by Wehner & Harris (2006) and further discussed by Capuzzo-Dolcetta & Tosta e Melo (2017). This single continuous relation between the CMO mass and the luminosity of their hosting spheroid (Wehner & Harris 2006) would, in the present context, be consistent with the assembly of the

spheroid: as the spheroid forms over the downsizing time $\Delta\tau$, the inner, nuclear-cluster-hosting region acquires a baryonic mass amounting to $N_{\text{gen}} M_{\text{ecl,max}}$ (Eq. 6). The correlation for dwarf elliptical galaxies and their nuclear cluster (the upper grey dashed line in Figs 11 and 18) may thus be explained. This amount of mass infall into the central region would also lead to the compression and growth of the SMBH-seed mass needed to reach the data points shown in both figures. While the nuclear regions of spheroids form within the downsizing time scale, late-type galaxies continue to grow in mass (e.g. Speagle et al. 2014; Kroupa et al. 2020) such that their nuclear star cluster is likely to grow through in-situ star formation and mergers with freshly formed massive clusters beyond the mass of that assembled during the initial formation of its spheroidal component. Additional slow growth of the SMBH through the disruption of stars continues until the present, most efficiently though for low-mass SMBHs (Brockamp et al. 2011). This would lead to a flatter $M_{\text{CMO}} - M_{\text{gal}}$ relation for late-type galaxies as found to be the case by Capuzzo-Dolcetta & Tosta e Melo (2017).

The upper dotted lines in Figs 11 and 18 are obtained by adding all mass assembled in the nuclear region over the down-sizing time, i.e., it is $M_{\text{CMO}} = N_{\text{gen}} M_{\text{ecl,max}}$. This means that the nuclear clusters, in this mathematical description of the highly complex central processes, form one after another and on top of each other, the second one forming when the first one is finished after $\delta t = 10 \text{ Myr}$. This is not entirely unphysical as the notion is that star-formation proceeds also in the central nuclear region as long as the spheroid assembles over the down sizing time scale. These N_{gen} clusters therefore do not need to first spiral towards the central region through dynamical friction. The nuclear region is likely to grow further as non-nuclear massive clusters merge with the central region due to dynamical friction on the spheroid and due to gas drag (cf. Bekki 2010). The time-scale needed for a BH cluster with (for example) a mass $M_{\text{BH},0} = 10^8 M_{\odot}$ to sink to the center of its hosting spheroid due to dynamical friction on the stellar population can be estimated from the usual mass-segregation times scale,

$$t_{\text{ms}} \approx \left(\frac{m_{\text{star}}}{M_{\text{BH},0}} \right) t_{\text{sph,rlx}}, \quad (35)$$

where $m_{\text{star}} \approx 0.5 M_{\odot}$ is the mass of a typical star in the spheroid and $t_{\text{sph,rlx}} \approx (N/8 \ln(0.5N)) t_{\text{sph,cr}} \approx 6 \times 10^6 \text{ Gyr}$ is the median two-body relaxation time for the spheroid with radius of 2 kpc and containing $N \approx 10^{11}$ stars. The crossing time is $t_{\text{sph,cr}} \approx 12 \text{ Myr}$ and $t_{\text{ms}} \approx 30 \text{ Myr}$. Thus, over less than 0.1 Gyr most such clusters will arrive at the centre, adding to the SMBH masses in some cases. However, how and if such BH clusters do merge with the SMBH is a major open question and goes beyond the scope of this work. This discussion is merely meant to indicate the great complexity of the variety of processes that will be acting in the nuclear regions of spheroids and cannot be treated in any detail in the present contribution.

7 THE REDSHIFT-DEPENDENT NUMBER OF QUASARS

In this section the expected number of quasars at high redshift is assessed. Indeed, observations of the distribution of

quasars on the sky and with redshift are being applied to constrain structure formation (e.g. Song et al. 2016). From local observations it is known that most major galaxies host a SMBH and that the correlation between the SMBH mass and spheroid properties exists but that the overall situation is complex (Kormendy & Ho 2013). Taking the Local Group of galaxies (which has a zero-velocity radius of about 1.5 Mpc) as an example, there are two SMBHs in two major galaxies, the MW and M31, which leads to an equivalent of about 1.4×10^8 galaxies hosting SMBHs per Gpc^3 . The Catalogue of Nearby Galaxies (Karachentsev et al. 2004, 2013) contains about 1200 galaxies in total and 140 galaxies more massive than $10^9 M_{\odot}$ within a sphere with a radius of about 11 Mpc. This is equivalent to 2.5×10^7 such galaxies per Gpc^3 . Since it is to be expected that each of these galaxies hosted a SMBH in the early Universe, we would expect to observe of the order of $10^7 - 10^8$ quasars in a co-moving Gpc^3 volume at, e.g., a redshift of $z = 6$ if all these SMBHs were in fact accreting at the same time and would not be obscured by dust. Observational surveys of the number density of quasars at a high redshift are extremely difficult (e.g. Wu et al. 2011; Manti et al. 2017; Yang et al. 2018; Pacucci & Loeb 2019) and prone to major observational bias towards detecting only the brightest quasars and missing those that are obscured by intervening dust or missing quasars if they have an anisotropic emission. For example, Jiang et al. (2016) detect a few quasars per Gpc^3 at $z \approx 6$ with a decreasing number density with increasing redshift. There may thus be a problem in that, given the number of SMBHs per unit volume found in the local Universe, the expected number of quasars at a high redshift is not readily evident.

It is clear that neither are all SMBHs formed at the same time nor do they all accrete in-phase such that the visibility of quasars should be spread-out over time, possibly helping to alleviate the missing quasar problem. Within the framework of the present model (see Fig. 12), first the quasar-like hyper-massive clusters discussed above appear at very high redshift to then drop-out because they fade when the ionising stars die, for some of these to re-appear again after they formed SMBH seeds if these accrete gas sufficiently to shine as quasars. This accretion phase may last only while the spheroid forms, or later briefly again (of the order of a dynamical time, i.e. a hundred to a few hundred Myr) when the spheroid or hosting galaxy has an encounter with another galaxy such that gas enters its central region.

Using the model developed here we can estimate the observable number of quasars at a high redshift. This estimate also serves the purpose to visualise the redshift dependence of the two different phases which ought to exist: the first quasar-like hyper-massive star cluster phase and the subsequent accreting SMBH seed quasar phase.

In the following we estimate the number of quasars as a function of redshift using empirical constraints to serve as a visualisation of the model rather than to provide explicit quantification which depend on structure formation in an adopted cosmological model. The estimate is very basic and we do not aim at a fully fledged quantification as this would be beyond the scope of this contribution. The calculations neither take into account flux limits nor that some quasar-like objects or quasars may be unobservable due to obscuration by intervening dust or unfavourable viewing orientation if the quasars emit anisotropically.

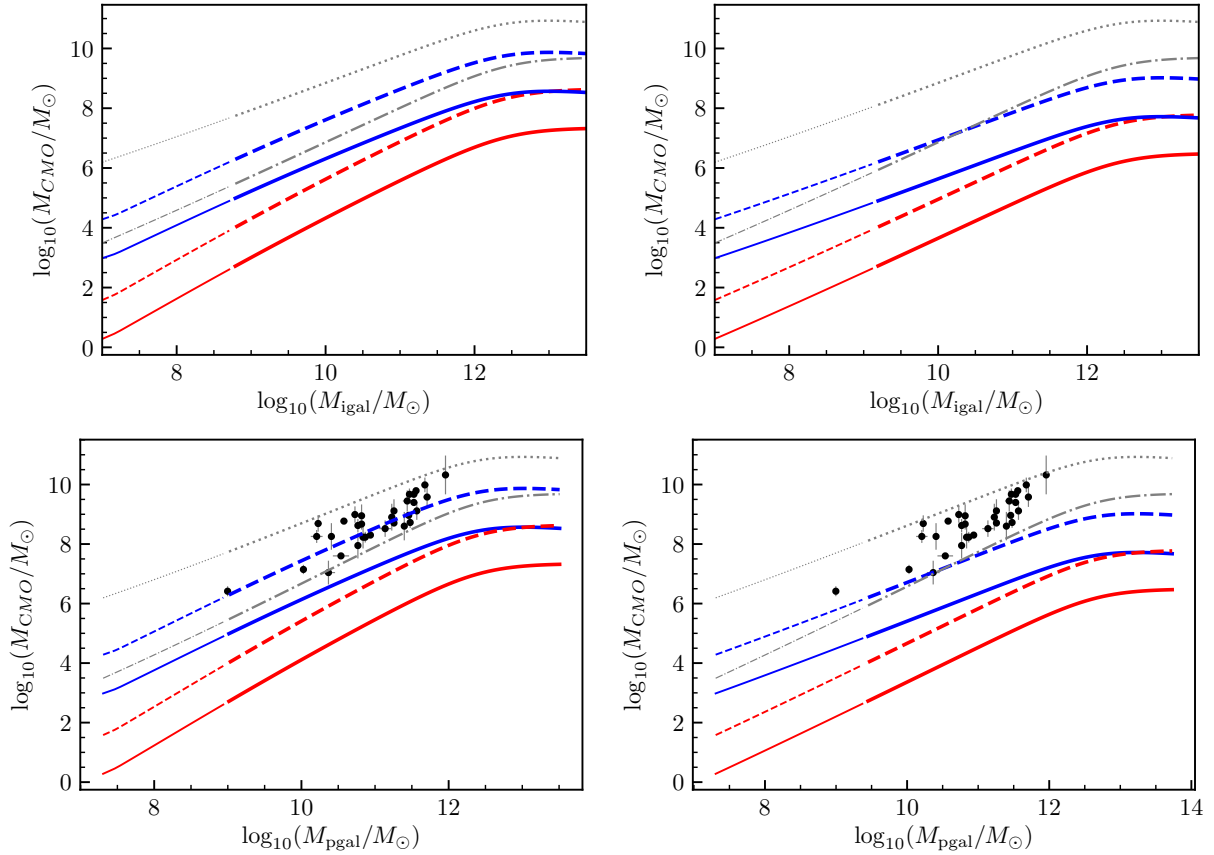


Figure 11. The mass of the central massive object, M_{CMO} , observed in a galaxy in dependence of the initial (total) stellar mass (upper panels) and the present-day luminous stellar mass (lower panels) of the hosting spheroid and assuming $\beta = 2.0$ (see Fig. 18 for the case $\beta = 2.4$). The left panels are for the variable IMF (Sec. 3.2) while the right panels are for the invariant canonical IMF (Sec. 3.1). The observational SMBH-mass data are the black dots with uncertainties (table 3 in McConnell & Ma 2013, see also Sanghvi et al. 2014; Heckman & Best 2014). Assuming that 5 per cent of the BH sub-cluster of mass $M_{\text{BH},0}$ in the first-formed cluster with a mass of $M_{\text{ecl,max}}$ merges to a SMBH-seed within 100–300 Myr (Fig. 8) yields the solid red line. The dashed red line assumes all of $M_{\text{BH},0}$ merges to the SMBH-seed. The solid blue line assumes that the SMBH-seed mass is $0.05 N_{\text{gen}} M_{\text{BH},0}$, i.e., that 5 per cent of all BH sub-clusters of all formed $M_{\text{ecl,max}}$ -clusters merge to one SMBH-seed. The blue dashed line assumes $N_{\text{gen}} M_{\text{BH},0}$ is the SMBH-seed mass, i.e. that all of the BH sub-clusters merge to an SMBH-seed due to gas infall onto the BH sub-clusters over the whole formation period (the downsizing time) of the spheroid. The divergence between the respective blue and red lines with decreasing M_{igal} is a result of downsizing (N_{gen} increasing for decreasing M_{igal}). The lower grey dash-dotted line depicts the SMBH-seed mass if all of $M_{\text{ecl,max}}$ collapses to the SMBH-seed. This scenario would only be valid if the gas-infall from the forming spheroid forces the whole cluster to coalesce to one massive object and is deemed to be merely an indicative possible upper mass limit. The case that all N_{gen} most massive consecutively-formed central clusters collapse in this way is shown as the upper grey dotted line. The gap and thinner lines for $M_{\text{igal,pgal}} < 10^9 M_{\odot}$ indicate the formal relationships but SMBH-seeds are unlikely to form for these spheroid masses as the BH clusters have $M_{\text{BH},0} < 10^4 M_{\odot}$ which cannot coalesce to any reasonably-massive SMBH-seed (Fig. 8).

Following Speagle et al. (2014) and Kroupa (2015) it is implicitly assumed here that galaxies follow a common, deterministic track. We assume the number of galaxies in a given co-moving volume remains constant with time. Is this a reasonable assumption? Conselice et al. (2016) calculates the number density of galaxies observed locally, given the number density at very high redshift, finding the local density to be smaller than expected by a factor of about 7 and inferring from this that galaxies merge and are destroyed in clusters. Their calculation does not take into account that the local 400-Mpc-radius volume is a significant underdensity (Karachentsev 2012; Keenan et al. 2013, by a factor of 3 to 5, fig. 1 in Kroupa 2015) such that the number of galaxies merging would be smaller. Concerning observational evidence for the role of mergers in galaxy formation and evolu-

tion, in “The Impossibly Early Galaxy Problem”, Steinhardt et al. (2016) note that there are several orders of magnitude more $10^{12-13} M_{\odot}$ dark matter halos at $z = 6 - 8$ than expected if hierarchical assembly through mergers were to be valid. Shankar et al. (2014) conclude, based on a sample of early-type galaxies, that the hierarchical merging models are disfavoured significantly and therefore that the dynamical friction time-scales need to be longer than theoretically expected. In the same vein, Kormendy et al. (2010) deduces that the large number of observed massive bulgeless galaxies are in contradiction to the hierarchical formation of such galaxies through mergers. The observational study by De Propriis et al. (2014) of merger rates using close pairs indicates blue galaxies to have a small merger incidence, being smaller than that expected in standard-cosmology. De

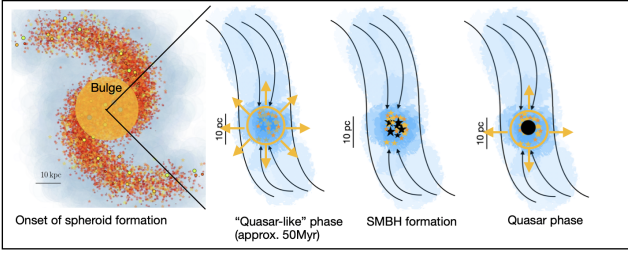


Figure 12. Visualisation of the major model ingredients (see Table 1): From left to right: formation of the spheroid, the formation of the central hyper-massive star cluster (the quasar-like object), the evolution of the BH cluster left by the hyper-massive cluster through accretion of gas from the still forming spheroid to the SMBH seed, accretion onto the SMBH seed of gas from the still forming spheroid (“true” quasar phase).

Propris et al. (2014) conclude that their findings minimize the importance of major mergers and interactions for galaxy evolution and they argue that most galaxy evolution takes place via secular and internal processes. Because disk (i.e. blue) galaxies dominate the number counts across a wide range of redshifts (Delgado-Serrano et al. 2010; Tamburri et al. 2014), we neglect merging in the present explorative simple estimate. As a caveat, the spheroids may form from early intense mergers (Sec. 2.1) and galaxies may be destroyed in galaxy clusters such that more work is needed to establish the role of such processes in galaxy evolution. The idea is thus to tag a galaxy whether it hosts a SMBH today and compute, from the observed present-day galaxy mass function, how many quasars we expect to see at a given redshift.

The life-time of the first quasar-like (hyper-massive star cluster) phase is ≈ 50 Myr. A stochastic interval is added during which gas re-accretes onto this cluster (now of BHs), and the quasar phase (i.e. the accreting SMBH-seed) lasts for the remaining time until the hosting spheroid has assembled.

7.1 The algorithm

By assuming the stellar mass density of the Universe, $\rho_{\text{stars}} = 0.0027 \times 1.46 \times 10^{11} M_{\odot}/\text{Mpc}^3$ (Karachentsev & Telikova 2018; Fukugita & Peebles 2004, see also Panter et al. 2004), the observationally constrained Schechter function (Conselice et al. 2016, their eq. 1 with parameters from the first row of their table 1) can be normalised such that the number density of galaxies in the local Universe is known. The normalisation leads to an equivalent $\eta_0 = 1.13 \times 10^9$ galaxies per Gpc^3 with a stellar mass between $10^6 M_{\odot}$ and $10^{13} M_{\odot}$, being in good agreement with the above number in view of the underdensity by a factor of about 3 to 5 in the local region with a radius of about 400 Mpc (Karachentsev 2012; Keenan et al. 2013).

The Schechter function is randomly sampled with $N_{\text{gal}} = 10^8$ galaxies, i.e. we obtain N_{gal} values of present-day masses, $M_{\text{pgal},i} \geq 10^6 M_{\odot}$. Using the Schechter function in this problem is not without precedent (e.g. Pacucci & Loeb 2019). Each galaxy is assumed to have a bulge/spheroid mass $M_{\text{sph},i} = X_1 M_{\text{pgal},i}/2$ (leaned on the results by Kormendy et al. 2010; $0 \leq X_1 \leq 1$ being a random deviate) and it is as-

sumed that stellar-evolution mass loss does not play a role in this exploratory modelling (Fig. 10 shows this to be a reasonable assumption). The requirement that a spheroid is needed for the quasar phase is based on the identification of their role for quasar activity (Kormendy et al. 2011) and is consistent with the model here in that the accretion onto the SMBH seed formed from the very early central cluster of BHs is fuelled by the formation of the spheroid.

The time of formation of a spheroid_i (i.e. the time or age of the Universe when the spheroid begins to form) with total stellar mass (once it has assembled all its stars), $M_{\text{igal},i}$, is (all times are in Gyr)

$$t_{\text{form},i} = \tau_{\text{Hubble}} - T_{1,i}, \quad (36)$$

with

$$T_{1,i} = T_{2,i} + 0.5 \Delta\tau_i, \quad (37)$$

where

$$T_{2,i} = a + b \log_{10} \frac{M_{\text{igal},i}}{M_{\odot}}, \quad (38)$$

with $a = 0.125 + X_2 (0.427 - 0.125)$ for random number deviate $0 \leq X_2 \leq 1$, $b = a c_1 + c_2$, $c_1 = (0.053 - 0.071)/(0.427 - 0.125)$ and $c_2 = 0.053 - c_1 0.427$, which together comprise a linear interpolation between the formation time in high- and low-density environments as given by eq. 3 in Thomas et al. (2005). The above formation time combines the average age of the stellar population (eq. 3 in Thomas et al. 2005) with the duration (i.e. down-sizing time scale) of the star formation in the spheroid (Eq. 1, Fig. 9) and $\tau_{\text{Hubble}} = 13.8$ Gyr is the age of the Universe (Planck Collaboration et al. 2018b). Thus, more massive spheroids form earlier and quicker, and the same occurs in low-density environments but delayed. It is thus assumed here that the galaxies form evenly distributed between high- and low-density regions. The relation between age (t) and redshift (z) is calculated for the standard LCDM model (Planck Collaboration et al. 2018a,b).

We conservatively assume every spheroid_i with a stellar mass $M_{\text{igal},i} > 10^{9.6} M_{\odot}$ (Fig. 11, Fig. 18) forms a hyper-massive cluster which appears quasar-like for 50 Myr. Following these 50 Myr, the time $t_{\text{infl},i}/\text{Myr} = 100 - 99 X_3$ is added during which the in-fall of gas into the BH cluster occurs. $0 \leq X_3 \leq 1$ being a random deviate and $t_{\text{infl},i}$ describes that gas in-fall may be very rapid (1 Myr) or delayed by a considerable amount (100 Myr being a conservative value, Sec. 8.2.1). The time, $t_{\text{compr},i}$, needed for the BH cluster to be squeezed to the SMBH seed by the gas in-fall, is then added before the quasar (i.e. the accreting-SMBH seed) phase begins. This time is expressed here as $t_{\text{compr},i}/\text{Myr} = 500 X_4$, with X_4 being another random deviate. This allows for the possibility that the coalescence of the BH cluster to a SMBH seed may be instantaneous or may take up to $t_{\text{rel},i} = 500$ Myr (Sec. 5, Fig. 8). Note that in this simple modelling we do not take into account the dependence of $t_{\text{rel},i}$ on $M_{\text{BH},0}$ evident in Fig. 8. The accretion phase of the now existing SMBH seed which formed in the cluster according to Sec. 5 is assumed to last for maximally the remaining downsizing time (Eq. 1), i.e., for the time

$$\Delta t_{\text{quasar},i} = \Delta\tau_i - (50 \text{ Myr} + t_{\text{infl},i} + t_{\text{compr},i}). \quad (39)$$

If $\Delta t_{\text{quasar},i} \leq 0$ Myr then no visible quasar phase is recorded.

time/Myr	physical process
$t = t_{\text{form},i}$	galaxy <i>i</i> begins to form
$t_{\text{form},i} \leq t \leq t_{\text{form},i} + 50 = t_{1,i}$	quasar-like hyper-massive cluster
$t_{1,i} < t \leq t_{1,i} + t_{\text{infl},i} = t_{2,i}$	infall of gas into BH cluster
$t_{2,i} < t \leq t_{2,i} + t_{\text{compr},i} = t_{3,i}$	BH cluster collapses to SMBH seed
$t_{3,i} < t \leq t_{\text{form},i} + \Delta\tau_1$	quasar phase only if $t_{3,i} \leq t_{\text{form},i} + \Delta\tau_1$
$t > t_{\text{form},i} + \Delta\tau_1$	SMBH in spheroid, possible AGN phase

Table 1. Sequence of time epochs. Subscript *i* refers to galaxy *i* in the calculation. The final phase constitutes the SMBH in the centre of the spheroid which can become an active galactic nucleus (AGN) if the spheroid accretes gas. The quasar phases are visualised in Fig. 12 (the physical relation between AGN, Seyferts and quasars is reviewed by Heckman & Best 2014).

Table 1 and Fig. 12 summarise these different evolutionary phases.

7.2 Results

The co-moving number density of quasar-like objects and of quasars per Gpc^3 is shown in Fig. 13 and 14.

Fig. 13 implies that the model based on the spheroid formation times of Thomas et al. (2005) leads to the too late appearance of quasars. Quasars are observed at $z > 5$ (e.g. Jiang et al. 2016, Sec. 7.3) in contrast to the present model which couples the onset of the formation of spheroids with the formation of hyper-massive clusters. One possibility would be to increase the downsizing time (Eq. 1). According to stellar population synthesis it would be about twice longer (de La Rosa et al. 2011; McDermaid et al. 2015). This approach however leads to the quasar phase lasting longer and thus to a larger number of quasars per unit time in the redshift range when the SMBH seeds are accreting from their forming spheroids.

Another possibility is to shift the spheroid formation times closer to the birth of the Universe and to increase the dispersion of these times, while keeping $\Delta\tau_1$ unchanged in order to not enlarge the quasar population. Fig. 14 indicates, in comparison to Fig. 13, how assumptions on the formation time of the spheroids affect the quasar counts. Thus, by moving the formation times 1.5 Gyr earlier to the birth of the Universe (and in addition introducing a 30 per cent spread of these formation times), quasars would be readily observed at the highest redshifts (Fig. 14). According to this model, at the very highest redshifts (i.e. at ages near 0.5 Gyr), the observed quasars are hyper-massive clusters (the quasar-like objects), and at later cosmological epochs (ages $\gtrsim 6$ Gyr) all quasars are accreting SMBHs. In the intermediate times both types of quasars co-exist albeit the hyper-massive cluster type contributes only about 10 per cent to the numbers. In this model, the quasar numbers per co-moving Gpc^3 reach a maximum around $z \approx 2$, with the brightest quasars appearing at $z > 9.5$. At these earliest cosmological ages ($t \lesssim 1.5$ Gyr), hyper-massive clusters slightly outnumber accreting SMBH seeds, with the very first “quasars” being, in this model, hyper-massive clusters. This model also implies that the number of quasars per co-moving Gpc^3 of both types decreases with increasing redshift $z > 3$. Especially the change of the number of the brightest quasars per co-moving Gpc^3 with increasing z for $z > 5$ (lower panel in Fig. 14) is

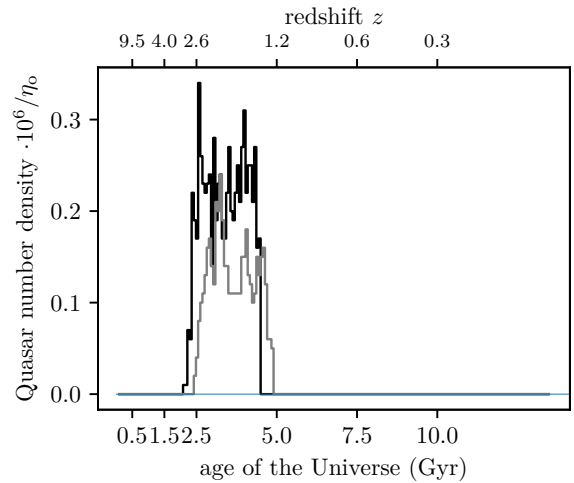
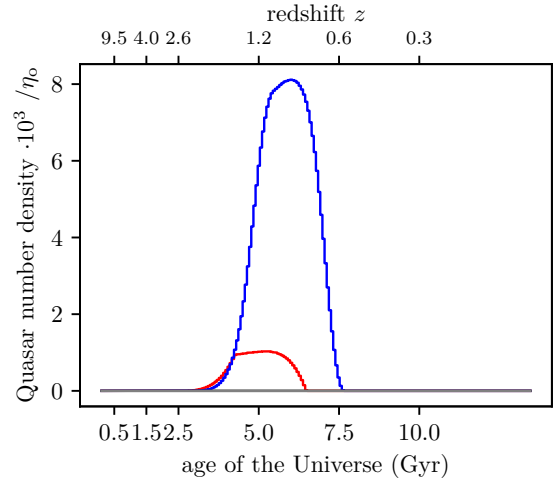


Figure 13. The number of quasars in a co-moving Gpc^3 volume in units of the present-day number of galaxies, η_0 , as a function of the age of the Universe. If quasars were to live for ever and their number would not change, then neither the quasar number density nor η_0 would change in this plot. Top panel: The red histogram is for all quasar-like hyper-massive clusters while the blue histogram shows all accreting SMBH seeds (i.e. “true” quasars) which form in these. Note that the quasar-like hyper-massive clusters appear before the accreting SMBH seeds, which however are the last ones to shine. At $t > 4$ Gyr the blue curve lies above the red one because the life-times are different, the accreting SMBH seeds being quasars for much longer and thus their numbers add-up in each time interval. The grey histograms below the blue and red ones are shown in the bottom panel. Bottom panel: only the quasars which are in the most massive spheroids with $M_{\text{gal},i} > 10^{11.5} M_{\odot}$. These are likely to have the largest accretion rates and are thus likely to be the brightest quasars. The black histogram is for the quasar-like hyper-massive clusters, while the grey histogram is for the accreting SMBH seeds. The hyper-massive clusters are more abundant in the present model because the accreting SMBH seed phase is limited by the short $\Delta\tau_1$ values of the massive spheroids. Thus, many hyper-massive clusters leave SMBH seeds, which however do not appear as quasars ($\Delta t_{\text{quasar},i} \leq 0$, Eq. 39) or do so only for a short time. For example, in the upper panel at an age $t \approx 5$ Gyr, the model implies there to be about 8×10^6 accreting SMBH seeds per co-moving Gpc^3 which should appear like quasars (blue curve). In the lower panel, at $z \approx 2.6$, there would be ≈ 300 quasar-like hyper-massive clusters per co-moving Gpc^3 (black histogram) while there would be about 100 accreting SMBH seeds (“true” quasars) per co-moving Gpc^3 (grey histogram). Note that the quasars in the most massive spheroids (lower panel) appear before the vast number of quasars in all spheroids (upper panel), and that, with the formation times assumed here (Eq. 38), no quasars ought to be observable at $z > 3$. At lower redshifts, AGN and quasars are most likely triggered

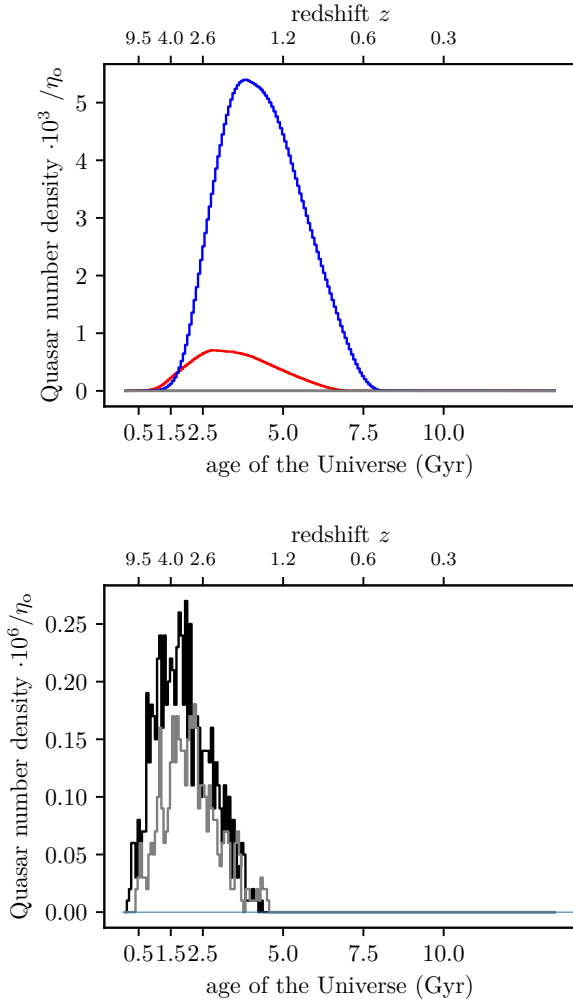


Figure 14. As Fig. 13, but here it is assumed that the spheroid formation time, $T_{2,i}$ (Eq. 38), is reduced such that all galaxies form 1.5 Gyr earlier, and that this new time $T_{2,i}$ is randomised with a uniform distribution over the interval ± 30 per cent (leaving $\Delta\tau_i$ unchanged). This adds a reasonable degree of variation in the formation time without affecting the down-sizing time scale, since it is expected that spheroids which end up with the same stellar mass would not all form at exactly the same time even if forming in the same density environment since perturbations are likely to play a role (values of $t_{\text{form},i} \leq 0.1$ Gyr are transformed to a random value in the range $0.1 \leq t_{\text{form},i}/\text{Gyr} < 1$, but this affects only a negligible number of cases). According to this model, there ought to be a peak of $\approx 5.5 \times 10^6$ quasars per co-moving Gpc^3 at $z \approx 2$ (blue curve in the upper panel), while the hyper-massive clusters would contribute about 10 per cent to the number as quasar-like objects (red curve in the upper panel). At a redshift of about $z = 5$ there would be about 100 quasars and about 200 quasar-like hyper-massive clusters per co-moving Gpc^3 (grey and black histograms, respectively, lower panel).

reminiscent of the observed dependency (Jiang et al. 2016). This is demonstrated in Fig. 15.

The following two problems thus emerge within the present model and would need to be addressed in future studies:

- The very early formation times that are suggested by

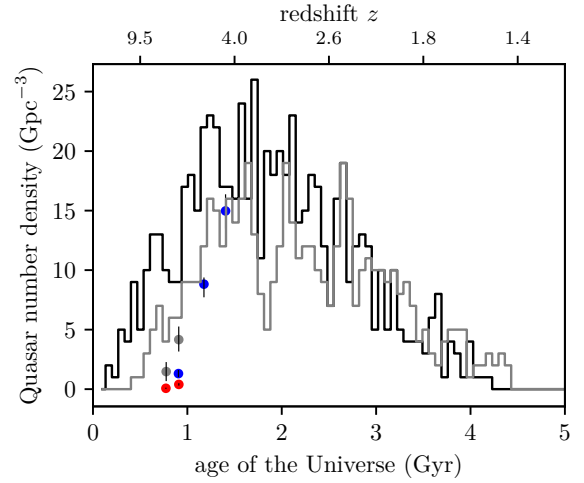


Figure 15. As Fig. 14, lower panel, but here showing the expected number of quasars per co-moving Gpc^3 (rather than the normalised value) and assuming only 10 per cent of all quasar-like hyper-massive clusters and 10 per cent of all quasars can be detected because of dust obscuration and unfavourable viewing directions. These model numbers are compared with the numbers per co-moving Gpc^3 gleaned from a survey of $z \approx 6$ quasars (Jiang et al. 2016) shown by the seven symbols. The reader is referred to their fig. 10 for a detailed description of the symbol types. Notable is also that a newer and more sensitive survey reports about 380 quasars per co-moving Gpc^3 at $z \approx 5$ (Shin et al. 2020, their table 4), which is comparable to the model numbers shown in the bottom panel of Fig. 14.

the observed very-high red-shift quasars appear to be in tension with the formation times deduced from the observational analysis of spheroids by Thomas et al. (2005) which would not allow quasars to exist at $z > 5$. More generally, the nearby massive-spheroid data and the high redshift observations in terms of the SFRs and timings (Sec. 8.2.3) appear to be in conflict.⁴

- Another issue raised here is that of the “missing quasars”: As noted above, the number of SMBHs in the local Universe should lead to $10^6 - 10^7$ quasars per co-moving Gpc^3 existing at intermediate redshifts ($1 \lesssim z \lesssim 3$, Fig. 14 for the more realistic spheroid formation times). Such an expected large number is difficult to verify observationally. For example, the spectroscopic survey by Eftekharzadeh et al. (2015) reports about 3000 quasars per co-moving Gpc^3 in the redshift range 2.2 – 2.8, while 3–4 million are expected (blue curve in Fig. 14). Eftekharzadeh et al. (2015) discuss the daunting observational problems in this work, and a combination of missing quasars due to dust obscuration and unfavourable viewing direction as well as flux limits may bring the model numbers into the observed range. But the very early cosmological era during which quasars are expected to appear may lead to countable predictions. The number of brightest quasars per co-moving Gpc^3 , expected to be hosted in the most massive forming spheroids ($M_{\text{gal},i} > 10^{11.5} M_{\odot}$),

⁴ One issue relevant for this problems is the redshift-age relation which may differ in different cosmologies (e.g. Melia 2009; Balakrishna Subramani et al. 2019; Merritt 2017).

is indeed much smaller as the model calculations depicted in the lower panel of Fig. 14 (about 300 quasars in total at $z \approx 5$) indicate. The model presented here thus underlines this issue of missing quasars at intermediate redshifts, despite taking into account that the quasars would not form at the same time but in dependence of the formation time of their hosting galaxy and that they would come in two phases with interruption in detectability. Detecting quasars at a high redshift is very difficult so it is not clear yet whether a missing-quasar problem exists. Indeed, assuming only 10 per cent of the existing quasar-like objects and quasars can be detected leads to model numbers in agreement with those observed (Fig. 15).

The model as shown in Figs 14 and 15 thus lead to about ten times more quasars being expected than are observed at $z > 5$. If the large number density of quasars expected as based on the Local Cosmological Volume galaxy numbers and the model studied here are not found at a high redshift, then this would imply that the SMBHs hosted by the majority of galaxies with stellar mass $\gtrsim 10^{9.6} M_\odot$ would need to be either existing at a high redshift but not be accreting (thus supporting a primordial origin), or that they might need to form later but largely invisibly. Both possibilities appear to pose difficult physical hurdles.

7.3 A case in point: the $1.5 \times 10^9 M_\odot$ SMBH in the luminous quasar Pōniuā’ena at $z = 7.5$

How does this model fare in comparison with the discovery by Yang et al. (2020) of the $z = 7.5$ ($t \approx 700$ Myr after birth of the Universe) quasar J1007+2115 which is interpreted to be powered by an $\approx 1.5 \times 10^9 M_\odot$ heavy SMBH? The quasar is observed to be in a host with $80 \lesssim SFR_{\text{[CII]}}/(M_\odot/\text{yr}) \lesssim 520$ (based on the [CII] emission line) and $SFR_{\text{TIR}} \approx 700 M_\odot/\text{yr}$ (based on total infrared luminosity assuming $T_{\text{dust}} = 47$ K). Assuming the IMF is top-heavy and that the correction factor is $\kappa = 0.5$ (Eq. 50 below), $40 \lesssim SFR_{\text{true}}/(M_\odot/\text{yr}) \lesssim 350$.

According to the model this quasar may be interpreted non-exclusively as follows:

(i) It may be a hyper-massive star-burst cluster formed at $z = 7.5$ (within about 10 Myr of the observation). It may, for example, constitute the first cluster with $M_{\text{ecl,max}} \approx 3 \times 10^9 M_\odot$ formed at the start of assembly of the spheroid which will become an elliptical galaxy with a mass of about $10^{12} M_\odot$ which follows from the $M_{\text{ecl,max}}(SFR)$ relation (Eq. 5) and assuming the standard downsizing time $\Delta\tau = 0.34$ Gyr (Eq. 1). The bolometric luminosity of this cluster (assuming it has a top-heavy IMF, Eq. 7) would be $L_{\text{bol}} \approx 3 \times 10^{13} L_{\text{bol},\odot}$ (fig. 3 in Jerabkova et al. 2017) which compares favourably with the observed value. The cluster would drive a massive outflow which may have the observed line widths (Sec. 3.4). The SFR would correspond to $SFR_{\text{true}} \approx 300 M_\odot/\text{yr}$ for a formation time-scale of 10 Myr assuming only this cluster is forming.

(ii) Alternatively, it may already be an accreting SMBH which formed as a SMBH-seed from such a cluster. In this case, the SMBH-seed might comprise the conservative 5 per cent of $M_{\text{BH},0}$, amounting to $\approx 4.8 \times 10^7 M_\odot$ (Fig. 2) and it would need to accrete at the Eddington-limited constant super-Eddington rate for about 172 Myr (Eq. 34) to reach $1.5 \times 10^9 M_\odot$. This interpretation would necessitate the host-

ing cluster with $M_{\text{ecl,max}} \approx 3 \times 10^9 M_\odot$ to have formed sufficiently prior to the age it is observed at (≈ 700 Myr) to allow (a) all massive stars to transform into BHs (about 50 Myr), (b) to allow gas-inflow from the forming spheroid to shrink the sub-cluster of BHs to the SMBH-seed ($\approx 100 - 200$ Myr, Fig. 8) and (c) to allow the SMBH-seed to grow to the deduced $1.5 \times 10^9 M_\odot$ (≈ 172 Myr). The onset of the formation of the spheroid would thus have to have been at an age of $280 \lesssim t_{\text{form}}/\text{Myr} \lesssim 380$ Myr after the birth of the Universe (cf. Fig. 15 and 16). The SFR_{true} value at the moment this object is observed at would correspond to a snapshot of the SFH of the forming spheroid (nominally at $3000 M_\odot/\text{yr}$ according to the box SFH model in Fig. 16) and may be suppressed momentarily through the action of the quasar (cf. Ploeckinger et al. 2019).

These possibilities are non-exclusive because different combinations between $M_{\text{ecl,max}}$, t_{form} and time for the SMBH-seed to reach $1.5 \times 10^9 M_\odot$ (as long as it is $\lesssim \Delta\tau$) are possible in this model.

The discovery of Pōniuā’ena thus appears to be consistent with the present model but clearly much more work will be needed to test the above possibilities. For example, concerning the first hypothesis above, it needs to be checked if a hyper-massive cluster can drive an outflow which does resemble the observations. It will also be important to check if the $\lesssim 100$ kpc (Sec. 2.1) surroundings of this putative first hyper-massive cluster contains a gas cloud weighing a few times $10^{12} M_\odot$ from which the spheroid will form. Concerning the second hypothesis, observations might verify if a major galaxy is in the process of assembling around the quasar. Because about 333 – 433 Myr have passed since the putative $M_{\text{ecl,max}} \approx 4 \times 10^9 M_\odot$ hyper-massive starburst cluster began to form (at $t_{\text{form}} \approx 280$ to 380 Myr), the spheroid, which nominally takes $\Delta\tau = 0.34$ Gyr to form, should already largely be present with a possibly already decreasing SFH.

8 DISCUSSION

The above calculations are simplified because the physically realistic situation of an astrophysically and stellar-dynamically evolving super-star cluster formed at extremely low metallicity and at the centre of a violently forming and evolving spheroid including gas in- and out-flows and stellar mergers cannot, for the time being, be computationally assessed in full rigour. In the study of this problem performed here, the well-documented empirical constraints on freshly formed stellar populations (which are the basic axioms of the IGIMF theory, Sec. 3.3) and the global evolution of a cluster of BHs, which emerges from the stellar population, are combined.

The evolution of the BH sub-cluster is primarily dictated by balanced evolution and by gas drag, as discussed above. The physically realistic situation is however very complex as the BHs accrete, they exert radiation which heats the gas and also the rate of cooling of the gas in the BH sub-cluster is governed by the opacity. In Sec. 8.1 some of these processes are briefly touched upon in view of their possible influence on the overall evolution of the BH sub-cluster and may be helpful in future extensions of this work. In particular the possibility that accreting BHs may be accelerated

rather than suffer orbital decay is raised. The mutually related problems of whether spheroids form as rapidly as in this model and if the observed SFRs at a high redshift are as high as associated with the formation of spheroids in the present model are addressed in Sec. 8.2. In Sec. 8.3 additional caveats are attended to.

8.1 Gas accretion onto the BHs

As the BHs orbit through the in-falling gas they accrete from it (for a comprehensive treatment see Frank et al. 2002). The Bondi-Hoyle-Lyttelton accretion rate onto a BH of mass m_{BH} moving with velocity $v \approx \sigma$ through an ambient medium of (mass) density ρ_{g} and sound speed c_{s} is

$$\dot{m}_{\text{BH}} = 4\pi\rho_{\text{g}} \frac{G^2 m_{\text{BH}}^2}{(v^2 + c_{\text{s}}^2)^{3/2}}. \quad (40)$$

Assuming supersonic motion which is appropriate for the case of extremely dense star clusters, $v \gg c_{\text{s}}$,

$$\dot{m}_{\text{BH}} = 4\pi\rho_{\text{g}} \frac{G^2 m_{\text{BH}}^2}{v^3}. \quad (41)$$

The accretion onto the moving BH leads to loss of momentum, $\dot{p} \approx -\dot{m}_{\text{BH}}v$, leading to dissipation of kinetic energy, $\dot{E}_{\text{BH}} \approx v\dot{p}$, which implies an equation for the shrinkage of the BH sub-cluster similar to Eq. 28 since both effects (dynamical friction and accretion) are due to the same physical process.

With accretion-induced feedback, the accretion rate is proportional to mass (as opposed to Eq. 40) because the feedback luminosity, which opposes infall, is proportional to the mass of the BH. Eddington-limited BH growth, a limit where the in-falling matter radiates its rest-mass energy which balances the infall, is thus significantly slower than growth through Bondi-Hoyle accretion, which is why taking $m_{\text{BH}} = \text{constant}$ (Sec. 5) is a reasonable assumption.

Thus, if we assume that the accretion rate is at the Eddington limit, then

$$\dot{m}_{\text{BH}} = m_{\text{BH}}/\tau_{\text{Edd}}, \quad (42)$$

with

$$\tau_{\text{Edd}} \equiv \frac{c\sigma_{\text{T}}}{4\pi G m_{\text{p}}} \approx 452 \text{ Myr}, \quad (43)$$

where c is the speed of light, σ_{T} is the Thompson scattering cross section and m_{p} is the mass of the proton. In this case the BHs double their mass every ≈ 300 Myr.

To give an explicit example, assume that the BHs accrete at a constant fraction of the Eddington limit, i.e.,

$$\dot{m}_{\text{BH}} = f_{\text{Edd}} m_{\text{BH}}/\tau_{\text{Edd}} \quad (44)$$

with $f_{\text{Edd}} = (1 - \epsilon_{\text{r}})/\epsilon_{\text{r}} < 1$, the radiative efficiency ϵ_{r} being the fraction of the rest-mass energy of the in-falling matter being electromagnetically radiated. Thus, for Eddington-limited accretion at the Eddington rate, $\epsilon_{\text{r}} = 0.5$, while a standard assumption used throughout the literature is accretion to occur Eddington-limited but with a super-Eddington rate with $\epsilon_{\text{r}} = 0.1$ (Salpeter 1964; Yoo & Miralda-Escudé 2004; Basu & Das 2019). This means that the mass-growth of the black hole is regulated by the feedback from the accretion flow, while the mass accretion onto the black hole is at the

super-Eddington rate as given by the customary assumption $\epsilon_{\text{r}} = 0.1$. The mass of a BH then grows with accretion time $t_{\text{accr}} = t - t_{\text{start}}$ as

$$m_{\text{BH}}(t) = m_{\text{BH},0} \exp\left(\frac{f_{\text{Edd}} t_{\text{accr}}}{\tau_{\text{Edd}}}\right), \quad (45)$$

where $m_{\text{BH},0}$ is the initial mass of the BH at time t_{start} . Over the formation time-scale of the spheroid (up to a few hundred Myr, Eq. 1), the mass growth of the BH is relatively small and can thus be neglected without significantly affecting the results on the shrinkage of the BH cluster.

The realistic situation is complicated because the dormant BH begins to accrete according to Eq. 40. The accreted gas forms an accretion disk about the BH feeding the BH and thus increasing m_{BH} in a regulated manner and more likely similar to a rate given by Eq. 45. The interplay between the accretion onto the disk and the accretion onto the BH defines the mass growth of the BH plus accretion disk system, the outflow in the form of relativistic jets and the actual mass gain of the BH.

Assume that the BHs moving through the gaseous medium will accrete at the Eddington-limited rate, i.e., with the accretion rate given by Eq. 44. Assuming further that half of the rest mass energy of the accreted matter turns into radiation⁵, $\epsilon_{\text{r}} = 0.5$, the luminosity of individual BHs will be $L_{\text{BH},\text{acc}} \approx \frac{1}{2} \dot{m}_{\text{BH}} c^2$. The total accretion luminosity of the cluster of BHs is thus

$$L_{\text{acc}} \approx \frac{1}{2} N \dot{m}_{\text{BH}} c^2. \quad (46)$$

If L_{acc} exceeds the formal Eddington luminosity, L_{Edd} , of the whole cluster of mass $M_{\text{cl}} = N m_{\text{BH}} + M_{\text{g}}$, the gas cloud would be blown out and its density will drop. Consequently, both energy dissipation of the BH sub-cluster and its luminosity will be decreased or even stopped, until the gas inflow re-establishes. The ratio of L_{acc} and L_{Edd} is estimated next. Assuming the gas consists of ionised hydrogen,

$$L_{\text{Edd}} = \frac{4\pi G m_{\text{p}} c M_{\text{cl}}}{\sigma_{\text{T}}}, \quad (47)$$

i.e

$$\frac{L_{\text{Edd}}}{L_{\odot}} = 3.4 \times 10^5 \frac{M_{\text{Edd}}}{M_{\odot}}, \quad (48)$$

where $M_{\text{Edd}} = M_{\text{cl}}$ is the luminosity-inferred Eddington mass of this accreting object with, in this case, a mass of M_{cl} .

When $L_{\text{acc}}/L_{\text{Edd}} > 1$, ρ_{g} would decrease within R on a time-scale that may be estimated by 10^4 K gas leaving the cluster radius R with the sound speed (about 10 km/s), thus on a time-scale of $\tau_{\text{out}} \approx R/(10 \text{ km/s})$. If this blow-out time-scale is much longer than the crossing time of BHs through the cluster, $\tau_{\text{out}} \gg t_{\text{cross}}$, then the BH sub-cluster would expand to a new $R_{\text{new}} = R/(1 - f_{\text{out}})$ (eq. 25 in Kroupa 2008), where $f_{\text{out}} = M_{\text{g}}/N m_{\text{BH}}$ is the fraction of mass blown out, assuming all gas goes and ignoring the rest of the stellar cluster in which the BH sub-cluster is embedded. It is un-

⁵ While this assumption is a reasonable first order estimate for standard disc-like accretion flows, a completely different geometry of the accretion flow considered here may lead to a different relation between the accretion rate and luminosity. The estimate used here, however, represents a rather safe upper limit.

clear though if this evolution is viable, because the in-falling gas from beyond R as a result of the continued formation of the spheroid during the first few hundred Myr is likely to limit the decrease of ρ_g within R . Consequently, we ignore the possible drop of ρ_g during the assembly of the spheroid.

Given the long mass-doubling time and the likely interruptions of the accretion activity, the conservative case is $\dot{m}_{\text{BH}} = 0$ which is why this work assumes $M_{\text{BH}}(t) = \text{constant} = M_{\text{BH},0}$. In this case the shrinkage time of R calculated in Sec. 5 is likely to overestimate the time-scale to SMBH-seed formation. The special case, $\dot{m}_{\text{BH}} = 0, \dot{M}_g \propto M_g^2$, leads to an analytical solution to the mass increase of the gas mass within R (see Appendix 1).

One important caveat which will need to be taken into account in future modelling is the possibility that the gas accretion onto the BH sub-cluster will lead to the individual BHs in the sub-cluster to accelerate. Kim & Kim (2009), Gruzinov et al. (2020) and Li et al. (2020) point out that accreting BHs which move through a gaseous medium and which drive an outflow may experience, under certain conditions, acceleration rather than a deceleration. The details are highly complex, especially in view of the calculations that were performed being by necessity simplified and idealised. The BH sub-cluster envisioned in the present model experiences gas in-fall from the forming spheroid at a high rate which is most likely time variable and also highly inhomogeneous. Since the BHs accrete some of this gas, their growing mass and accretion of gas with, on average, a negligible momentum, should be shrinking the BH sub-cluster. The dissipational gas component further shrinks the sub-cluster as its mass increases through accretion.

8.2 On the formation of massive spheroids

The model of SMBH formation relies on the most-massive-star-cluster (Eq. 2 or 5) and the formation-time-scale (Eq. 1) to correlate with the mass of the spheroid. These relations imply large SFRs and short assembly times. Are these consistent with other evidence gleaned from high-redshift observations and modelling of spheroids? This question is relevant for understanding the SMBH–spheroid mass correlation. Observational information on the formation of spheroids is touched upon in Sec. 8.2.1 and Sec. 8.2.2 contains a discussion of observational constraints on SFRs at high redshift. In Sec. 8.2.3 the possible revision of these SFRs is considered if the high-redshift dust temperatures are lower than assumed and if the galaxy-wide IMF is top-heavy in spheroid formation. The implications of this on the SMBH-seed are discussed in Sec. 8.2.4.

8.2.1 Observational constraints on the formation of spheroids

This model rests on the bulk of a spheroid assembling rapidly such that the centre-most very massive star cluster correlates with the rest of the mass of the spheroid through the observed SFR–most-massive-young cluster relation. This also yields the observed metal and alpha-element abundances of spheroids. If it were to be found that spheroids form from previously uncorrelated smaller proto-galaxies, then this would largely invalidate the model.

Concerning evidence on the assembly of spheroids obtained independently of elemental abundances: A massive, nearly non-star-forming galaxy with a velocity dispersion of about 270 km/s has been found to be present at a redshift $z = 4.01$ (Tanaka et al. 2019)⁶. Glazebrook et al. (2017) report the discovery of a quiescent galaxy with stellar mass $\approx 1.7 \times 10^{11} M_\odot$ at $z = 3.17$. Concerning more-local spheroids, in their spatially-resolved stellar populations analysis of a sample of 45 elliptical galaxies, Martín-Navarro et al. (2018) find that the bulk of stars are old and typically formed $\gtrsim 10$ Gyr ago. Salvador-Rusiñol et al. (2020) conclude, based on their study of 28663 galaxies, residual star formation to be ubiquitous in massive early-type galaxies, amounting to an average mass fraction of 0.5 % in young stars in the last 2 Gyr of their evolution. They also conclude that this fraction decreases with increasing galaxy stellar mass, being consistent with downsizing. Lim et al. (2020) discovered the sustained formation of globular clusters around the central giant elliptical galaxy of the Perseus cluster in large-scale filamentary structures. The analysis by Vazdekis et al. (2016) of a representative set of spheroids of varying mass implies a small fraction of the stellar body to be young with the bulk being very old. Seidel et al. (2015) find, that in all the galactic bulges they studied, at least 50 per cent of the stellar mass already existed 12 Gyr ago, being more than currently predicted by simulations. These results are consistent with the finding by Delgado-Serrano et al. (2010) that the fraction of early-type galaxies amongst galaxies with a baryonic mass $> 1.5 \times 10^{10} M_\odot$ remains constant at 3–4 per cent over the past 6 Gyr, a similar result being reported by Tamburri et al. (2014) but for $0.6 \leq z \leq 2.5$. This is consistent with the conclusion reached by Lorenzo et al. (2014), as based on their survey of isolated galaxies, that the colours of the red bulges and the low bulge-to-total ratios for AMIGA isolated galaxies are consistent with an early formation epoch and not much subsequent growth. The major observational survey and stellar population synthesis by de La Rosa et al. (2011) and McDermid et al. (2015) finds massive early type galaxies to have formed their stars faster and earlier than less-massive ones. McDermid et al. (2015) write that all of today’s spheroids share an early period of intense star formation, making the systems compact, metal-rich, and alpha-enhanced. It should be noted though that their downsizing times are systematically longer by about a factor of two than those quantified by Eq. 1.

Intimately linked to the formation process of spheroids are their morphological properties – while star formation observations indicate that the bulk of the massive spheroids formed very early (perhaps monolithically), the evidence from modelling of morphological and kinematical properties of spheroids is not so clear: Massive elliptical galaxies show cores, are boxy and slow rotators, while less massive ones are disk, have power-law slopes and are fast rotators (e.g. Bender et al. 1989, 1992). Krajnović et al. (2020) provide a detailed discussion of the rich morphology and kinematical complexity of spheroids. These properties need to be accounted for in any formation theory. The properties range from being explainable via massive dissipation-less mergers and via gas accretion and gas-rich mergers (Naab et al.

⁶ The redshift–age correspondence can be found e.g. in Fig. 16

2014). Trakhtenbrot et al. (2018) acknowledge that many of their high redshift sources hosting quasars may be interpreted to be merging galaxies, and point out that in some cases the ordered gas rotation signatures do not support this, implying other than merging processes to be feeding the star-formation activity. Early-type galaxies show a significant size evolution with redshift from $z \approx 2$ to $z = 0$ (Balakrishna Subramani et al. 2019 and references therein). Using Nbody simulations of minor and major dry mergers, Nipoti et al. (2009) conclude that the observed magnitude of the size evolution cannot be explained through dissipation-less mergers. By using a high-resolution cosmological simulation, Naab et al. (2009) deduce, on the other hand, that compact high-redshift spheroids can evolve into the observed sizes and concentration of present-day spheroids by undergoing minor mergers such that minor mergers may be the main driver for the late evolution of sizes and densities of the observed spheroids. A review of the current standing of the merger theory can be found in Naab & Ostriker (2017). Dissipation-less (dry) monolithic formation models of galaxies explored by Nipoti et al. (2007) in Milgromian gravitation (Milgrom 1983; Bekenstein & Milgrom 1984; Famaey & McGaugh 2012; Merritt 2020) are an alternative approach. The challenge facing all models is to explain the combination of high metallicity and high alpha-element abundances (Sec. 2.1).

In summary, the evidence thus seems to suggest that the bulk (at least about 50 per cent) of the present-day spheroids did form early and rapidly and possibly monolithically, but that a part of the stellar body may have joined later. If the time-scale of the formation of the bulk of the spheroids is longer by a factor of two than the downsizing time deduced from metallicity constraints, as suggested by the stellar-population synthesis work, then the implied SFRs would be correspondingly lower (by a factor of 2) than used in the nominal modelling here which assumes all the mass of the spheroid to form in the time $\Delta\tau$ (Eq. 1), leaving more time for hierarchical merging to play a role.

8.2.2 Observed SFRs

First the SFH of a typical model is discussed to then consider how observed SFRs at high redshifts compare.

The model presented here assumes an idealised box-shaped SFH (Fig. 16). A more detailed description of monolithic formation would include star formation starting in the highest-density peak very low-metallicity gas near the centre of the future spheroid to then pick-up as the gas collapses and forms the spheroid. Such a putative SFH is approximated in Fig. 16 as a skew normal distribution. In standard cosmology, the accretion of gas onto a galaxy can be parametrised as (Dekel et al. 2009)

$$\frac{SFR}{M_{\odot}/\text{yr}} \approx 6.6 \left(\frac{M_{\text{DMH}}}{10^{12} M_{\odot}} \right)^{1.15} (1+z)^{2.25} f_{0.165}, \quad (49)$$

where $f_{0.165}$ is the baryon fraction in the dark matter halos in units of the cosmological value, $f_b = 0.165$, and M_{DMH} is the mass of the dark matter halo. It is assumed here, for the purpose of the argument, that a dark matter halo with $M_{\text{DMH}} = 6 \times 10^{12} M_{\odot}$ (such that $M_{\text{igal}} = 10^{12} M_{\odot}$ for consistency with $f_{0.165} = 1$, Dekel et al. 2009) formed at very high

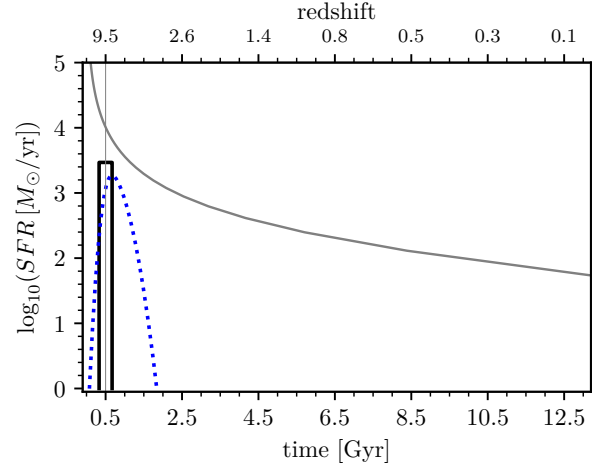


Figure 16. The idealised box-shaped SFH adopted in this model is shown as the black solid line. It assumes the SFR jumps to $SFR = 3 \times 10^3 M_{\odot}/\text{yr}$ implied by Eq. 1 for the downsizing time $\Delta\tau = 0.34 \text{ Gyr}$. The midpoint of the SFH lies at 0.5 Gyr corresponding to $t_{\text{form}} = 0.33 \text{ Gyr}$ (cf Fig. 14). A more realistic SFH can be approximated by a skew normal distribution as shown by the dotted blue line. This example has the skew parameter set to 2.5 (0 corresponding to a Gaussian), the sigma value is $\Delta\tau$ and the location is 0.5 Gyr. The gray solid line corresponds to the growth rate of the baryonic component of a galaxy in the standard dark-matter-based cosmological model (Eq. 49). Except for the latter, in the two SFH models the integral under each curve yields the mass formed in stars, $M_{\text{igal}} = 10^{12} M_{\odot}$. In both models, the first hyper-massive star-burst cluster at the centre of the spheroid with a mass of $M_{\text{ecl,max}} = 3 \times 10^9 M_{\odot}$ (Eq. 5) would form during the first few Myr. Note that the box and skew-normal models do not emerge from a self-consistent cosmological structure formation calculation such that the here applied value of t_{form} is not a prediction but an assumption.

redshift and accretes gas such that the accretion rate equals the SFR. The resulting SFH is shown in Fig. 16. Given the stellar population synthesis constraints from recent observations, the galaxy would need to shut-off star-formation after a few 100 Myr.

Thus, star-formation begins in the highest-density gas which also cools fastest. If the formation of stars at very low metallicity and in the first highest-density peaks occurs mostly in extremely massive star-burst clusters, i.e. if the initial mass function of embedded clusters, $\xi_{\text{ecl}}(M_{\text{ecl}})$, is strongly top-heavy ($\beta \leq 2$ in Eq. 4) under these conditions, a hyper-massive star-burst cluster weighing $10^8 \lesssim M_{\text{ecl}}/M_{\odot} \lesssim 10^9$ would need $20 \lesssim SFR_{\text{true}}/(M_{\odot}/\text{yr}) \lesssim 1000$ to form over a time of 1–5 Myr. Metal-enrichment proceeds on the time-scale of a few dozen Myr and will be especially rapid if the IMF in this cluster is top-heavy (Murray 2009), such that observing a metal-enriched high redshift star-burst is not necessarily in contradiction with it beginning to form from very low-metallicity gas.

In terms of observed SFRs at high redshifts, Finkelstein et al. (2013) find a galaxy at a redshift of $z \approx 7.5$ (about 700 Myr after the Big Bang assuming the detected emission line to be Ly α ; the alternative redshift being $z = 1.78$ if the line is [O II]) with a 68 per cent confidence range $320 < SFR_{\text{obs}}/(M_{\odot}/\text{yr}) < 1040$ and a stellar mass $0.9 \times 10^9 - 1.2 \times 10^9 M_{\odot}$. Trakhtenbrot (2020) pro-

vides a review of the properties of high redshift quasars and ALMA observations of their hosts show observed SFRs surpassing $1000 M_{\odot}/\text{yr}$ at $z > 6$ in some cases. Nguyen et al. (2020) depict, in their fig. 9 and for the twelve quasars at $z \approx 4.8$ observed with ALMA, host-galaxies. These have $1000 \lesssim SFR_{\text{obs}}/(M_{\odot} \text{Myr}^{-1}) < 4000$. Nguyen et al. (2020) assume a dust temperature, $T_{\text{dust}} = 60 - 70 \text{ K}$, for the objects with the highest SFRs in their sample. Trakhtenbrot et al. (2018) point out, as an interesting case in point, that the system J1341 ($z \approx 4.8$) has an observationally deduced $SFR_{\text{obs}} \approx 3000 M_{\odot}/\text{yr}$ ($T_{\text{dust}} = 47 \text{ K}$) and evidence of rotation-dominated gas and no companion galaxies, being quite comparable to the galaxy-formation simulations by Wittenburg et al. (2020). Forrest et al. (2020) report a $z = 3.493$ quiescent galaxy with a stellar mass of $3.1^{+0.1}_{-0.2} \times 10^{11} M_{\odot}$. The authors infer $SFR_{\text{obs}} > 1000 M_{\odot}/\text{yr}$ for about 0.5 Gyr beginning at $z \approx 7.2$ for it to have buildup its mass and suggest it to be a descendant of massive dusty star-forming galaxies at $5 < z < 7$ recently observed with ALMA. Scoville et al. (2017) report ALMA observations of a sample of 708 galaxies at $z = 0.3 - 4.5$ finding cases with $5000 < SFR_{\text{obs}}/(M_{\odot}/\text{yr}) < 10^4$ at $z \approx 3$ (their fig. 6; they assume $T_{\text{dust}} = 25 \text{ K}$). Fan et al. (2019) report a dust-obscured quasar at $z \approx 2.9$ in a galaxy with an inferred molecular gas mass of $8.4 \times 10^{10} M_{\odot}$ and $SFR_{\text{obs}} \approx 3000 - 7000 M_{\odot}/\text{yr}$ using various methods and for a derived $T_{\text{dust}} = 78.1 \text{ K}$. Riechers et al. (2020) report three dusty galaxies at $z > 5$ with deduced $SFR_{\text{obs}} = 870 \pm 100 M_{\odot}/\text{yr}$ ($T_{\text{dust}} \approx 35 \text{ K}$), $1030^{+190}_{-150} M_{\odot}/\text{yr}$ ($T_{\text{dust}} \approx 50 \text{ K}$) and $SFR_{\text{obs}} = 2500 \pm 700 M_{\odot}/\text{yr}$ ($T_{\text{dust}} \approx 92 \text{ K}$), each with a gas mass of a few $10^{10} M_{\odot}$, finding that their results suggest an $\approx 6 - 55$ times higher space density of such distant dusty systems within the first billion years after the Big Bang than thought until now. They also discuss that higher dust temperatures are expected at higher redshift.

In summary, the high redshift observations indicate rather high SFRs, consistent with the present model as can be deduced by comparing the SFRs quoted above with Fig. 16, but cooler dust temperatures may lower these somewhat.

8.2.3 Revised SFRs?

If the present model were relevant for the observed population of SMBHs then the model SFRs ought to be consistent with the SFRs deduced from high-red shift observations. The previous Sec. 8.2.2 suggests this to be the case, but the observed SFRs rely on a number of assumptions and in particular on the assumed value of T_{dust} and on the IMF.

In their fig. 9, Decarli et al. (2018) quantify how the assumed dust temperature influences the observationally derived SFRs. If T_{dust} in the star-forming system is 25 K instead of 50 K, then $SFR_{25 \text{ K}} \approx \kappa_{\text{dust}} \times SFR_{50 \text{ K}}$ with the correction factor $\kappa_{\text{dust}} \approx 0.1$, such that the values reported above, $1000 \lesssim SFR_{50 \text{ K}}/(M_{\odot}/\text{yr}) < 10^4$, would become $100 \lesssim SFR_{25 \text{ K}}/(M_{\odot}/\text{yr}) < 10^3$. However, some of the above mentioned results are obtained by independently fitting for T_{dust} with the argument that T_{dust} is expected to be higher at higher z .

At the same time, if the gwIMF/IGIMF is top-heavy (Sec. 3.3), then the true SFRs are much smaller in truth than the observed SFRs inferred using the invariant canonical IMF. This is the case because the photons which an

observer detects to measure the SFR are emitted mostly by the ionising stars while a top-heavy gwIMF changes the ratio between the mass in low-mass stars and high-mass stars towards smaller values (Yan et al. 2017; Jerabkova et al. 2018). The IGIMF models indicate that canonical observed values of $SFR_{\text{obs}} \approx 5000 - 10000 M_{\odot}/\text{yr}$ may in actuality be $SFR_{\text{true}} \approx 200 - 1000 M_{\odot}/\text{yr}$ largely independently of the metallicity (fig. 7 in Jerabkova et al. 2018). It is to be noted though that the correction factor used here is valid only if the SFR tracer is $H\alpha$ emission. For example, using the far-UV flux would increase the correction factor closer to a value of 1 (Pflamm-Altenburg et al. 2009). The impact of a top-heavy gwIMF on the observationally-deduced SFRs needs to be investigated in the future and is an important point to consider.

Furthermore, combining the maximum dust-temperature reduction factor with the IGIMF correction factor would imply $SFR_{\text{true}} \approx 10^{-2} SFR_{\text{obs}}$. Thus, a local spheroid with $M_{\text{gal}} = 10^{12} M_{\odot}$ would have had a physical counterpart at high redshift with $SFR_{\text{true}} \approx 30 M_{\odot}/\text{yr}$ and would need to form over a time span $\Delta\tau_{\text{true}} \approx 3 \times 10^{10} \text{ yr}$. This is clearly ruled out by the observed bulk ages of the local spheroids (Sec. 8.2.1). Presumably, the realistic case is that the dust temperatures adopted by the observational studies mentioned in Sec. 8.2.2 are approximately correct and that the IGIMF correction factor lies in the range 0.1 – 1.0 (for $SFR_{\text{obs}} \gtrsim 100 M_{\odot}/\text{yr}$, with the canonical gwIMF being used to infer SFR_{obs} , Jerabkova et al. 2018, and since the high-redshift SFR tracer is not the $H\alpha$ flux) such that

$$SFR_{\text{true}} = \kappa SFR_{\text{obs}} \quad (50)$$

with $\kappa \approx 0.5$ for the combined IGIMF and dust-temperature correction factor.

In summary, a tension has emerged between the high SFRs necessary to form the locally-observed massive spheroids within a Gyr and the here possibly implied smaller SFRs (if the dust temperature at very high redshift is in fact much smaller than usually assumed, and if the observed SFRs are overestimated due to the assumption of a canonical gwIMF). Given that local observations are typically more reliably interpreted than high redshift ones, it may well be that the local constraints (Sec. 8.2.1) might inform us about the observational biases acting in high-redshift observations. A plausible resolution of this tension might be that the downsizing times are somewhat longer together with a possible bias that typically the most-massive cluster would be seen in formation (which has a much lower SFR than the whole spheroid) in combination with the rarity of the most massive spheroids.

8.2.4 Implications of revised SFRs?

Would the model developed here be invalidated if the observed SFRs at high redshift are in fact much lower (Sec. 8.2.3) than implied by the downsizing time (Eq. 1)?

The observed emission from high redshift star-forming objects stems mostly from ionising stars. The mass, $M_{\text{max}, m^* > 8}$, in stars more massive than $8 M_{\odot}$ in the hyper-massive cluster with mass $M_{\text{ecl}, \text{max}}$, corresponds to an absolute luminosity (in some relevant wavelength range), $L_{\text{max}, m^* > 8}$, from all such stars combined. $M_{\text{max}, m^* > 8}$ associated with an observed object is thus fixed through the re-

ceived photons once the luminosity distance is known. The observationally deduced $L_{\max, m > 8}$ is transformed into a SFR by usually assuming an invariant (e.g. the canonical) gwIMF (Sec. 3.3) which essentially associates the luminosity, and thus mass of the ionising stellar component, with the total stellar mass including all low-mass stars. If the gwIMF is, however, top-heavy, then the same $M_{\max, m > 8}$ corresponds to a smaller total stellar mass including low mass stars.

A case in point is the measurement of the SFR using the $H\alpha$ flux, i.e. if $L_{\max, m > 8} = L_{H\alpha}$. Jerabkova et al. (2018) quantifies the galaxy-wide $L_{H\alpha}$ assuming a canonical gwIMF and the gwIMF calculated using the IGIMF theory (Sec. 3.3). Using $L_{H\alpha}$ leads to the largest sensitivity on the gwIMF shape since it is the most direct luminosity measure of the ionising-star massive-stellar content. The dependency of the true SFR on the gwIMF is quantified in fig.7 in Jerabkova et al. (2018) from which follows that for an observed value assuming the canonical gwIMF of $SFR_{H\alpha} \gtrsim 100 M_{\odot}/\text{yr}$ the correction factor is 0.1 – 0.05, i.e. $0.05 \lesssim SFR_{\text{true}}/SFR_{H\alpha} \lesssim 0.1$ with a weak dependence on metallicity.

This implies that $SFR_{\text{obs}} = 5000 M_{\odot}/\text{yr}$ would correspond to $SFR_{\text{true}} \approx 250 M_{\odot}/\text{yr}$ while $M_{\max, m > 8}$ remains the same. Fig. 17 depicts this situation. The implication is that the observed SFRs may in fact be lower by a factor of perhaps ten, but the mass in ionising stars corresponding to these SFRs remains unchanged, as explicitly pointed out by Chruślińska et al. (2020).

Thus, given the top-heavy gwIMF, the implied lower true SFRs transform to the same mass of the BH cluster as used in this model such that the model remains unaffected apart from requiring longer $\Delta\tau$ to form M_{igal} . In other words, Fig. 9 will change accordingly, while Fig. 10, Fig. 11 and 18 will not change. The number density of high redshift quasars (Sec. 7) would need to be recomputed taking into account the new $\Delta\tau$. This is not done here because the calculation presented there is very rough in any case and more detailed galaxy-formation models would need to be incorporated.

8.3 Other caveats

Further caveats and uncertainties, all of which can be included in future research programs, are touched upon in this section.

8.3.1 The IMF

The initial BH content of a cluster depends on the IMF, with the invariant canonical IMF (Sec. 3.1) having fewer and the variable IMF (Eq. 7) allowing for many more. But the invariant IMF is inconsistent with a broad range of observational constraints and basic star-formation theory robustly expects the IMF to vary with physical conditions (Sec. 3).

How does this variation look like in view of the many existing observational constraints and in view of the universality of the canonical IMF in Milky Way star-forming clouds? The coefficients used in Eq. 7 are originally obtained from GC data. The inferred initial conditions of the GCs are based on the semi-analytical model of Marks & Kroupa (2010) which quantifies the expansion of a young GC due to residual gas expulsion. The explicit constraints on the

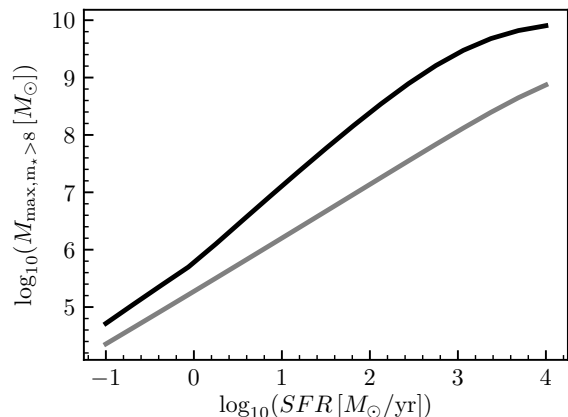


Figure 17. The mass, $M_{\max, m > 8}$, in stars more massive than $8 M_{\odot}$ in the first-formed most-massive cluster (of mass $M_{\text{ec1, max}}$ as obtained by solving Eq. 5) formed in the model with a box-shaped SFH as a function of the SFR of the spheroid ($SFR = M_{\text{igal}}/\Delta\tau$). This mass, $M_{\max, m > 8}$ yields the mass in BHs (Fig. 2) which, according to the present model, may coalesce to the SMBH. The gray line is the relation valid for the canonical IMF (corresponding to the dashed red line in the bottom-right panel of Fig. 11; note that the values here are larger because all stars with $m > 8 M_{\odot}$ are counted). The black line is the relation assuming the IMF is top-heavy (Eq. 7; corresponding to the dashed red line in the lower-left panel of Fig. 11; note that the values here are larger because all stars with $m > 8 M_{\odot}$ are counted). For example, an observer might deduce a high redshift star-forming spheroid to have $SFR_{\text{obs}} = 5000 M_{\odot}/\text{yr}$ which would correspond to $M_{\max, m > 8} \approx 3 \times 10^8 M_{\odot}$ assuming a canonical IMF (Sec. 3.1) and $\beta = 2.0$. If, however, the IMF and thus the gwIMF is top-heavy then the true SFR is smaller, $SFR_{\text{true}} \approx 250 M_{\odot}/\text{yr}$ (Jerabkova et al. 2018). This is the case because the same number of ionising photons emitted by the massive stars is observed, but it now corresponds to a smaller total stellar mass being formed. The mass in ionising stars corresponding to this smaller SFR is thus unchanged (Chruślińska et al. 2020), as is the mass in the BH sub-clusters which forms in these clusters.

IMF variation (Eq. 7) are obtained by Marks et al. (2012) who, by that process, account for the lack of low-mass stars in those GCs which have a low concentration (De Marchi et al. 2007), as well as taking the high dynamical mass-to-light ratios (Dabringhausen et al. 2009), the overabundance of low-mass X-ray binaries (Dabringhausen et al. 2012) in some UCDs and the Milky Way data into account. The need to evacuate a certain fraction of low-mass stars from a GC with an observed concentration, allows the massive-star IMF to be constrained because the massive stars provide the energy to expel the residual gas thereby expanding the mass-segregated young GC. But neither Marks & Kroupa (2010) nor Marks et al. (2012) take into account the impact on the long-term evolution of a GC by the implied large population of BHs (e.g. Breen & Heggie 2013a; Chatterjee et al. 2017; Giersz et al. 2019; Wang 2020). For $\alpha_3 < 1.5$, BHs would dominate the total mass of a GC. This can result in the fast dissolution of the luminous component of the GC and the formation of a dark cluster (Banerjee & Kroupa 2011). This would imply that the observed morphology of those GCs, which, according to the analysis by Marks et al. (2012) ought to have been born with a very top-heavy IMF, can probably not be matched to their observed versions. A

case in point is 47 Tuc (Hénault-Brunet et al. 2020). However, none of the existing modelling of the long-term evolution of GCs takes into account the evolving potential of the hosting galaxy (e.g. Speagle et al. 2014; de la Rosa et al. 2016; Mancini et al. 2019), and also other astrophysical processes not yet included in the first Gyr of GC evolution will affect the present-day appearance of GCs.

Thus, considering the sum of observational evidence (Sec. 3), the systematic variation of the IMF with density and metallicity appears to be a robust general trend. Indeed, if one were to construct an IMF dependency on metallicity and density on the embedded-star-cluster scale in view of the observational constraints from the Milky Way and other galaxies (Sec. 3.2 and 3.3), this dependency would need to be similar to Eq. 7. The ultra-low metallicity IMF may even be much more top-heavy than assumed here. For instance, in the Galactic centre, the observed population of very young stars appears to follow a very top-heavy IMF with low-mass stars apparently largely missing (Sec. 3.2) despite being a metal-rich population. This may indicate a more extreme variation of the IMF than encompassed here through Eq. 7, and would imply even larger BH sub-cluster masses than in the models computed here.

Thus, given the above caveats, the specific formulation via Eq. 7 is strongly suggestive but not definitive. In view of this we have also included models with an invariant canonical IMF.

8.3.2 *The low-mass stars and other simplifications*

In finding the collapsing solutions, we ignored the low mass stars. These are likely to help (speed-up) the shrinkage of the BH sub-cluster due to energy equipartition. We applied, in Sec. 4.1, the balanced-evolution theory as formulated via eq. 1 in Antonini et al. (2019) to the case of a cluster of equal-mass BHs. By doing so we neglected the rest of the stellar cluster, assumed the BH sub-cluster to be self-gravitating and thermally isolated from its surroundings. Clearly these are significant simplifications, but the complexity of the realistic situation which involves the dynamical evolution and the heating rate through BH binaries being modulated by the gas inflow warrants an argument in support of these simplifications to ensure technical feasibility. The stellar component is likely to enhance the mass growth of the central massive BH since it will also be shrunk onto the BH cluster through the in-falling gas. The BHs will have different masses in the BH sub-cluster. This speeds-up core collapse and merging rates (e.g. Khalisi et al. 2007). We have ignored the likely rotation of the BH sub-cluster, but rotating systems collapse faster, the collapse being accelerated even more if the BHs have a mass spectrum (Kim et al. 2004). Spin-spin interactions during BH mergers have not been considered here, but simulations of BH clusters in which the BHs have no, aligned or randomly oriented spins do not lead to measurable differences in the merging behaviour (Brem et al. 2013).

8.3.3 *Further growth of the SMBH seeds*

The SMBH-seed will additionally grow through gas accretion in the time $\Delta\tau$ during which the spheroid forms. The

gas in-flow and out-flows will be modulated by the accretion activity of the SMBH-seed(s), being dependent also on the progressive metal enrichment of the gas as the spheroid forms (e.g. Yan et al. 2019a). The accretion of gas onto the BHs and the likely feedback effect are discussed in Secs 8.1. Ultimately, it will be necessary to perform N-body or equivalent simulations of such systems, but these currently remain out of computational reach (e.g. Lee 1993, 1995; Spurzem 1999; Kupi et al. 2006; Brem et al. 2013; Giersz et al. 2015; Rodriguez et al. 2016; Wang et al. 2016). Once the bulk of the spheroid is assembled, their central SMBHs may grow slowly through the disruption of stars (e.g. Brockamp et al. 2011), and this will need to be also included in future more comprehensive modelling of the SMBH–spheroid correlation.

8.3.4 *Multi-generation clusters and their merging*

As the spheroid assembles, many massive clusters will form near its centre (Eq. 6). These will have their own BH sub-clusters and the masses of these will depend on how quickly the IMF changes to a more canonical form as the metallicity of the gas from which they form increases. Whether or not the BH sub-cluster in any one of these evolves sufficiently rapidly into the pressureless state to allow collapse to a SMBH-seed depends on whether the hosting cluster can accrete a sufficient amount of gas for a sufficiently long time from the forming spheroid. Thus, more than one SMBH-seed is likely to co-exist near the centre of the forming spheroid, but BH sub-clusters which have not collapsed should also exist. These would be identifiable as “dark clusters” (Banerjee & Kroupa 2011). Gas inflow and dynamical friction on field stars (Bekki 2010) brings the most massive clusters to merge near the centre of the spheroid, enhancing the growth of the central SMBH-seed which forms from the first ultra-metal-poor star-burst cluster. Observational evidence for this process, albeit in dwarf galaxies, has been documented (Fahrion et al. 2020). The detailed physical evolutionary processes operating in the interactions and mergers of multiple massive star clusters and their BH components leading to the formation of the present-day nuclear regions in spheroids and the continued build-up of the nuclear cluster in late-type galaxies are complex and need special attention (e.g. Arca-Sedda et al. 2015, 2016; Arca Sedda et al. 2019, for a review of nuclear star clusters see Neumayer et al. 2020).

8.3.5 *Multiple SMBH seeds*

Mergers between SMBH-seeds formed in the individual cluster discussed in Sec. 8.3.4 are likely to contribute to the growth of the SMBHs and will add a stochastic element to the final mass correlation between SMBH and spheroid mass (Fig. 11). Such mergers may lead to recoils from gravitational wave emission and this would imply displaced SMBHs from the centres of their hosting spheroids (Lena et al. 2014). Dynamical friction of the SMBHs on the stellar population of the spheroid will bring the SMBH back to the centre within the mass-segregation time scale of about 10^9 yr (Eq. 35). The observed absence of a significant population of displaced SMBHs, which Lena et al. (2014) use to constrain the merging rate of galaxies, thus appears to be broadly consistent with the model developed here.

Less-massive SMBHs, IMBHs, or dark clusters would not suffer sufficient dynamical friction to merge with the central cluster though such that the inner regions of spheroids should, according to the present model, contain many such objects. The IRS13E object near the Galactic centre source Sgr A* may be such an example (Banerjee & Kroupa 2011; Tsuboi et al. 2017, but see Reid & Brunthaler 2020 for astrometric limits on such companions of Sgr A*). Another example may be the candidate 12-yr-period binary-SMBH in the active galactic nucleus or blazar OJ287 (Britzen et al. 2018; Laine et al. 2020).

8.3.6 IMBHs

As can be seen from Fig. 8, the process of BH cluster collapse presented here is not limited to the formation of SMBHs. Indeed, assuming 5 per cent of $M_{\text{BH},0}$ merge and in the case of a low to moderate gas fraction ($\eta \lesssim 1$), the formation of IMBH seeds is possible within a wide range of initial parameters which may be in-line with the hierarchical scenario of the formation of massive galaxies. Challenges to be addressed in this context are that the model presented here relies on massive spheroids harbouring a SMBH to have formed rapidly, because smaller progenitors would violate the $M_{\text{ecl,max}} - \text{SFR}$ relation (Eq. 5), that the observed metallicity and alpha-element abundances of the spheroids need to be fulfilled, and that the IMBHs would subsequently have to merge rapidly by some mechanism to form the SMBHs observed at very high redshifts. For example, Wirth & Bekki (2020) study models in which pre-existing IMBHs assemble at the centre of a UCD through dynamical friction where they form a sub-cluster in which mergers lead to the build-up of an SMBH.

The model presented here though *allows* the direct formation of the SMBH-seeds on a very short time-scale.

9 CONCLUSION

The problem of the observed rapid appearance of quasars in the very young Universe and of the mass correlation between the SMBH and its spheroid are considered. Here we concentrate on a conservative approach resting on the properties of observed stellar populations and known stellar-dynamical processes. The model relies on the mass in massive stars in the first-formed star-burst cluster(s) near the centre of the later spheroid to correlate with the global SFR at assembly time of the bulk of the spheroid as given by observational data in the nearby Universe. The sequence of star-burst clusters assembled at the centre of the forming spheroid provides the seed-SMBH(s) and the formation of the spheroid leads to gas inflow which shrinks and merges the star-burst cluster's stellar-mass BHs and leads to additional mass growth of the seed(s). It is this physical correlation between the central gas density and the proto-spheroid gas mass which ultimately leads to the observed SMBH-mass-spheroid-mass correlation.

By applying the IGIMF theory, i.e. the observationally independently derived relations describing stellar populations in individual star-formation events on a molecular cloud-core scale (i.e. embedded clusters) and their distribution by mass in a star-forming galaxy, to assess the expected

content of stellar-mass BHs in the very early Universe, this work suggests that SMBH-seeds with masses up to a few times $10^6 M_{\odot}$ might emerge within a few hundred Myr of the first star formation (Figs 11 and 18). This is a conservative estimate relying on only 5 per cent of the BH content of the first massive cluster at the centre of the forming spheroid to merge to the SMBH seed.

The existence of quasars within ≈ 500 Myr after the birth of the Universe and the existence of massive SMBHs at lower redshift is explained as a two-stage process (see Fig. 12 in Sec. 7 for a visualisation using explorative models):

During the first phase, an extremely massive ($> 10^8 M_{\odot}$) star-burst cluster forms as the first ultra-low-metallicity population with a top-heavy IMF (Jerabkova et al. 2018; Yan et al. 2019b,a) at the centre of the forming spheroid. This cluster might appear, in terms of emission line widths, spatial resolution and luminosity, similar to a quasar (Jerabkova et al. 2017, Sec. 3.4), but this needs to be ascertained using radiation-hydrodynamic simulations. This phase lasts a few dozen Myr during which the massive stars explode as supernovae driving an energetic and metal-rich cluster wind. Once the last core-collapse supernova explodes, leaving the BH sub-cluster, such an object fades, and this is where the SMBH formation ensues as per the model presented here if the BH sub-cluster accretes gas from the surrounding environment.

During the second phase, which begins after the first few dozen Myr when the cluster luminosity has decreased significantly (Jerabkova et al. 2017; Ploekinger et al. 2019), gas will fall onto the central region from the still violently forming spheroid (Sec. 4). The key mechanism for the appearance of the actual SMBH-seeds is accretion of gas from the surrounding forming spheroid into the central region. The gas accretion leads to contraction of the BH containing cluster (modelled here as a BH sub-cluster, ignoring the stellar component) to a relativistic state (Eq. 20) within a few hundred Myr from which it collapses through energy loss by radiating gravitational waves during BH-BH encounters. The BH sub-cluster has an incompressible phase-space distribution function and would, if left on its own, be in a state of balanced evolution (with the rest of the stellar cluster), but the gas spatially shrinks it to the point where its equation of state becomes pressure-less, allowing the relativistic collapse to a SMBH-seed. Post-Newtonian N-body simulations show such a BH sub-cluster to core-collapse within 10–15 median two body relaxation times leading to runaway merging between the BHs and coalescence of the core of the BH sub-cluster to a SMBH-seed (Lee 1995) which may amount to 5 per cent of the BH sub-cluster mass (Lee 1993; Kuper et al. 2006). Due to the small physical size, core collapse occurs within a dozen Myr once the BH sub-cluster reaches this relativistic state. The SMBH-seed mass may in reality reach much larger values if the compression through the gas forces faster shrinkage, faster BH-BH coalescences and if it would squeeze the rest of the stellar cluster into the BHs. The key physical mechanism provided by the in-falling gas from the forming spheroid is thus to force the BH sub-cluster out of its balanced evolution and into the state where core collapse occurs within a dozen Myr.

The first and second phase together last as long as the spheroid continues to form on the downsizing time-scale (Eq. 1). As a case in point, the model developed here is

applied in Sec. 7.3 to the $1.5 \times 10^9 M_\odot$ SMBH in the luminous quasar Pōniuā'ena at $z = 7.5$ discovered by Yang et al. (2020). Since spheroids remain largely dormant once they have formed (Sec. 8.2.1), the SMBH–spheroid correlation will not change significantly with redshift once spheroid assembly quenches, although some slow further growth will likely take place (Sec. 8.3.3). Indeed, Suh et al. (2020) find a lack of evolution of the SMBH–spheroid relation out to $z \approx 2.5$.

While possibly being relevant for the rapid emergence of SMBHs in the Universe, the present model also at the same time relaxes the need to interpret extremely high redshift quasars as already formed accreting very massive SMBHs. This is explicitly shown in Sec. 7 with a calculation based on the formation times of galaxies adopted from Thomas et al. (2005) and the different model phases of the quasars. In that section also the possible issue of missing quasars is discussed.

The model studied here might be relevant for explaining why evidence for IMBHs exists only at the centres of galaxies, them not having been found in star clusters (Baumgardt et al. 2019): If a BH sub-cluster is embedded only in a star cluster and is locked in a state of balanced evolution thereby slowly ejecting its BH content through BH–BH binary encounters, it will core-collapse on a time-scale too long to form a substantial IMBH (e.g. Giersz et al. 2015). The same BH sub-cluster which suffers gas infall from the forming and evolving galaxy will, on the other hand, be compressed sufficiently for runaway merging. The results obtained here (Fig. 8) suggest that only when the BH sub-cluster has a mass $M_{\text{BH},0} > 10^4 M_\odot$ will the relativistic state be reached. More research on this question is clearly desired.

According to the present model, SMBHs are expected to occur from the formation of spheroids, i.e., a disk galaxy with a classical bulge should have an SMBH, while a disk galaxy with the same rotation speed but without a classical bulge may not host an SMBH, or at best, only a compact central BH sub-cluster.

Noteworthy is that the SMBH–spheroid mass correlation (Figs 11 and 18) comes out naturally in terms of its slope, without needing to adjust any parameters to achieve this purpose, the model being consistent with observational data on pc-scale stellar systems (Fig. 1) and with galaxy-scale stellar populations, as it results from applying the IGIMF theory (Sec. 3.3). A correlation emerges also if the IMF remains canonical, but in a weaker form (Figs 11 and 18). But the IMF variation with metallicity and density as inferred from independent data by Dabringhausen et al. (2009, 2012); Marks et al. (2012) implies, surprisingly, a near-perfect correlation in excellent agreement with the observed one. Further Eddington-limited mass-growth of the thus formed SMBH-seeds will depend on further infall of gas as modulated by the formation of the spheroid and may lead to extremely massive SMBHs within an additional few hundred Myr period as allowed by the down-sizing time (Eq. 1). Interestingly, taking the conservative estimate that if only the 5 per cent SMBH-seed masses grow for about 345 Myr (Sec. 6) at the super-Eddington rate ($\epsilon_f = 0.1$, Sec. 8.1), then they reach the observed correlation (Eq. 34). That is, this model achieves a most remarkable consistency of time-scales in that the need to grow the SMBH-seeds per spheroid to the observed SMBH masses comes out to be within the

downsizing time. *This is not a trivial correspondence, because the result might have been that the growth time would have turned out to be much longer than the downsizing time, which would have violated the model.*

Note also that if all of the mass formed into stars in all the N_{gen} central most-massive clusters would be combined into a black hole, then the resulting SMBH–spheroid correlation is impressively consistent with the data (dotted line in Figs 11 and 18).

The here presented model is expected to lead to a dispersion of the SMBH masses at a given present-day spheroid mass because the SMBH-seeds are expected to not be identical, given the stochasticity of mergers between central clusters and of the gas infall feeding SMBH-seed growth. According to the present model, the correlation of SMBH–spheroid ceases near a spheroid mass of $10^9 M_\odot$ (for $\beta = 2.0$, Fig. 11) and $10^{9.6} M_\odot$ (for $\beta = 2.4$, Fig. 18) such that at lower masses only the central (i.e. nuclear) star cluster with its central component of BHs takes over the correlation towards smaller masses due to Eq. 5. This appears to be consistent with this same observed phenomenon (Wehner & Harris 2006; Capuzzo-Dolcetta & Tosta e Melo 2017).

Since the environment of the central cluster need not necessarily become a massive spheroid, this object may, under certain circumstances, later appear as an isolated UCD with a SMBH in it as observed (Sec. 1). This may also be relevant to the finding of a quasar at a redshift of 3.84 which is inferred to be a SMBH weighing $\approx 2.5 \times 10^{10} M_\odot$ embedded in a host with stellar mass $\lesssim 6.3 \times 10^{10} M_\odot$ (Schramm et al. 2019). This may happen in the present context if mergers of forming spheroids eject some of their very massive clusters with associated material. An implication of this scenario would be that some such ejected UCDs may have been cutoff from the gas accretion from their forming spheroid such that their BH sub-cluster may not have reached the relativistic limit. The SMBH detected in such UCDs would then constitute a compact (pc-scale) sub-cluster of BHs which is in the state of balanced evolution, rather than an actual SMBH. At the moment this is merely a speculation, and detailed computations would be needed to test if this scenario for the formation of SMBH-bearing UCDs is viable.

The model studied here has two implications: (i) The central region of spheroids should contain many dark clusters and SMBH-seeds (including IMBHs) as left over relics (Sec. 8.3.5). (ii) When the BH sub-clusters enter the relativistic phase, they will radiate gravitational waves at an increasing rate from the many BH–BH mergers, including the final runaway collapse to the SMBH-seed. This emission ought to be detectable with the appropriate gravitational wave observatories, and must not be wrongly interpreted as a sign of the hierarchical assembly of early galaxies in their speculative dark matter halos. It will be useful to calculate the signal expected from SMBH assembly according to the model presented here.

The here presented results rest on, by computational necessity, important simplifications (Sec. 8). Sec. 8.2 dissects the current observational evidence for and against the high SFRs that ought to be evident at high redshift when the massive spheroids were forming, and how the evidence compares with the theory developed here. Thus, while encouraging, much more research will be needed to assess the importance of gas accretion onto the BH sub-cluster, its for-

mation and evolution in a realistic spheroid formation context. We note that the model presented here would not work (i) if either the bulk of a spheroid does not form monolithically and thus with the high SFRs assumed, or (ii) the first star-formation events at extremely low metallicity and modest SFRs do not produce hyper-massive star-burst clusters with a top-heavy IMF before the bulk of the spheroid assembles later. It is quite likely that a combination of processes play a role. For example, a hyper-massive star (formed either as a population III object or from runaway stellar mergers in the central hyper-massive star cluster, Sec. 1) may directly collapse to a SMBH-seed which subsequently accretes such that the outcome (the SMBH-mass-spheroid-mass correlation) emerges also just as in the present model, although it is not clear if this scenario can reach the large SMBH-seed masses as in the present model such that the further growth were consistent with the downsizing time. It is also imaginable that the squeezing of a cluster of BHs into the relativistically unstable regime studied here through gas drag in addition to the coalescence of the whole stellar body of the nuclear cluster (generations) by gas drag, leads to an, in effect, hyper-massive first star, similarly as discussed in the Introduction. This hypothetical possibility would be physically related to the postulated Thorne-Zytkow objects (Thorne & Zytlow 1975, 1977). Observationally, it will be important to constrain the number density of quasars at the highest reachable redshifts and to assess the masses the most massive SMBHs may reach as is the goal of the Gargantua search strategy (Brockamp et al. 2016).

ACKNOWLEDGEMENTS

An early version of this research programm was begun in Concepcion, Chile, at the Modelling and Observing Dense Stellar Systems 15 (MODEST15) conference. Pavel Kroupa and Long Wang thank the organisers of that memorable event (notably Mike Fellhauer), Sverre Aarseth, Paulina Assmann, Joerg Dabringhausen and Rainer Spurzem for detailed discussions on the N-body dynamics of BH clusters. We thank Moritz Haslbauer for useful discussions on galaxy evolution and Zhiqiang Yan and Alexandre Vazdekis for important discussions on the formation of elliptical galaxies. Pavel Kroupa and Ladislav Šubr acknowledge support from the Grant Agency of the Czech Republic under grant number 20-21855S. Tereza Jerabkova acknowledges support through a two-year European Southern Observatory (ESO) Studentship in Garching, the Erasmus+ programme of the European Union under grant number 2017-1-CZ01- KA203-035562 on La Palma, and the European Space Agency fellowship programme. Long Wang acknowledges support through an Alexander von Humboldt Fellowship while being hosted by the Stellar Populations and Dynamics Research (SPODYR) group at the University of Bonn. Long Wang also acknowledges the present support through a Japan Society for the Promotion of Science International Research Fellowship. Some of this work was performed at ESO in Garching and Pavel Kroupa thanks ESO for a science-visiting position in 2019. Pavel Kroupa and Long Wang thank the non-professorial staff of the Argelander-Institute for Astronomy for technical support. This work benefited from the International Space Science Institute (ISSI/ISSI-BJ) in Bern

and Beijing, thanks to the funding of the team “Chemical abundances in the ISM: the litmus test of stellar IMF variations in galaxies across cosmic time” (Donatella Romano and Zhi-Yu Zhang). Pavel Kroupa is grateful to the Isaac Newton Group staff on La Palma for hospitality where a part of this manuscript was written just prior to the Corona Crisis and acknowledges the Erasmus+ programme of the European Union under grant number 2017-1-CZ01- KA203-035562 for enabling this visit while on a contract with the Czech Academy of Sciences through Ondřejov Observatory. Havelka Kuchine (“knedlikarna”) in Prague was an essential location throughout this work – Knedlikum zdar!

DATA AVAILABILITY

The results are based on calculated models as described within this manuscript.

REFERENCES

- Abbott B. P., et al., 2016, *Phys. Rev. Lett.*, 116, 061102
 Abbott B. P., et al., 2019, *Physical Review X*, 9, 031040
 Adams F. C., Fatuzzo M., 1996, *ApJ*, 464, 256
 Adams F. C., Laughlin G., 1996, *ApJ*, 468, 586
 Afanasiev A. V., et al., 2018, *MNRAS*, 477, 4856
 Ahn C. P., et al., 2017, *ApJ*, 839, 72
 Ahn C. P., et al., 2018, *ApJ*, 858, 102
 Alexander T., Natarajan P., 2014, *Science*, 345, 1330
 Alister Seguel P. J., Schleicher D. R. G., Boekholt T. C. N., Fellhauer M., Klessen R. S., 2019, *arXiv e-prints*, p. arXiv:1912.01737
 Ando R., et al., 2017, *ApJ*, 849, 81
 Antonini F., Gieles M., Gualandris A., 2019, *MNRAS*, 486, 5008
 Arav N., Xu X., Miller T. R., Kriss G. A., Plesha R. J., 2020, *arXiv e-prints*, p. arXiv:2003.08688
 Arca-Sedda M., Capuzzo-Dolcetta R., Antonini F., Seth A., 2015, *ApJ*, 806, 220
 Arca-Sedda M., Capuzzo-Dolcetta R., Spera M., 2016, *MNRAS*, 456, 2457
 Arca Sedda M., Berczik P., Capuzzo-Dolcetta R., Fragione G., Sobolenko M., Spurzem R., 2019, *MNRAS*, 484, 520
 Ardaneh K., Luo Y., Shlosman I., Nagamine K., Wise J. H., Begelman M. C., 2018, *MNRAS*, 479, 2277
 Bañados E., et al., 2016, *ApJS*, 227, 11
 Bañados E., et al., 2018, *Nature*, 553, 473
 Balakrishna Subramani V., Kroupa P., Shenavar H., Muralidhara V., 2019, *MNRAS*, 488, 3876
 Banerjee S., 2017, *MNRAS*, 467, 524
 Banerjee S., Kroupa P., 2011, *ApJ*, 741, L12
 Banerjee S., Kroupa P., 2012, *A&A*, 547, A23
 Banerjee S., Baumgardt H., Kroupa P., 2010, *MNRAS*, 402, 371
 Banerjee S., Kroupa P., Oh S., 2012, *MNRAS*, 426, 1416
 Banerjee S., Belczynski K., Fryer C. L., Berczik P., Hurley J. R., Spurzem R., Wang L., 2019, *arXiv e-prints*, p. arXiv:1902.07718
 Bartko H., et al., 2010, *ApJ*, 708, 834
 Bastian N., Covey K. R., Meyer M. R., 2010, *ARA&A*, 48, 339
 Basu S., Das A., 2019, *arXiv e-prints*, p. arXiv:1906.05138
 Baumgardt H., Makino J., 2003, *MNRAS*, 340, 227
 Baumgardt H., Kroupa P., Parmentier G., 2008, *MNRAS*, 384, 1231
 Baumgardt H., et al., 2019, *MNRAS*, 488, 5340
 Beccari G., et al., 2017, *A&A*, 604, A22
 Begelman M. C., Volonteri M., 2017, *MNRAS*, 464, 1102

- Bekenstein J., Milgrom M., 1984, *ApJ*, 286, 7
- Bekki K., 2010, *MNRAS*, 401, 2753
- Bekki K., Mackey A. D., 2009, *MNRAS*, 394, 124
- Belczynski K., et al., 2016, *A&A*, 594, A97
- Bender R., Surma P., Doebereiner S., Moellenhoff C., Madejsky R., 1989, *A&A*, 217, 35
- Bender R., Burstein D., Faber S. M., 1992, *ApJ*, 399, 462
- Boco L., Lapi A., Danese L., 2020, arXiv e-prints, p. arXiv:2002.03645
- Breen P. G., Heggie D. C., 2013a, *MNRAS*, 432, 2779
- Breen P. G., Heggie D. C., 2013b, *MNRAS*, 436, 584
- Brem P., Amaro-Seoane P., Spurzem R., 2013, *MNRAS*, 434, 2999
- Britzen S., et al., 2018, *MNRAS*, 478, 3199
- Brockamp M., Baumgardt H., Kroupa P., 2011, *MNRAS*, 418, 1308
- Brockamp M., Baumgardt H., Britzen S., Zensus A., 2016, *A&A*, 585, A153
- Brodie J. P., Romanowsky A. J., Strader J., Forbes D. A., 2011, *AJ*, 142, 199
- Brown P., Hindmarsh A., 1989, *Journal of Applied Mathematics and Computing*, 31, 40
- Brüns R. C., Kroupa P., Fellhauer M., Metz M., Assmann P., 2011, *A&A*, 529, A138
- Capuzzo-Dolcetta R., Tosta e Melo I., 2017, *MNRAS*, 472, 4013
- Carr B. J., Hawking S. W., 1974, *MNRAS*, 168, 399
- Chabrier G., 2003, *PASP*, 115, 763
- Chatterjee S., Rodriguez C. L., Rasio F. A., 2017, *ApJ*, 834, 68
- Chevalier R. A., Clegg A. W., 1985, *Nature*, 317, 44
- Chruślińska M., Jeřábková T., Nelemans G., Yan Z., 2020, *A&A*, 636, A10
- Comerón S., Salo H., Peletier R. F., Mentz J., 2016, *A&A*, 593, L6
- Conselice C. J., Wilkinson A., Duncan K., Mortlock A., 2016, *ApJ*, 830, 83
- Dabringhausen J., 2019, *MNRAS*, 490, 848
- Dabringhausen J., Hilker M., Kroupa P., 2008, *MNRAS*, 386, 864
- Dabringhausen J., Kroupa P., Baumgardt H., 2009, *MNRAS*, 394, 1529
- Dabringhausen J., Fellhauer M., Kroupa P., 2010, *MNRAS*, 403, 1054
- Dabringhausen J., Kroupa P., Pflamm-Altenburg J., Mieske S., 2012, *ApJ*, 747, 72
- Davies M. B., Miller M. C., Bellovary J. M., 2011, *ApJ*, 740, L42
- De Marchi G., Paresce F., Pulone L., 2007, *ApJ*, 656, L65
- De Masi C., Matteucci F., Vincenzo F., 2018, *MNRAS*, 474, 5259
- De Propriis R., et al., 2014, *MNRAS*, 444, 2200
- Decarli R., et al., 2018, *ApJ*, 854, 97
- Dekel A., et al., 2009, *Nature*, 457, 451
- Delgado-Serrano R., Hammer F., Yang Y. B., Puech M., Flores H., Rodrigues M., 2010, *A&A*, 509, A78
- Deng H., Vilenkin A., 2017, *J. Cosmology Astropart. Phys.*, 12, 044
- Devereux N., 2019, arXiv e-prints, p. arXiv:1906.10085
- Di Matteo T., Croft R. A. C., Feng Y., Waters D., Wilkins S., 2017, *MNRAS*, 467, 4243
- Díaz V. B., Schleicher D. R. G., Bovino S., FFibla P., Riaz R., Vanaverbeke S., Olave C., 2019, *Boletín de la Asociación Argentina de Astronomía La Plata Argentina*, 61, 166
- Dib S., Kim J., Shadmehri M., 2007, *MNRAS*, 381, L40
- Eftekharzadeh S., et al., 2015, *MNRAS*, 453, 2779
- Egusa F., Sofue Y., Nakanishi H., 2004, *PASJ*, 56, L45
- Egusa F., Kohno K., Sofue Y., Nakanishi H., Komugi S., 2009, *ApJ*, 697, 1870
- Eilers A.-C., Hennawi J. F., Davies F. B., 2018, *ApJ*, 867, 30
- Elmegreen B. G., Efremov Y. N., 1997, *ApJ*, 480, 235
- Event Horizon Telescope Collaboration et al., 2019, *ApJ*, 875, L1
- Fahrion K., et al., 2020, arXiv e-prints, p. arXiv:2001.02241
- Famaey B., McGaugh S. S., 2012, *Living Reviews in Relativity*, 15, 10
- Fan L., Knudsen K. K., Han Y., Tan Q.-h., 2019, *ApJ*, 887, 74
- Farina E. P., et al., 2019, arXiv e-prints, p. arXiv:1911.08498
- Favata M., Hughes S. A., Holz D. E., 2004, *ApJ*, 607, L5
- Fellhauer M., Kroupa P., 2002, *MNRAS*, 330, 642
- Ferrarese L., Merritt D., 2002, *Phys. World*, 15N6, 41
- Figer D. F., 2005, *Nature*, 434, 192
- Finkelstein S. L., et al., 2013, *Nature*, 502, 524
- Fioc M., Rocca-Volmerange B., 1997, *A&A*, 326, 950
- Fontanot F., De Lucia G., Hirschmann M., Bruzual G., Charlot S., Zibetti S., 2017, *MNRAS*, 464, 3812
- For B.-Q., Bekki K., 2017, *MNRAS*, 468, L11
- Forrest B., et al., 2020, *ApJ*, 890, L1
- Frank J., King A., Raine D. J., 2002, *Accretion Power in Astrophysics: Third Edition*
- Fryer C. L., Belczynski K., Wiktorowicz G., Dominik M., Kalogera V., Holz D. E., 2012, *ApJ*, 749, 91
- Fujii M. S., Portegies Zwart S., 2014, *MNRAS*, 439, 1003
- Fujimoto S., et al., 2020, arXiv e-prints, p. arXiv:2003.00013
- Fukugita M., Peebles P. J. E., 2004, *ApJ*, 616, 643
- Fukui Y., Kawamura A., 2010, *ARA&A*, 48, 547
- Fukui Y., et al., 1999, *PASJ*, 51, 745
- Gadotti D. A., Kauffmann G., 2009, *MNRAS*, 399, 621
- Gibson B. K., Matteucci F., 1997, *MNRAS*, 291, L8
- Gieles M., Heggie D. C., Zhao H., 2011, *MNRAS*, 413, 2509
- Giersz M., Spurzem R., 2003, *MNRAS*, 343, 781
- Giersz M., Leigh N., Hypki A., Lützgendorf N., Askar A., 2015, *MNRAS*, 454, 3150
- Giersz M., Askar A., Wang L., Hypki A., Leveque A., Spurzem R., 2019, *MNRAS*, 487, 2412
- Glazebrook K., et al., 2017, *Nature*, 544, 71
- Goswami S., Umbreit S., Bierbaum M., Rasio F. A., 2012, *ApJ*, 752, 43
- Gravity Collaboration et al., 2018, *A&A*, 615, L15
- Gruzinov A., Levin Y., Matzner C. D., 2020, *MNRAS*, 492, 2755
- Gunawardhana M. L. P., et al., 2011, *MNRAS*, 415, 1647
- Gürkan M. A., Freitag M., Rasio F. A., 2004, *ApJ*, 604, 632
- Haemmerlé L., Mayer L., Klessen R. S., Hosokawa T., Madau P., Bromm V., 2020, arXiv e-prints, p. arXiv:2003.10533
- Haghi H., Khalaj P., Hasani Zonoozi A., Kroupa P., 2017, *ApJ*, 839, 60
- Hasani Zonoozi A., Haghi H., Kroupa P., 2016, preprint, (arXiv:1605.04913)
- Hashimoto T., et al., 2018, *Nature*, 557, 392
- Heckman T. M., Best P. N., 2014, *ARA&A*, 52, 589
- Heggie D. C., 1975, *MNRAS*, 173, 729
- Heggie D., Hut P., 2003, *The Gravitational Million-Body Problem: A Multidisciplinary Approach to Star Cluster Dynamics*
- Hénault-Brunet V., Gieles M., Strader J., Peuten M., Balbinot E., Douglas K. E. K., 2020, *MNRAS*, 491, 113
- Hénon M., 1961, *Annales d'Astrophysique*, 24, 369
- Hénon M., 1965, *Annales d'Astrophysique*, 28, 62
- Hénon M., 1975, in Hayli A., ed., *IAU Symposium Vol. 69, Dynamics of the Solar Systems*. p. 133
- Hilker M., Baumgardt H., Infante L., Drinkwater M., Evstigneeva E., Gregg M., 2007, *A&A*, 463, 119
- Hills J. G., 1975, *AJ*, 80, 809
- Hindmarsh A., 1983, *ODEPACK, a Systematized Collection of ODE Solvers*, in *Scientific Computing*. Elsevier
- Hopkins A. M., 2018, *Publ. Astron. Soc. Australia*, 35, 39
- Hoversten E. A., Glazebrook K., 2008, *ApJ*, 675, 163
- Hunter D. A., Elmegreen B. G., Dupuy T. J., Mortonson M., 2003, *AJ*, 126, 1836
- Hypki A., Giersz M., 2013, *MNRAS*, 429, 1221
- Janz J., Forbes D. A., Norris M. A., Strader J., Penny S. J., Fagioli M., Romanowsky A. J., 2015, *MNRAS*, 449, 1716

- Jerabkova T., Kroupa P., Dabringhausen J., Hilker M., Bekki K., 2017, *A&A*, 608, A53
- Jerabkova T., Hasani Zonoozi A., Kroupa P., Beccari G., Yan Z., Vazdekis A., Zhang Z. Y., 2018, *A&A*, 620, A39
- Jiang L., et al., 2016, *The Astrophysical Journal*, 833, 222
- Joncour I., Duchêne G., Moraux E., Motte F., 2018, *A&A*, 620, A27
- Joseph R. D., Wright G. S., 1985, *MNRAS*, 214, 87
- Joshi K. J., Rasio F. A., Portegies Zwart S., 2000, *ApJ*, 540, 969
- Kalari V. M., Carraro G., Evans C. J., Rubio M., 2018, preprint, ([arXiv:1801.01490](https://arxiv.org/abs/1801.01490))
- Karachentsev I. D., 2012, *Astrophysical Bulletin*, 67, 123
- Karachentsev I. D., Telikova K. N., 2018, *Astronomische Nachrichten*, 339, 615
- Karachentsev I. D., Karachentseva V. E., Huchtmeier W. K., Makarov D. I., 2004, *AJ*, 127, 2031
- Karachentsev I. D., Makarov D. I., Kaisina E. I., 2013, *AJ*, 145, 101
- Keenan R. C., Barger A. J., Cowie L. L., 2013, *ApJ*, 775, 62
- Khalisi E., Amaro-Seoane P., Spurzem R., 2007, *MNRAS*, 374, 703
- Kim H., Kim W.-T., 2009, *ApJ*, 703, 1278
- Kim E., Lee H. M., Spurzem R., 2004, *MNRAS*, 351, 220
- Kim Y., et al., 2018, preprint, ([arXiv:1802.02782](https://arxiv.org/abs/1802.02782))
- Koen C., 2006, *MNRAS*, 365, 590
- Kormendy J., Ho L. C., 2013, *ARA&A*, 51, 511
- Kormendy J., Drory N., Bender R., Cornell M. E., 2010, *ApJ*, 723, 54
- Kormendy J., Bender R., Cornell M. E., 2011, *Nature*, 469, 374
- Kotilainen J. K., Falomo R., Decarli R., Treves A., Uslenghi M., Scarpa R., 2009, *ApJ*, 703, 1663
- Krajinović D., et al., 2020, *A&A*, 635, A129
- Kroupa P., 1995, *MNRAS*, 277, 1491
- Kroupa P., 1998, *MNRAS*, 300, 200
- Kroupa P., 2001, *MNRAS*, 322, 231
- Kroupa P., 2002, *Science*, 295, 82
- Kroupa P., 2008, in Aarseth S. J., Tout C. A., Mardling R. A., eds, *Lecture Notes in Physics*, Berlin Springer Verlag Vol. 760, *The Cambridge N-Body Lectures*. p. 181 ([arXiv:0803.1833](https://arxiv.org/abs/0803.1833)), doi:10.1007/978-1-4020-8431-7_8
- Kroupa P., 2015, *Canadian Journal of Physics*, 93, 169
- Kroupa P., Weidner C., 2003, *ApJ*, 598, 1076
- Kroupa P., Weidner C., Pflamm-Altenburg J., Thies I., Dabringhausen J., Marks M., Maschberger T., 2013, *The Stellar and Sub-Stellar Initial Mass Function of Simple and Composite Populations*. p. 115, doi:10.1007/978-94-007-5612-0_4
- Kroupa P., Jeřábková T., Dinnbier F., Beccari G., Yan Z., 2018, *A&A*, 612, A74
- Kroupa P., Haslbauer M., Banik I., Nagesh S. T., Pflamm-Altenburg J., 2020, *arXiv e-prints*, p. [arXiv:2007.07905](https://arxiv.org/abs/2007.07905)
- Kupi G., Amaro-Seoane P., Spurzem R., 2006, *MNRAS*, 371, L45
- Lada C. J., 2010, *Philosophical Transactions of the Royal Society of London Series A*, 368, 713
- Lada C. J., Lada E. A., 2003, *ARA&A*, 41, 57
- Laine S., et al., 2020, *ApJ*, 894, L1
- Larsen S. S., 2002a, *AJ*, 124, 1393
- Larsen S. S., 2002b, in Geisler D. P., Grebel E. K., Minniti D., eds, *IAU Symposium Vol. 207, Extragalactic Star Clusters*. p. 421 ([arXiv:astro-ph/0105489](https://arxiv.org/abs/astro-ph/0105489))
- Larsen S. S., Richtler T., 2000, *A&A*, 354, 836
- Larson R. B., 1998, *MNRAS*, 301, 569
- Latif M. A., Ferrara A., 2016, *Publ. Astron. Soc. Australia*, 33, e051
- Latif M. A., Schleicher D. R. G., 2015, *A&A*, 578, A118
- Latif M. A., Lupi A., Schleicher D. R. G., D'Amico G., Panci P., Bovino S., 2019, *MNRAS*, 485, 3352
- Lee M. H., 1993, *ApJ*, 418, 147
- Lee H. M., 1995, *MNRAS*, 272, 605
- Lee J. C., et al., 2009, *ApJ*, 706, 599
- Leigh N., Sills A., Böker T., 2013, *MNRAS*, 433, 1958
- Lena D., Robinson A., Marconi A., Axon D. J., Capetti A., Merritt D., Batcheldor D., 2014, *ApJ*, 795, 146
- Leroy A. K., et al., 2018, *ApJ*, 869, 126
- Li H., Gnedin O. Y., Gnedin N. Y., Meng X., Semenov V. A., Kravtsov A. V., 2017, *ApJ*, 834, 69
- Li X., Chang P., Levin Y., Matzner C. D., Armitage P. J., 2020, *MNRAS*, 494, 2327
- Lim J., Wong E., Ohyama Y., Broadhurst T., Medezinski E., 2020, *Nature Astronomy*, 4, 153
- Lonsdale C. J., Diamond P. J., Thrall H., Smith H. E., Lonsdale C. J., 2006, *ApJ*, 647, 185
- Lorenzo M. F., et al., 2014, *The Astrophysical Journal*, 788, L39
- Lüghausen F., Famaey B., Kroupa P., Angus G., Combes F., Gentile G., Tiret O., Zhao H., 2013, *MNRAS*, 432, 2846
- Lynden-Bell D., Rees M. J., 1971, *MNRAS*, 152, 461
- Maíz Apellániz J., 2008, *ApJ*, 677, 1278
- Mancini C., et al., 2019, *MNRAS*, 489, 1265
- Manti S., Gallerani S., Ferrara A., Greig B., Feruglio C., 2017, *MNRAS*, 466, 1160
- Mapelli M., 2016, *MNRAS*, 459, 3432
- Marks M., Kroupa P., 2010, *MNRAS*, 406, 2000
- Marks M., Kroupa P., 2011, *MNRAS*, 417, 1702
- Marks M., Kroupa P., 2012, *A&A*, 543, A8
- Marks M., Kroupa P., Dabringhausen J., Pawłowski M. S., 2012, *MNRAS*, 422, 2246
- Martín-Navarro I., 2016, *MNRAS*, 456, L104
- Martín-Navarro I., Vazdekis A., Falcón-Barroso J., La Barbera F., Yıldırım A., van de Ven G., 2018, *MNRAS*, 475, 3700
- Martín-Navarro I., et al., 2019, *A&A*, 626, A124
- Martini P., Weinberg D. H., 2001, *ApJ*, 547, 12
- Massey P., 2003, *ARA&A*, 41, 15
- Massey P., Johnson K. E., Degioia-Eastwood K., 1995, *ApJ*, 454, 151
- Matteucci F., 1994, *A&A*, 288, 57
- Mayer L., Bonoli S., 2019, *Reports on Progress in Physics*, 82, 016901
- Mazzucchelli C., et al., 2017, *ApJ*, 849, 91
- McConnell N. J., Ma C.-P., 2013, *ApJ*, 764, 184
- McCraday N., Graham J. R., 2007, *The Astrophysical Journal*, 663, 844
- McDermid R. M., et al., 2015, *MNRAS*, 448, 3484
- Megeath S. T., et al., 2016, *AJ*, 151, 5
- Meidt S. E., et al., 2015, *ApJ*, 806, 72
- Melia F., 2009, *High-Energy Astrophysics*
- Merritt D., 2017, *Studies in the History and Philosophy of Modern Physics*, 57, 41
- Merritt D., 2020, *A Philosophical Approach to MOND: Assessing the Milgromian Research Program in Cosmology*
- Meurer G. R., et al., 2009, *ApJ*, 695, 765
- Mezcua M., 2017, *International Journal of Modern Physics D*, 26, 1730021
- Mieske S., et al., 2008, *A&A*, 487, 921
- Milgrom M., 1983, *ApJ*, 270, 365
- Miller M. C., Davies M. B., 2012, *ApJ*, 755, 81
- Miller M. C., Hamilton D. P., 2002, *MNRAS*, 330, 232
- Miller T. B., et al., 2018, *Nature*, 556, 469
- Murray N., 2009, *ApJ*, 691, 946
- Naab T., Ostriker J. P., 2017, *ARA&A*, 55, 59
- Naab T., Johansson P. H., Ostriker J. P., 2009, *ApJ*, 699, L178
- Naab T., et al., 2014, *MNRAS*, 444, 3357
- Neumayer N., Seth A., Boeker T., 2020, *arXiv e-prints*, p. [arXiv:2001.03626](https://arxiv.org/abs/2001.03626)
- Nguyen D. D., Seth A. C., Reines A. E., den Brok M., Sand D., McLeod B., 2014, *ApJ*, 794, 34
- Nguyen N. H., Lira P., Trakhtenbrot B., Netzer H., Ciccone C., Maiolino R., Shemmer O., 2020, *ApJ*, 895, 74

- Nipoti C., Londrillo P., Ciotti L., 2007, *ApJ*, 660, 256
- Nipoti C., Treu T., Auger M. W., Bolton A. S., 2009, *ApJ*, 706, L86
- Norman C. A., 1987, in Lonsdale Persson C. J., ed., *NASA Conference Publication Vol. 2466*, NASA Conference Publication.
- Oey M. S., Clarke C. J., 2005, *ApJ*, 620, L43
- Offner S. S. R., Clark P. C., Hennebelle P., Bastian N., Bate M. R., Hopkins P. F., Moraux E., Whitworth A. P., 2014, in Beuther H., Klessen R. S., Dullemond C. P., Henning T., eds, *Protostars and Planets VI*. p. 53 ([arXiv:1312.5326](https://arxiv.org/abs/1312.5326)), doi:10.2458/azu_uapress_9780816531240-ch003
- Oh S., Kroupa P., 2018, *MNRAS*, 481, 153
- Pacucci F., Loeb A., 2019, *ApJ*, 870, L12
- Panther B., Heavens A. F., Jimenez R., 2004, *MNRAS*, 355, 764
- Papadopoulos P. P., 2010, *ApJ*, 720, 226
- Pavesi R., et al., 2018, *ApJ*, 861, 43
- Pavlík V., Jeřábková T., Kroupa P., Baumgardt H., 2018, *A&A*, 617, A69
- Pavlík V., Kroupa P., Šubr L., 2019, *A&A*, 626, A79
- Peters P. C., 1964, *Physical Review*, 136, 1224
- Pflamm-Altenburg J., Kroupa P., 2009, *MNRAS*, 397, 488
- Pflamm-Altenburg J., Weidner C., Kroupa P., 2009, *MNRAS*, 395, 394
- Pflamm-Altenburg J., Weidner C., Kroupa P., 2011, in Treyer M., Wyder T., Neill J., Seibert M., Lee J., eds, *Astronomical Society of the Pacific Conference Series Vol. 440*, UP2010: Have Observations Revealed a Variable Upper End of the Initial Mass Function?. p. 269 ([arXiv:1011.2200](https://arxiv.org/abs/1011.2200))
- Pflamm-Altenburg J., González-Lópezlira R. A., Kroupa P., 2013, *MNRAS*, 435, 2604
- Planck Collaboration et al., 2018a, preprint, p. [arXiv:1807.06205](https://arxiv.org/abs/1807.06205) ([arXiv:1807.06205](https://arxiv.org/abs/1807.06205))
- Planck Collaboration et al., 2018b, *arXiv e-prints*, p. [arXiv:1807.06209](https://arxiv.org/abs/1807.06209)
- Ploeckinger S., Schaye J., Hacar A., Maseda M. V., Hodge J. A., Bouwens R. J., 2019, *MNRAS*, 484, 4379
- Portegies Zwart S. F., McMillan S. L. W., 2002, *ApJ*, 576, 899
- Portegies Zwart S. F., Baumgardt H., Hut P., Makino J., McMillan S. L. W., 2004, *Nature*, 428, 724
- Portinari L., Kotilainen J., Falomo R., Decarli R., 2012, *MNRAS*, 420, 732
- Radhakrishnan R., Hindmarsh A., 1993, *Description and Use of LSODE, the Livermore Solver for Ordinary Differential Equations*. Lawrence Livermore National Laboratory
- Ramasawmy J., Stevens J., Martin G., Geach J. E., 2019, *MNRAS*, 486, 4320
- Randriamanakoto Z., Escala A., Väisänen P., Kankare E., Kotilainen J., Mattila S., Ryder S., 2013, *ApJ*, 775, L38
- Randriamanakoto Z., Väisänen P., Ryder S. D., Ranaivomanana P., 2019, *MNRAS*, 482, 2530
- Rasio F. A., Freitag M., Gürkan M. A., 2004, *Coevolution of Black Holes and Galaxies*, p. 138
- Recchi S., Kroupa P., 2015, *MNRAS*, 446, 4168
- Recchi S., Calura F., Kroupa P., 2009, *A&A*, 499, 711
- Reid M. J., Brunthaler A., 2020, *arXiv e-prints*, p. [arXiv:2001.04386](https://arxiv.org/abs/2001.04386)
- Riaz R., Schleicher D. R. G., Vanaverbeke S., Klessen R. S., 2020, *arXiv e-prints*, p. [arXiv:2003.07639](https://arxiv.org/abs/2003.07639)
- Riechers D. A., et al., 2020, *arXiv e-prints*, p. [arXiv:2004.10204](https://arxiv.org/abs/2004.10204)
- Rodríguez C. L., Morscher M., Wang L., Chatterjee S., Rasio F. A., Spurzem R., 2016, *MNRAS*, 463, 2109
- Romano D., Matteucci F., Zhang Z.-Y., Papadopoulos P. P., Iverson R. J., 2017, *MNRAS*, 470, 401
- Rowlands K., Gomez H. L., Dunne L., Aragón-Salamanca A., Dye S., Maddox S., da Cunha E., van der Werf P., 2014, *MNRAS*, 441, 1040
- Salpeter E. E., 1955, *ApJ*, 121, 161
- Salpeter E. E., 1964, *ApJ*, 140, 796
- Salvador-Rusiñol N., Vazdekis A., La Barbera F., Beasley M. A., Ferreras I., Negri A., Dalla Vecchia C., 2020, *Nature Astronomy*, 4, 252
- Sanghvi J., Kotilainen J. K., Falomo R., Decarli R., Karhunen K., Uslenghi M., 2014, *MNRAS*, 445, 1261
- Schneider F. R. N., et al., 2018, *Science*, 359, 69
- Schramm M., et al., 2019, *ApJ*, 881, 145
- Schulz C., Pflamm-Altenburg J., Kroupa P., 2015, *A&A*, 582, A93
- Schulz C., Hilker M., Kroupa P., Pflamm-Altenburg J., 2016, *A&A*, 594, A119
- Scoville N., et al., 2017, *ApJ*, 837, 150
- Seidel M. K., et al., 2015, *MNRAS*, 446, 2837
- Seth A. C., et al., 2014, *Nature*, 513, 398
- Shankar F., et al., 2014, *MNRAS*, 439, 3189
- Shields G. A., 1999, *PASP*, 111, 661
- Shin S., et al., 2020, preprint, p. [ArXiv:2003.00709](https://arxiv.org/abs/2003.00709) ([ArXiv:2003.00709](https://arxiv.org/abs/2003.00709))
- Silich S., Bisnovaty-Kogan G., Tenorio-Tagle G., Martínez-González S., 2011, *ApJ*, 743, 120
- Song H., Park C., Lietzen H., Einasto M., 2016, *ApJ*, 827, 104
- Speagle J. S., Steinhardt C. L., Capak P. L., Silverman J. D., 2014, *ApJS*, 214, 15
- Spurzem R., 1999, *Journal of Computational and Applied Mathematics*, 109, 407
- Steinhardt C. L., Capak P., Masters D., Speagle J. S., 2016, *ApJ*, 824, 21
- Stolte A., et al., 2014, *ApJ*, 789, 115
- Strader J., Chomiuk L., Maccarone T. J., Miller-Jones J. C. A., Seth A. C., 2012, *Nature*, 490, 71
- Suh H., Civano F., Trakhtenbrot B., Shankar F., Hasinger G., Sanders D. B., Allevato V., 2020, *ApJ*, 889, 32
- Tamburri S., Saracco P., Longhetti M., Gargiulo A., Lonoce I., Ciocca F., 2014, *A&A*, 570, A102
- Tamburro D., Rix H.-W., Walter F., Brinks E., de Blok W. J. G., Kennicutt R. C., Mac Low M.-M., 2008, *AJ*, 136, 2872
- Tanaka M., et al., 2019, *ApJ*, 885, L34
- Tenorio-Tagle G., Silich S., Muñoz-Tuñón C., 2007, *New Astron. Rev.*, 51, 125
- Tenorio-Tagle G., Wunsch R., Silich S., Muñoz-Tuñón C., Palouš J., 2010, *ApJ*, 708, 1621
- Terlevich R., Melnick J., 1985, *MNRAS*, 213, 841
- Thomas D., Greggio L., Bender R., 1999, *MNRAS*, 302, 537
- Thomas D., Maraston C., Bender R., Mendes de Oliveira C., 2005, *ApJ*, 621, 673
- Thorne K. S., Zytkov A. N., 1975, *ApJ*, 199, L19
- Thorne K. S., Zytkov A. N., 1977, *ApJ*, 212, 832
- Trakhtenbrot B., 2020, *arXiv e-prints*, p. [arXiv:2002.00972](https://arxiv.org/abs/2002.00972)
- Trakhtenbrot B., Lira P., Netzer H., Ciccone C., Maiolino R., Shemmer O., 2018, *arXiv e-prints*, p. [arXiv:1801.01508](https://arxiv.org/abs/1801.01508)
- Tsuboi M., Kitamura Y., Tsutsumi T., Uehara K., Miyoshi M., Miyawaki R., Miyazaki A., 2017, *ApJ*, 850, L5
- Vazdekis A., Peletier R. F., Beckman J. E., Casuso E., 1997, *ApJS*, 111, 203
- Vazdekis A., Koleva M., Ricciardelli E., Röck B., Falcón-Barroso J., 2016, *MNRAS*, 463, 3409
- Virtanen P., et al., 2019, *arXiv e-prints*, p. [arXiv:1907.10121](https://arxiv.org/abs/1907.10121)
- Voggel K. T., et al., 2018, *ApJ*, 858, 20
- Voggel K. T., Seth A. C., Baumgardt H., Mieske S., Pfeffer J., Rasskazov A., 2019, *ApJ*, 871, 159
- Wang L., 2020, *MNRAS*, 491, 2413
- Wang L., et al., 2016, *MNRAS*, 458, 1450
- Wang L., Kroupa P., Takahashi K., Jerabkova T., 2020, *MNRAS*, 491, 440
- Wehner E. H., Harris W. E., 2006, *ApJ*, 644, L17
- Weidner C., Kroupa P., 2004, *MNRAS*, 348, 187
- Weidner C., Kroupa P., Larsen S. S., 2004, *MNRAS*, 350, 1503
- Weidner C., Ferreras I., Vazdekis A., La Barbera F., 2013a, *MNRAS*, 435, 2274

- Weidner C., Kroupa P., Pflamm-Altenburg J., Vazdekis A., 2013b, MNRAS, 436, 3309
- Whitmore B. C., Chandar R., Bowers A. S., Larsen S., Lindsay K., Ansari A., Evans J., 2014, AJ, 147, 78
- Willott C. J., et al., 2010, AJ, 140, 546
- Wirth H., Bekki K., 2020, arXiv e-prints, p. arXiv:2006.02517
- Wittenburg N., Kroupa P., Famaey B., 2020, ApJ, 890, 173
- Wolfe A. M., Burbidge G. R., 1970, ApJ, 161, 419
- Woods T. E., Heger A., Haemmerlé L., 2020, MNRAS, 494, 2236
- Wright G. S., Joseph R. D., Robertson N. A., James P. A., Meikle W. P. S., 1988, MNRAS, 233, 1
- Wu X.-B., Wang R., Schmidt K. B., Bian F., Jiang L., Fan X., 2011, AJ, 142, 78
- Yamaguchi R., et al., 2001, PASJ, 53, 985
- Yan Z., Jerabkova T., Kroupa P., 2017, A&A, 607, A126
- Yan Z., Jerabkova T., Kroupa P., 2019a, arXiv e-prints, p. arXiv:1911.02568
- Yan Z., Jerabkova T., Kroupa P., Vazdekis A., 2019b, A&A, 629, A93
- Yan Z., Jerabkova T., Kroupa P., 2020, A&A, 637, A68
- Yang J., et al., 2018, AJ, 155, 110
- Yang J., et al., 2020, arXiv e-prints, p. arXiv:2006.13452
- Yoo J., Miralda-Escudé J., 2004, ApJ, 614, L25
- Yoshida N., Bromm V., Hernquist L., 2004, ApJ, 605, 579
- Yu Q., Tremaine S., 2002, MNRAS, 335, 965
- Zhang Q., Fall S. M., 1999, ApJ, 527, L81
- Zhang Z.-Y., Romano D., Ivison R. J., Papadopoulos P. P., Matteucci F., 2018, Nature, 558, 260
- Zibetti S., Gallazzi A. R., Hirschmann M., Consolandi G., Falcón-Barroso J., van de Ven G., Lyubenova M., 2019, arXiv e-prints, p. arXiv:1906.02209
- de La Rosa I. G., La Barbera F., Ferreras I., de Carvalho R. R., 2011, MNRAS, 418, L74
- de la Rosa I. G., La Barbera F., Ferreras I., Sánchez Almeida J., Dalla Vecchia C., Martínez-Valpuesta I., Stringer M., 2016, MNRAS, 457, 1916

Appendix 1: Special case of Sec. 8.1

The special case, $\dot{m}_{\text{BH}} = 0$, $\dot{M}_g \propto M_g^2$, leads to an analytical solution to the mass increase of the gas mass within R : Assuming the gas mass within R to grow through Bondi-Hoyle accretion from the surrounding forming spheroid. This is essentially accelerating gas infall from the forming host galaxy and is given by Eq. 40 with velocity $v = 0$ since the central cluster is approximately at rest relative to the forming spheroid, and ρ_g being the average gas density of the protogalaxy, i.e. $\rho_g = M_{\text{gal}}/V_{\text{gal}}$. Here, M_{gal} is the initial mass of the post-Big-Bang gas cloud which will form the spheroid with a stellar mass of $M_{\text{Igal}} = M_{\text{gal}}/3$ for a star-formation efficiency of 1/3, and V_{gal} is the volume of this gas cloud. This volume can be taken to be a sphere of radius of $R_{\text{gal}} \approx 10$ kpc.

The analytical solution for the gas mass, M_g , as a function of time is derived. We have,

$$\dot{M}_g = \frac{dM_g}{dt} = 4\pi\rho_g \frac{G^2(M_g + Nm_{\text{BH}})^2}{c_s^3}, \quad (51)$$

where

$$\rho_g = \frac{M_{\text{gal}}}{4/3\pi R_{\text{gal}}^3}, \quad (52)$$

is given, as well as c_s . Eq. 51 can be rewritten as

$$\frac{dM_g}{dt} = K(M_g + Nm_{\text{BH}})^2 \quad (53)$$

where $K = 4\pi\rho_g G^2/c_s^3$ combines all the given constants. We can then separate the variables and integrate, obtaining

$$\int_{M_g^0}^{M_g} \frac{dM_g}{(M_g + Nm_{\text{BH}})^2} = \int_0^t K \cdot t, \quad (54)$$

which results in

$$\frac{1}{Nm_{\text{BH}} + M_g^0} - \frac{1}{Nm_{\text{BH}} + M_g} = K \cdot t. \quad (55)$$

Thus M_g can be expressed as a function of time as,

$$M_g(t) = \frac{1}{\frac{1}{Nm_{\text{BH}} + M_g^0} - K \cdot t} - Nm_{\text{BH}}. \quad (56)$$

Appendix 2: SMBH–spheroid-mass relations

Additional Fig. 18 to show the effect of using a bottom-heavy mass function of embedded clusters with Salpeter power-law index $\beta = 2.4$.

This paper has been typeset from a $\text{\TeX}/\text{\LaTeX}$ file prepared by the authors.

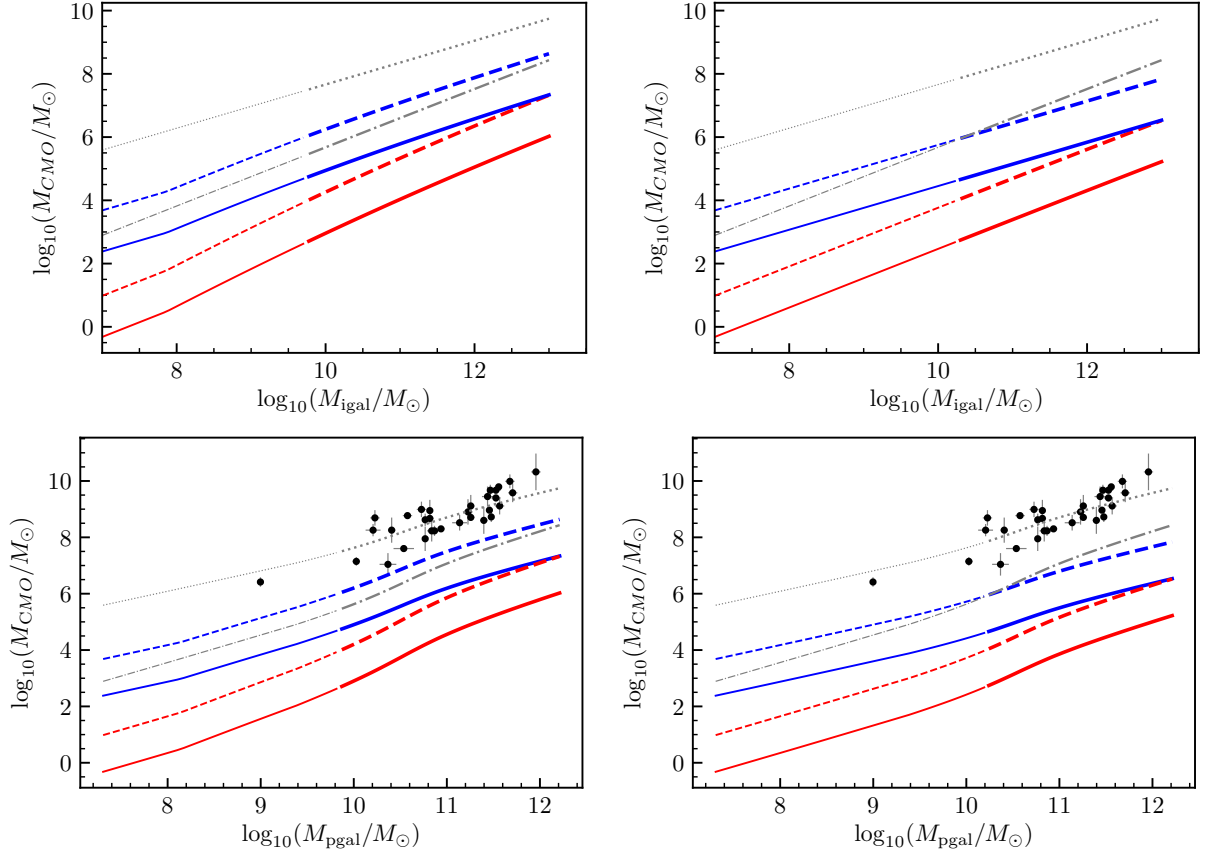


Figure 18. As Fig. 11 but for $\beta = 2.4$. Note the smaller SMBH-seed masses at a given value of present-day spheroid mass, M_{pgal} .